TIME-RESOLVED MICROFLUIDIC FLOW CYTOMETRY

By

Yan Wang

Supervisors:

Prof. James A. Piper

Dr. Yiqing Lu

FACULTY OF SCIENCE AND ENGINEERING

Department of Physics and Astronomy

This thesis is presented for the degree of Doctor of Philosophy

February 2019

I certify that the work in this thesis has not previously been submitted for a degree nor has it been submitted as part of requirements for a degree to any other university or institution other than Macquarie University.

I also certify that the thesis is an original piece of research and it was authored by myself. Help and assistance that I have received in the course of my research work and in the preparation of the thesis itself has, where appropriate, been acknowledged.

In addition, I certify that all information sources and literature used in the course of this research is also indicated where appropriate in this record of my thesis.

Yan Wang   01-Feb-2019

Acknowledgements

I sincerely thank my PhD supervisors, Prof. Jim A. Piper and Dr Yiqing Lu, both passing me not only their plenty knowledge and experience of the research, but also enthusiasm in the academia. I am greatly inspired by Prof. Piper's curiosity in science and insight on the project, he is always patient and encouraging with the students and young researchers. In particular, I am truly impressed by his orientation to pursue practical applications by commercializing scientific output to make an impact on people's lives. I am extremely grateful to gain the supervision from Dr. Yiqing Lu who guides me with his knowledge and intelligence in extensive disciplines. He is very professional in academic works and inspires me with his humble attitude about research and life, shaping me to be an independent and critical thinking researcher. I was ensured on the right track throughout the course of PhD due to their continued patience and unwavering approach to the research exploration.

I acknowledge our group members and lab colleagues who contribute significantly to my PhD project. I show my great appreciations to Dr. Nima Sayyadi from Department of Molecular Sciences. He patiently inducts me all the biological and chemical experiments involved in my project, from whom, I learnt cell culture and staining with Eu chelates. I would like to also thank Dr. Xianlin Zheng who provides valuable suggestions over my project and has been quite helpful on the lab inductions and demonstrations during my PhD study, I am significantly impressed by his ambitious pursuit in life.

I had thoroughly enjoyable experience with my colleagues at the MQ node of the Centre for Nanoscale Biophotonics (CNBP). I would like to show my acknowledgements to them, particularly, Dr Bingyang Shi, Dr. Lianmei Jiang, Dr. Wei Deng, Dr. Annemarie Nadort, Dr. Liuen Liang, Dr. Libing Fu, Dr. Nicole Cordina, Dr. Deming Liu, Dr. Denitza Denkova, Dr. Martin Ploschner, Dr. Liisa Kautto, Dr. Tom Lawson and Dr. Ayad Anwer. Their brilliance and skills have added a great value to my research results. I sincerely appreciate the generous help from these nice people and will cherish the interactions with all of them.

I also greatly appreciate the help offered by Mr. Walther Adendorff, Mr. Greg Yates, Mr. Benny Wang, and Mr. Ken Yuen in Macquarie Engineering & Technical Service (METS), they kindly assisted me with the mechanical design and electronic work for the

Abstract

Flow cytometry is extensively applied in life sciences and clinical practice for high-throughput identification and characterization of cells, particles or microorganisms suspended in fluid samples. However, conventional flow cytometry based on spectral detection suffers from two main disadvantages: interference from biological autofluorescence, and spectral crosstalk of fluorochromes. Time-resolved detection employing long-lived luminescent probes such as lanthanide complexes provides an effective strategy to overcome these issues. It effectively removes short-lived autofluorescence background arising from non-target specimens in the sample, resulting in high detection sensitivity and contrast. Multiplexing can be realised based on the luminescence lifetimes of the probes, avoiding spectral crosstalk between the detection channels.

This thesis reports the design, development and demonstration of a time-resolved microfluidic flow cytometer (TRMFC) as a practical and low-cost technique aiming to achieve lifetime-based multiplexed biosensing. A microfluidic chip coupled with a piezoelectric transducer is used for two-dimensional acoustic focusing of the events at the centre of the flow channel. The sample flow rates are set so that sufficient signal from the long-decay luminescence can be acquired as targets transit the detection aperture, to ensure accurate lifetime measurement. The excitation source (i.e. UV LED) and detector (i.e. gatable PMT) are pulsed with a time-shift delay between them to discriminate the autofluorescent before luminescence signal detection.

The current TRMFC system is able to achieve high counting efficiencies (>90%) of the luminescent targets passing through the microfluidic channel, and resolve lifetimes of individual targets at high accuracy (coefficient of variation ~2.4%). The acoustic focusing efficiency under varied flow velocity and the influence on time-resolved detection have been analysed in detail. The results indicate that a flow rate as high as 20 µl/min can be applied in the current system without affecting accurate counting of the events and measurement of their individual lifetime and intensity.

Poisson statistics has been applied to calculate the overlap probability of two or more events presenting simultaneously in the detection aperture. A peak detection algorithm has been developed to resolve the overlap events containing two targets; whereas events with three and more targets overlapped with each other are discarded due to significantly increased computational complexity and reduced robustness for nonlinear fitting. The probability of three and more targets overlap is limited to <1% by proper configuration of key experimental parameters including the detection aperture size, the flow velocity and the sample concentration, so that optimum performance is achieved at highest sample throughput.

Finally, a pilot multiplexing bioassay has been demonstrated using two cell lines stained with different europium complexes. Factors that influence the luminescence lifetimes and intensities of the stained cells, including different cell lines, cell growth phases, fixation of cells, chelate structures, ratio of chelators and Eu^{3+}, and reaction solvents for the chelates, have been investigated experimentally. Samples containing the two distinct cell types have been successfully analysed using the TRMFC. This new technique, upon further optimisation, is expected to benefit on-site screening of fluidic samples containing multiple target populations, such as blood, urine and environmental water, opening a range of opportunities using lanthanide complex as biosensors for ultrasensitive biomedical diagnostics.

Key Words: time-resolved luminescence; flow cytometry; acoustic focusing; microfluidics; lanthanide chelates; lifetime multiplexing

Content

List of Acronyms

(In Alphabetic Order)

AC   Alternating Current

ACN   Acetonitrile

AI   Artificial Intelligence

BHHBCB   1, 2-bis [4'-(1", 1", 1", 2", 2", 3", 3"-heptafluoro-4", 6"- hexanedion-6 "-yl)-benzyl]-4-chlorosulfobenzene

BHHCT   4,4'-bis(1",1",1",2",2",3",3"-heptafluoro-4",6"-hexanedion-6"-yl)-chlorosulfo-o-terphenyl

BHHTEGST   1 (4, 4'-bis(1", 1", 1", 2", 2", 3", 3"-heptafluoro-4", 6"- hexanedion-6"-yl) sulfonylamino-tetraethyleneglycol-succinimidyl carbonate-o-terphenyl)

CCD   Charge Coupled Device

CV   Coefficient of Variation

CW   Continuous Wave

DAQ   Data Acquisition

DMF   Dimethylformamide

DMSO   Dimethyl Sulfoxide

DNA   Deoxyribonucleic Acid

DRIE   Deep Reactive Ion Etching

Er   Erbium

Eu   Europium

FLIM	Fluorescence Lifetime Imaging Microscopes
FOV	Field of View
FWHM	Full Width at Half Maximum
HIV	Human Immunodeficiency Virus
IACS	Image-Activated Cell Sorting
ISC	Intersystem Crossing
La	Lanthanum
LED	Light Emitting Diodes
Ln	Lanthanide
MEMS	Microelectromechanical Systems
NA	Numerical Aperture
OSAM	Orthogonal Scanning Automated Microscopy
PBS	Phosphate Buffered Saline
PDMS	Polydimethylsiloxane
PFA	Paraformaldehyde
PMT	Photomultiplier Tube
PVA	Polyvinyl Alcohol
PZT	Lead Zirconate Titanate
RNA	Ribonucleic Acid
SERS	Surface Enhanced Raman Scattering
SNR	Signal-to-Noise Ratio

Tb   Terbium

TCSPC   Time-Correlated Single Photon Counting

TGL   Time-Gated Luminescence

Tm   Thulium

TTL   Transistor-Transistor Logic

UCNP   Upconversion Nanoparticle

UV   Ultraviolet

Chapter 1:   Introduction

This thesis reports design, construction and operation of a time-resolved microfluidic flow cytometer (TRMFC), incorporating a sheath-free acoustic-focusing microfluidic chip and accurate lifetime-resolving detection applied to long-lived (100 µs-2000 µs) luminescent lanthanide-based bioprobes. The project is aimed at development of a practical, low-cost technology enabling real-time, background-free, multiplexed detection of target analytes in liquid biomedical samples. The problem of distinguishing background autoflourescence from optically-excited biosamples is circumvented by increasing the signal to background ratio using a scheme of pulsed excitation and time-delayed detection of the long-lifetime luminescent probes. TRMFC has large potential in temporal-multiplexing with the use of lanthanide probes which have tens of distinct lifetime codes simultaneously in the same wavelength bands.[1,2] Moreover, TRMFC can be very affordable compared to the conventional flow cytometry based on spectral multiplexing (i.e. colour coding of the probes), because lifetime-based multiplexing requires only a single excitation source and a single optical detection system including a single detector. High accuracy in resolving lifetime codes and high target counting efficiency is achieved with the application of acoustic focusing in the microfluidic flow channel, with sample flow velocity optimised to permit adequate data sampling for individual detection events where luminescence lifetimes are long and emission intensity low. The results of the present studies indicate that TRMFC has significant potential for the screening of fluidic biosamples containing multiple subpopulations of targets at low concentration (i.e. rare-event targets), for example, detection of cancer cells or fragments in human blood or urine, or rare-event pathogens in environmental samples.

This chapter describes the motivation, aims, concepts and technical challenges underlying the present development of TRMFC in the context of relevant previous research reported in the international technical literature. The following chapters will describe the design of the TRMFC instrumentation, methodology involved, evaluation and calibration of the system, and demonstration of a specific lifetime-multiplexed bioassay using the system. The suggested applications of TRMFC in practice and future work will be discussed at the end of the thesis.

1.1 Background and Motivations

Flow cytometry is a broadly-applied methodology in bioscience research and clinical practice for high-throughput identification and characterization of particles, cells or microorganisms suspended in fluid samples[3–5]. In conventional colour-based flow cytometry, the targeted cells or particles are labelled with colour-coded probes which upon ultraviolet or visible excitation generate fluorescence emission at distinct wavelengths, detected in separate optical channels. Acquiring quantitative information about multiple parameters for individual target cells (e.g., the intensity of particular reporters and the volume size of the cells) allows the status of target cells to be characterised in detail (e.g., changes in the distributions of cellular components and variations in the expression of particular genes). Compared to the methods of detection by conventional microscopy, flow cytometry allows rapid rates of event analysis (~10,000 events/second) with high precision and sensitivity, of great value for large population analysis and also rare events detection. In addition, flow cytometry is regarded as a non-destructive technology, which permits subsequent cell recovery or purification when coupled with the sorting capabilities of modern instruments.[6–9] The above abilities of flow cytometry in analysing and sorting single cells results in a wide range of applications in biomedical research and clinical diagnostics.

The past few decades have seen a number of technical advances in flow cytometry typically focusing on increasing the numbers of parameters that can be measured simultaneously and rapidly from individual events. Seventeen-colour flow cytometry capable of measuring 19 parameters simultaneously was reported in 2004 and now it is routinely used[10], 30-parameter polychromatic flow cytometry has been commercialized and recently researchers have reported 50-parameter platforms[9,11]. The increase of parameters that can be detected on the polychromatic flow cytometry is based on the extension of the classical design with more powerful lasers and additional detectors, which however, require careful control to prevent spectral overlap between channels, and inevitably also result in increased instrumental cost. The number of detectable parameters per cell is also restricted by the strong and spectrally-broad autofluorescence background which overlaps the fluorescent signals from the colour-coded probes. The detection sensitivity is also limited because of low signal to noise ratio (SNR), especially in application to rare event detection. [4,12] As a result, an excitation and detection methodology which avoids the problems arising

from autofluorescence and spectral channel cross talk to deliver high-order multiplexing and background-free detection is demanded.

A new method of detection, time-resolved flow cytometry was reported by Condrau *et al.,* [12,13] , which is capable of eliminating the cellular autofluorescence based on the use of long-lived rare earth metal chelates (e.g., europium and terbium chelates, luminescence[14] lifetimes 30 μs-2ms) as reporters. The short autofluorescence lifetime, in the range of 1-100 ns [15], enables the background signal to be substantially removed using a delayed detection window following the excitation pulses. Following the suggestion of Leif *et al.* in the 1970's that the lifetimes of the probes can be used as the codes of label[16], Lu *et al.* [1,2] and Zhao *et al.* [17] succeeded in engineering tens of tunable luminescence lifetimes in the microsecond to millisecond range for both microspheres and nanocrystals, showing great potential for high-throughput analysis and temporal-domain multiplexing on time-resolved detection platforms. One advantage of using temporally-coded detection channels is the potential for low-cost and portable instruments as multiplexed lifetime channels in the same emission band share the same excitation source and the same capture optics and detector, with purpose-programmed software on PC undertaking lifetime decoding.

However, in previous research on time-resolved/time-gated flow cytometry, the ability to distinguish long-lifetime targets (hundreds of microseconds) was compromised by the high flow velocities (>1 m/s) of the sample stream necessary for focusing using conventional fluidic sheath methods, resulting in insufficient photon counting times to reliably determine the luminescence lifetime, limiting the resolving sensitivity and resulting in undetected events. Because of these high sample flow velocities, the detection region must be large for existing platforms (1.7 mm in Condrau *et al.* [12,13]; ~0.55-0.85 mm in Jin *et al.* [18,19]) to enable sufficient photon counting times, and therefore accurate determination of such long luminescence lifetimes. It was also necessary to decouple the excitation and detection regions to provide a time delay to eliminate autofluorescence and also to minimise the detection time. Additionally, luminescence signals from only one time-gated luminescence (TGL) cycle were retrieved for lifetime calculations on both systems, causing large random variation in the results. In addition, a significant number of events were missed during the long detection duration when the excitation source was off as reported by Condrau *et al.*

Improvement of the detection sensitivity could be achieved but at the expense of cell throughput: for 200 events per second detected and some 20% of the targets were missed

during 1 ms dark time intervals. Though 100% of the arriving events can be detected by setting high rates of TGL cycle on the platform integrated with a UV LED as described by Jin *et al*., the resolving accuracy of lifetimes is limited by the short detection interval (~60-150 µs) which is necessary to achieve a high target counting rate.

This thesis reports time-resolved microfluidic flow cytometry for accurate detection of long lifetime luminescence of lanthanide chelates by slowing down the flow velocity with a microfluidic chip capable of acoustic stream focusing, and lifetime-base multiplexing bioassay is developed for detection on this system. This platform can count >90% of luminescent targets that pass through the microfluidic channel and resolve lifetimes with high accuracy by decreasing flow velocity to acquire abundant TGL cycles during the time of event flying in the field of detection. However, the throughput of detection is limited by the possibility of overlap of double or more events showing in the detection aperture simultaneously, which is influenced by size of detection aperture and sample concentration. All these parameters, i.e., flow velocity with adequate acoustic focusing, TGL duration and duty, excitation and detection aperture size, sample concentration, are highly interactive, this is necessary to control operating conditions carefully to achieve optimized performance (high throughput and low overlap possibility) on TRMFC. The separation of two events with different lifetimes in the same TGL cycle is demonstrated in this thesis. Decoding more than two overlapped events is however unreliable and it is necessary to choose operating conditions so that the probability for more than two overlapping events is small, ideally <1%. Performance of the TRMFC system has been evaluated using calibrated europium (Eu) doped polymer microspheres to examine accuracy of lifetime, intensity and counting efficiency measurements, all these cross-validated against time-gated microscopy. Finally, analysis of biomedical samples comprising two target cell lines stained with different long-lifetime probes has been undertaken using TRMFC as a pilot demonstration of lifetime-based multiplexing detection of multiple analytes in a single sample.

1.2 Flow Cytometry

Flow cytometry is a sophisticated technique measuring multiple physical characteristics of a single cell such as size and granularity simultaneously as the cell flows in suspension through a measuring device[8,20]. Measurable cell parameters include: geometric properties, such as cell size (diameter, surface area, and volume). Using fluorescent probes in

combination with Flow Cytometry enables the physiological properties, such as membrane potential, integrity, and vitality; and quantities of DNA, RNA, cytokines, surface antigens, nuclear antigens, enzymes, proteins to be measured. Fluorescence Activated Cell Sorting (FACS)is an extension of this technology in which any single cell or object measured can be selectively removed from the suspension based on the measurements made. Due to the rich information that flow cytometry generates, it is frequently applied in disease diagnosis, chromosome karyotyping, cell function analysis, cancer therapy monitoring, detecting fetal cells, measuring cell kinetics, identifying tumour cells, cytogenetics, and fundamental cell biology[3][20].

1.2.1 Principle of Conventional Flow Cytometry

According to Shapiro, *cytometry* refers to the measurement of physical and/or chemical characteristics of cells or, by extension, of other biological properties. Flow cytometry is a process in which such measurements are made while the cells or particles pass, preferably in single file, through the measuring apparatus in a fluid stream[8].

For fluorescence-based flow cytometry, typically, cells or cellular structures are either labelled specifically with fluorescently-tagged antibody conjugates, or modified so that the cells are expressing fluorescent proteins. These cells are then hydro-dynamically focused by high speed sheath and are guided via laminar flow through a confined analysis space at high throughput rates. For each cell in the suspension, an increasingly large number of parameters is recorded and used to classify cells and cell populations.

There is only a limited number of components contributing to the core of a flow cytometric analysis instrument: a hydraulic system to route cells through a small observation volume, a light source to excite fluorescence, a detection system to detect the emitted fluorescence signals, and the signal processing involved to extract the resulting data. With FACS one or more parameters are used to select and separate individual cells with desired characteristics.
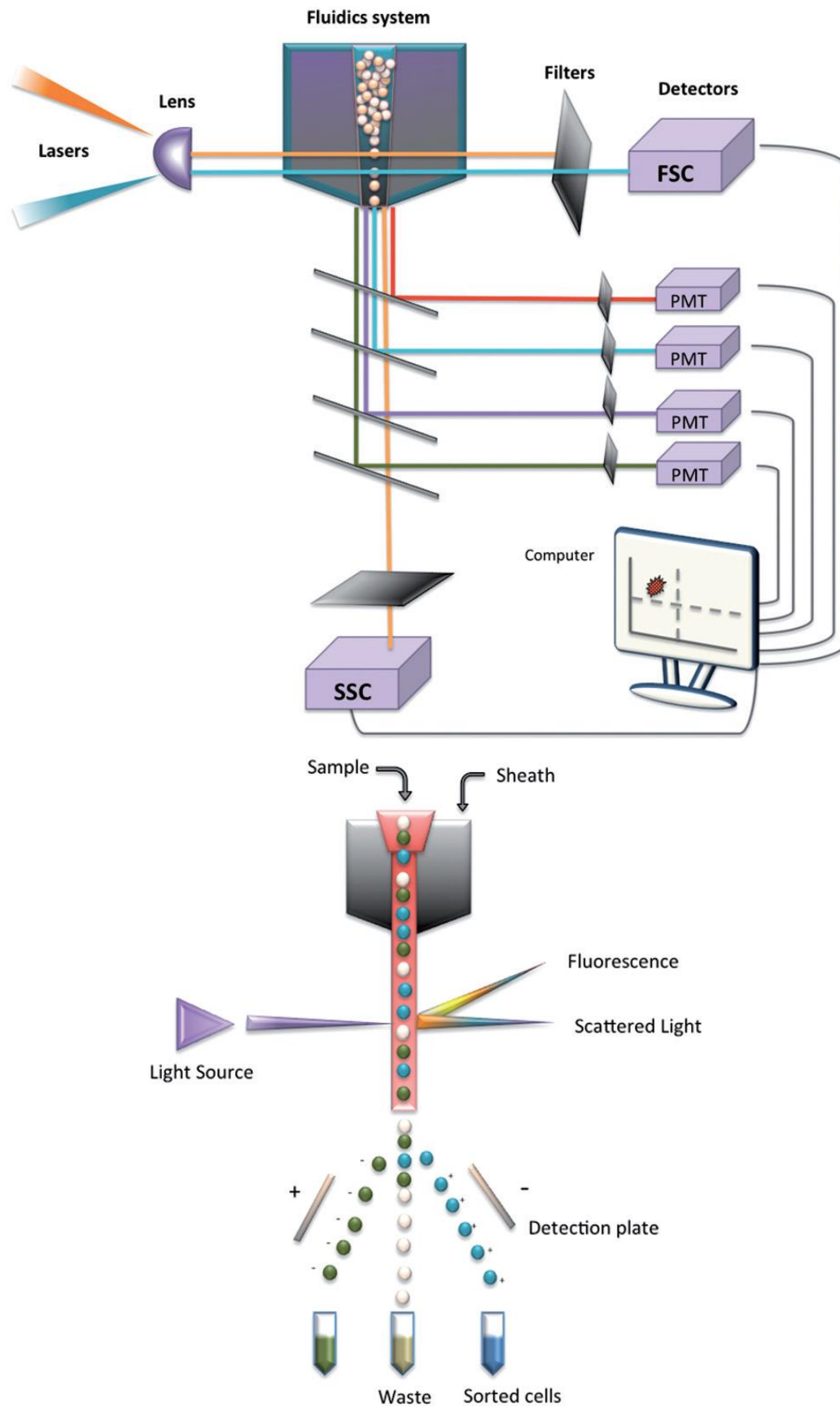
Figure 1-1 Schematic diagrams of a classic flow cytometer and cell sorting. Reprinted from Ref. [21].

As shown in Fig. 1-1, cells are injected into the core of a sheath flow and confined to a narrow single-file stream by hydrodynamic focusing. As fluorescent labelled cells flow past a focused laser beam, they generate light scattering and fluorescence emission measured by optics and electronics. Following optical detection of cells stained with fluorescent dye, the cells may be sorted based on their optical characteristics: commonly mechanical vibration of a nozzle tip at the end of a capillary tube generates droplets encapsulating cells, these droplets are selectively charged depending on the presence of labelled cells, and deflected by an electric field to different collectors.

The detailed design of practical flow cytometers must take into consideration a large number of practical issues including sample preparation (including fluorescence labelling techniques, methods of illuminating the targets, the use of fluidics to make sure that the targets flow individually past the illuminating beam, the use of detectors to measure signals from the cells, the use of computers to correlate the signals after they are stored in data files and the sorting methods to separate different populations of targets. These issues are discussed extensively in the literature [3,4,6–8,20–24]. A brief history of the development of flow cytometry is given in Appendix A.

1.2.2 Applications of Flow Cytometry

Flow cytometry is used to identify and count microorganisms in clinical, research, environmental, and industrial applications[24–26]. Clinical applications of classic flow cytometry range from differential blood count determination to the identification of fluorescence-labelled sub-populations of disease-specific cell types in cell suspensions[5]. Fig. 1-2 shows the most popular applications of flow cytometry in clinical medicine.
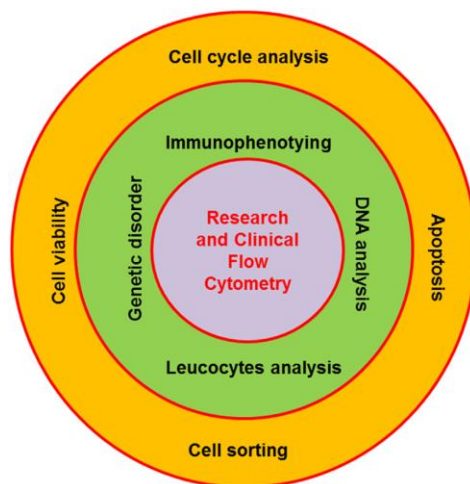
Figure 1-2 Current applications of flow cytometry in clinical medicine. Reprinted from Ref. [27].

Flow cytometry is not only applicable for making a diagnosis but also for disease monitoring and routine check-ups. It is often used in oncology-related analyses, such as for leukemia and lymphoma patients. The multicolour approach providing multiparametric analyses has led flow cytometry to be regarded as a cornerstone in cell biology research. For example, a mixture of four antibodies (CD45, CD3, CD4 and CD8) each tagged by a different fluorochrome allows identification and counting of all white blood cells, all lymphocytes, all T-lymphocytes and the two main subsets of T-lymphocytes. The concentration of CD4 cells in blood is used to diagnose AIDS and to monitor the response to therapy in AIDS patients. Intracellular staining for specific proteins such as cytokines requires cell fixation and permeabilization[28,29]. Flow cytometry is also an important tool for investigation and isolation of stem cells[30] to quantitate such cells on the basis of their expression of specific reliable markers.

Many advantages have been provided by the development of microfabricated flow cytometers that use microfluidics. Huh *et al.*[31] and Shrirao *et al.*[32] provide an excellent review of the technology. Microfluidics enable small fluid samples (10^{-9}–10^{-18} litres) to be processed and manipulated in channels with very small dimensions[33]. Microfluidic flow cytometers can be used to analyse single cells in a small population, cellular differences in gene expression or response to a drug within a population of cells[34,35]. These chip-based flow cytometers are cost- and size-effective and portable when compared to conventional benchtop instruments. And microfluidic flow cytometers have the ability to concentrate cells and particles at the centre of a microfluidic channel for direct analysis, which is based on

acoustic concentration. Graves and his colleagues illustrate the development of a low cost, high throughput ($>10^6$ cells/s) flow cytometer utilizing acoustic sample focusing done within rectangular channels[36–41], and validate its performance using standard microsphere mixtures. This will be reviewed in detail in the following sections. Another advantage of microfluidic flow cytometers is high-throughput screening in which small volumes of hundreds of thousands of samples can be analysed simultaneously. This approach has been used to analyse the cells for high protein content screening in 384 microfluidic flow channels, which uses laser scanning to analyse samples in parallel[42].
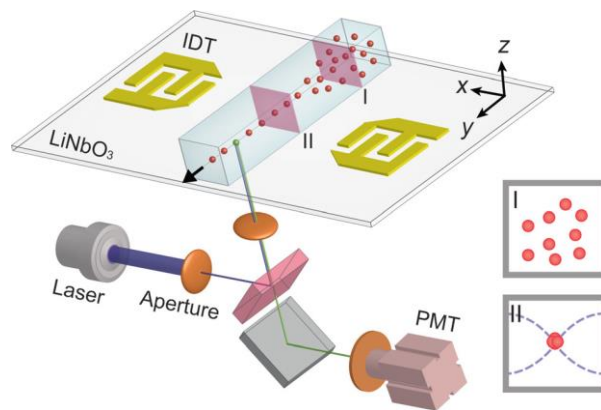
Figure 1-3 Standing surface acoustic waves particle focusing. A pair of interdigitated transducers (IDTs) positioned on either side of the microchannel generate acoustic waves which manipulate dispersed particles (I) into a single file line (II). These focused particles are then analysed using a standard fluorescence-based flow cytometry set up. Reprinted from Ref. [43].

Conventional flow cytometry is currently the method of choice for rapid quantification of cells, but it requires invasive extraction of cells from a living organism and associated procedures (e.g., fluorescence labelling and sorting), which may lead to unpredictable artefacts, and prevents long-term cell monitoring in the native biological environment. To detect fast moving cells in blood and lymph flows, a number of methods providing in vivo flow cytometry have been developed[44–48]. Galanzha and Zharov[49,50] noted the potential problem associated with the invasive extraction of cells from organisms generally required for conventional flow cytometric analysis and cell sorting. They describe a label free approach that employs time-resolved detection of acoustic waves induced within microcapillaries by short laser pulses (photoacoustic detection), and its application for the study the functional states of blood cells in different medical conditions, the adaption of

photoacoustic technologies to provide controlled destruction of specific cells, and the adaptation of the platform for different tissues and different organisms (Fig. 1-4).
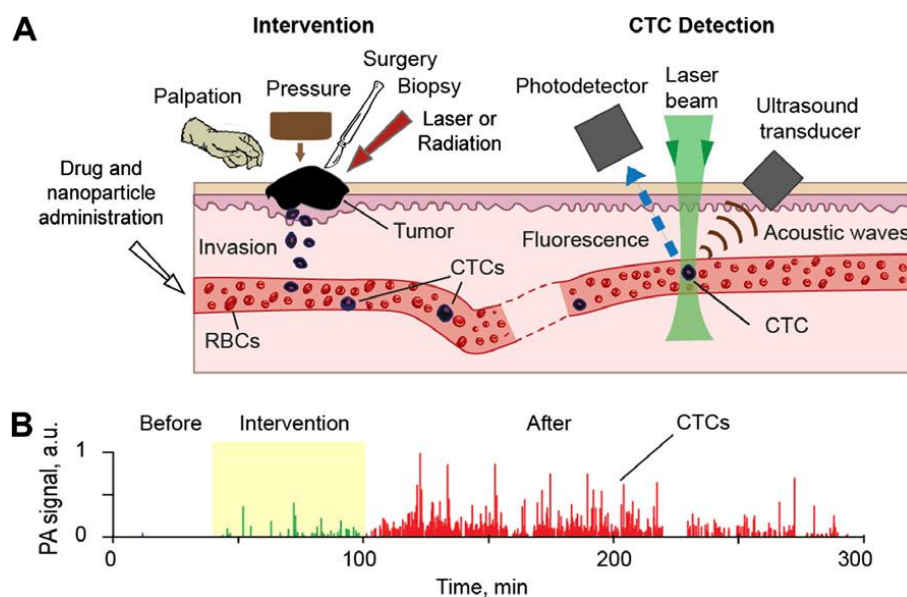
Figure 1-4 In vivo integrated photoacoustic (PA) and fluorescence flow cytometry. (A) Schematic for simultaneous detection of circulating cells (e.g., CTCs) with both absorption and fluorescence properties (right) during diagnostic and therapeutic interventions (left). (B) Example of a PA signal trace produced by melanoma CTCs in microvessels of the mouse ear before, during, and after pressure applied on ~5 mm skin tumour. Reprinted from Ref. [50,51].

1.2.3 Limitations of Conventional Flow Cytometry

Conventional flow cytometry based on spectral decoding suffers from two main disadvantages; autofluorescence interference and spectral overlap of fluorochromes.

Autofluorescence is the natural emission of fluorescence from the sample under illumination by ultraviolet (UV) or visible light. Autofluorescence can be found from both biological and non-biological samples, including endogenous molecules, cells, tissues, microorganisms and plant debris, as well as fluids and minerals. Autofluorescence typically covers a broad range in the visible spectrum and can easily dominate the fluorescence of target analytes. This is common in most of the biological samples and leads to reduced sensitivity in conventional fluorescence detection systems, especially in rare-event detection.

Spectral overlapping refers to the practical problem when multiple colours of fluorescent tags are used to confirm the presence of a target analytes (multi-colour staining) or multiple

fluorescence tags are employed to simultaneously probe different analytes in a single test. As illustrated in Fig. 1-5, conventional fluorescent tags (dyes) typically have broad bandwidth emission spectra (full width at half maximum, FWHM ranging from 50 to 100 nm). Spectral overlap resulting from such broad emission spectra results in cross-talk between neighbouring spectral detection channels which can become quite severe when the emission intensities of neighbouring channels are very different (e.g. orders of magnitude). Such spectral channel cross-talk seriously affects both the sensitivity and the specificity of identification and quantification of each targeted analyte.
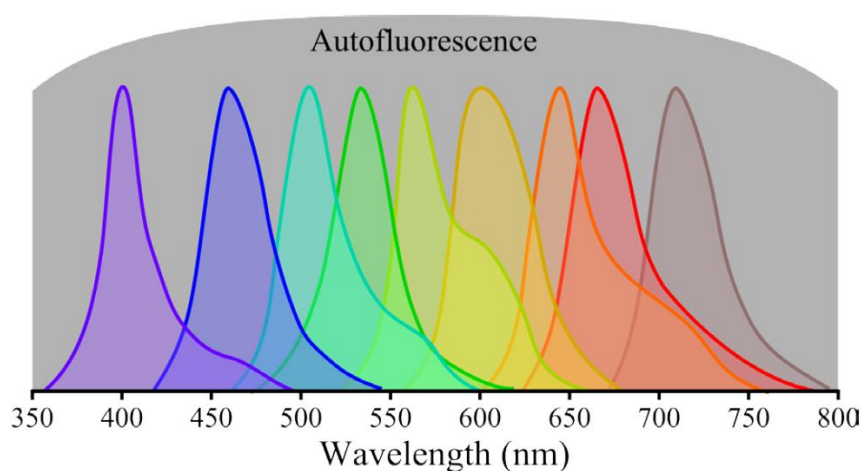
Figure 1-5 The sensitivity of conventional fluorescence techniques is limited by both issues of autofluorescence and spectral overlap of fluorochromes, stemming from the broad of fluorescence emission in the spectral domain. Reprinted from Ref. [52].

In order to achieve sensitive detection using fluorescence techniques, new methods are needed to suppress the overwhelming autofluorescence in most real samples to better differentiate target from non-target fluorescence; and the key to avoiding spectral overlapping is to create a new independent dimension which allows different spectral channels to be unambiguously identified. This can be achieved by adding to the multichannel spectral domain a multichannel temporal (i.e. lifetime coding) domain. Given that the temporal bandwidth is quite narrow, resulting from high accuracy (typically ±1%) in lifetime determination, a large number of lifetime channels can be obtained across the tens of microseconds to millisecond range with very low channel cross-talk under normal conditions.

1.3 Lifetime Detection on Flow Cytometry

The fluorescence/luminescence lifetime, often mathematically represented by the Greek symbol tau (τ), is the average time an excited fluorophore spends in an energetic state and vibrational level prior to relaxation back to a non-excited ground state. The step-wise photo-physics behind fluorescence excited state phenomena culminate in photon emission following an exponential decay kinetic process. The lifetime varies significantly from tens of femtoseconds for internal conversion to nanoseconds for fluorescence, and microseconds to milliseconds (or even seconds) for phosphorescence[53] (alternatively termed luminescence in many fields). The measurement of the luminescence lifetime with a flow cytometer is an old concept[12,13,54,55] that is experiencing a re-emergence owing to new applications and advancing technologies.

The luminescence lifetime is a parameter independent of a fluorophore's excitation and emission spectrum and thus independent of the number of photons emitted by an excitable molecule as well as the total number of excitable molecules present (i.e., fluorophore concentration). Being independent of emission intensity, the fluorescence lifetime can be used to distinguish between two or more fluorophores that have similar emission spectra. These advantages make lifetime become a detectable code in temporal dimension on top of fluorescence spectrum and intensity. Moreover, lanthanide probes with long-lived luminescence lifetime (micro-milliseconds range) can be easily distinguished from the autofluorescence (nanosecond lifetimes) emitted by most biosamples using time-gated detection methods[1,2,12,13,18,19,56–58]. Another advantage of the fluorescence/luminescence lifetime as a cytometry parameter is that it can be quantitative. With fluorescence lifetime quantification, it is possible to study basic cellular functions and phenomena such as cellular metabolism, DNA and RNA content, ATP synthesis, mitochondrial function, protein conformational changes, protein–protein interactions, protein mis-localization intracellularly, and cell signalling[15,53,54,59–67].

The existing techniques can be categorised into two ways, depending on the operational region in the lifetime dimension and methods of resolving lifetime. From the aspect of lifetime length, some systems have designed to detect probes with lifetimes in the range of nanoseconds (fluorescence), and other lifetimes in the micro-milliseconds region (luminescence). Time-domain perturbation (excitation pulsing) and frequency-domain perturbation (excitation

intensity modulation) are two primary approaches to measure fluorescence lifetime in flow cytometry.

1.3.1 Time-Domain and Frequency-Domain Detection

Today, state-of-art lifetime-based detection and imaging systems are represented by sophisticated commercially available fluorescence lifetime imaging microscopes (FLIM) systems operating in the 1-20 nanosecond time-domain and corresponding (1-100Hz) frequency-domain[68]. In contrast to the stationary samples in microscopy, the available detection time in flow conditions is limited, which imposes a serious constraint on implementing direct lifetime measurements in the flow. However, the ever-increasing speed of electronics made the implementation of the different lifetime measuring techniques also possible in flow cytometry, first the phase method pioneered by Steinkamp and his co-workers[54], then the time-domain method pioneered by Condrau *et al.*[12,13] in the form of time gated detection of fluorescence of lanthanides. Recently Cao *et al.*[69] reported on an attractive pulse-shape method situated between the pulsed and phase methods with the capability for parallelism well-matched to the high-throughput multiplex nature of flow cytometry.

The time-domain or pulsed technique, directly samples the fluorescence decay curves by short light flashes via single photon counting or stroboscopic detection. With time-domain approaches, the fluorescence decay is normally observed with single photon counting detectors, and the signal then analysed using single or multiple exponential decay algorithms. The measurement cycle is initiated by pulsing the excitation (e.g. laser) source and with precise timing collecting the emission photons after laser pulsation. The decaying emission is collected by gating a detector, which involves activating its photosensitivity simultaneous to laser pulsation and then deactivating the detector after a delay window for photons to be counted during fluorescence decay.
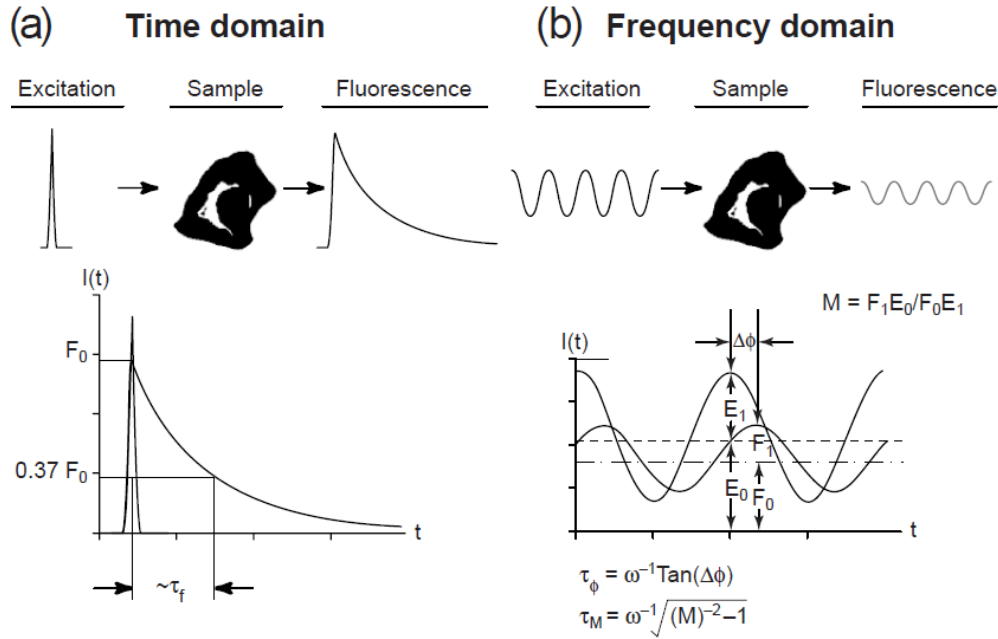
Figure 1-6 There are two general methods for the determination of fluorescence/ luminescence lifetimes. In the time domain (a), the lifetime is directly measured upon excitation of the sample with a short pulse of light, where the duration of the pulse is ideally much shorter than the fluorescence lifetime (τ_f) to be measured. This results in a fluorescence emission whose intensity decreases exponentially with time. For a sample comprising a single fluorescent species, the fluorescence lifetime is given by the time over which the fluorescence intensity drops to about 37% of its initial value. (b) In the frequency domain, the sample is excited with sinusoidally modulated light, the optimal angular frequency of which is reciprocal to the fluorescence lifetime to be measured. This results in the re-emission of sinusoidally modulated fluorescence at the same frequency as the excitation but with a reduction in the relative modulation depth, *M*, and shifted in phase, $\Delta\phi$. The phase shift and relative modulation depth can be used to calculate the phase τ_ϕ and modulation lifetimes τ_M, respectively. Reprinted from Ref. [70].

This method when integrated with flow cytometry hardware requires precise timing and is coupled with off-line analyses to fit exponential decay data and provide a fluorescence lifetime output, which can then be turned into a cytometric parameter and plotted in a histogram format. The disadvantage of the method is its long photon counting duration which results in relatively low throughput when compared with frequency-domain methods.

Some highlights of time-domain lifetime flow cytometry are exampled here. Li *et al.* developed a pseudo-time-resolved system in a fluorescence lifetime excitation cytometer by

kinetic dithering (FLECKD) of the instrument[71]. Nedbal *et al.* converted a conventional inverted wide-field fluorescence microscope into a time-domain flow cytometer by placing a flow-chip (microfluidic chamber) on the sample stage and applying time-correlated single photon counting (TCSPC)[66]. Note that time-domain cytometry involving emission lifetimes in the micro/millisecond range is usually referred to as time-gated or time-resolved flow cytometry [12,13,18,19,57].

Frequency-domain measurements involve sinusoidal (or square wave) modulation of the laser excitation source at a radio frequency (RF) of 1–100 MHz. When a fluorescently labelled cell is excited with this type of sinusoidal modulation, the intensity of emitted light, which decays as an exponential function of time, carries the same modulation frequency. However, the amplitude is attenuated and the phase is shifted owing to the fluorescence decay kinetics. The fluorescence lifetime is calculated from the information in the modulated signal using (generally) a Fourier transformation of the exponentially decayed function which depends on time[72].

The advantage of the method is its rapidity due to the efficient Fourier-algorithms, favouring multiplexing and applications for real time monitoring of dynamic events in video microscopy. However, relatively high signals are needed in frequency detection platforms. Because lifetime is an indirectly measured parameter here, lifetime heterogeneity cannot be revealed directly, though the recently introduced AB-plot technique has addressed this substantially[73].

1.3.2 Fluorescence Lifetime and Luminescence Lifetime Detection

The terms 'Fluorescence' and 'Luminescence' are widely used across various disciplines, but not always in a strictly correct basis, especially in life sciences, where 'Fluorescence' or 'Luminescence' are often used interchangeably. Both as subclasses of photoluminescence, Fluorescence is typically a fast process with decay times (lifetimes) of up to ~100 nanoseconds, while Luminescence (photoluminescence) is a unique type of photoluminescence with longer decay time after excitation, from a few microseconds to milliseconds, minutes or even several hours.

Detection scheme and methods applied to luminescence lifetime detection are different depending on the lifetime duration. The frequency-domain method of lifetime detection is normally applied to short lived fluorescence in nanoseconds range, which also can be

resolved with time domain method[70], i.e., time-correlated single photon counting (TCSPC). As shown in Fig. 1-7, TCSPC methods relies on statistical measurements of a single photon arrival time following a pulsed excitation of picoseconds or even femtoseconds over many cycles to obtain a single lifetime decay curve. However, techniques to distinguish lifetimes in this time-scale require high-speed devices and sophisticated signal processing, resulting in expensive instrumentation. Moreover, they still face the same issue of autofluorescence, since autofluorescence has lifetime in the same ns region. Therefore, it is not feasible for such techniques to suppress autofluorescence for improving detection sensitivity. Since the fluorescence lifetime typically varies significantly in this time-regime in response to many factors, such as temperature and pH, there are significant limitations to multiplexing.
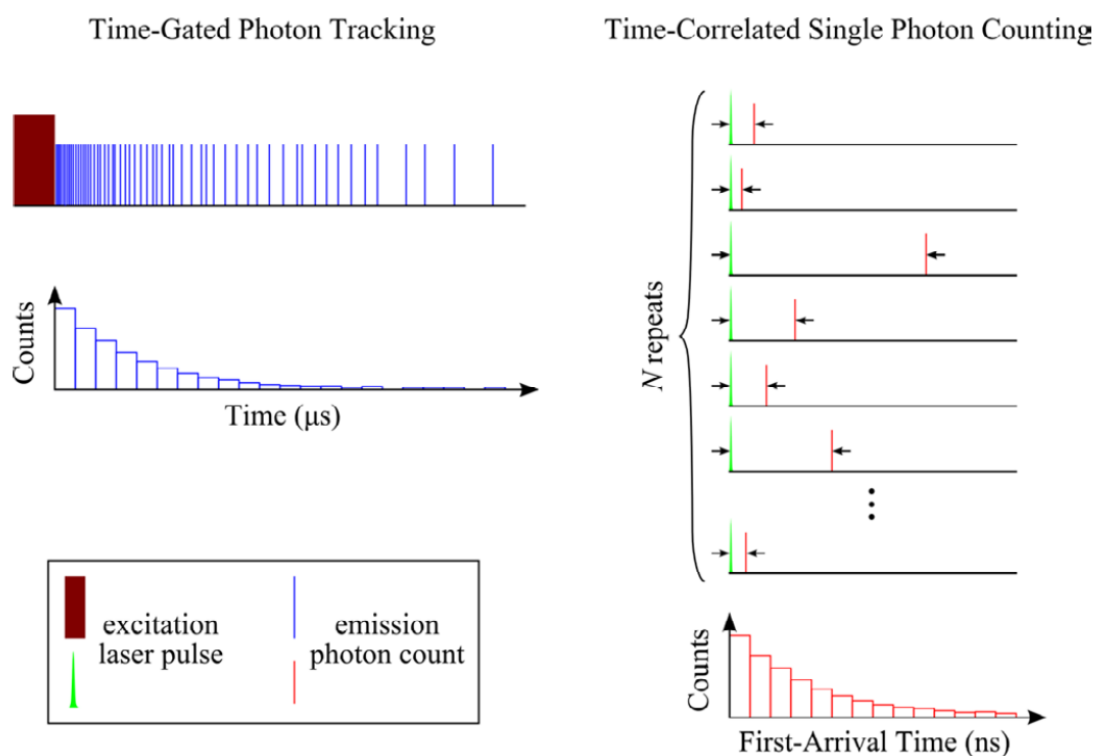
Figure 1-7 Different time-domain methods to detect long-lived luminescence (micro-milliseconds) and short lifetime fluorescence (nanoseconds). Reprinted from Ref. [2].

For decay times that become longer than about 20 ns, the complexity of TCSPC is no longer necessary. In fact, TCSPC is slow and inefficient for long decay times because of the need to use a low pulse repetitive rate and to wait a long time to detect each photon. In the past emission with long decay would be measured using a sampling oscilloscope. At present the preferred method is to use photon-counting detectors that sum the number of photons occurring within a time interval.

The principle for measuring luminescence lifetimes in the µs region, identified as the time-gated photon tracking method[2], is illustrated in Fig. 1-7. This method simplifies the time-resolved measurement of long-lifetime luminescence by directly collecting and binning many emitted photons after a pulsed excitation of tens to hundreds of microseconds, so that it becomes feasible to record the luminescence decay and fit the exponential curve with a single cycle of pulsed excitation and time-gated detection period.
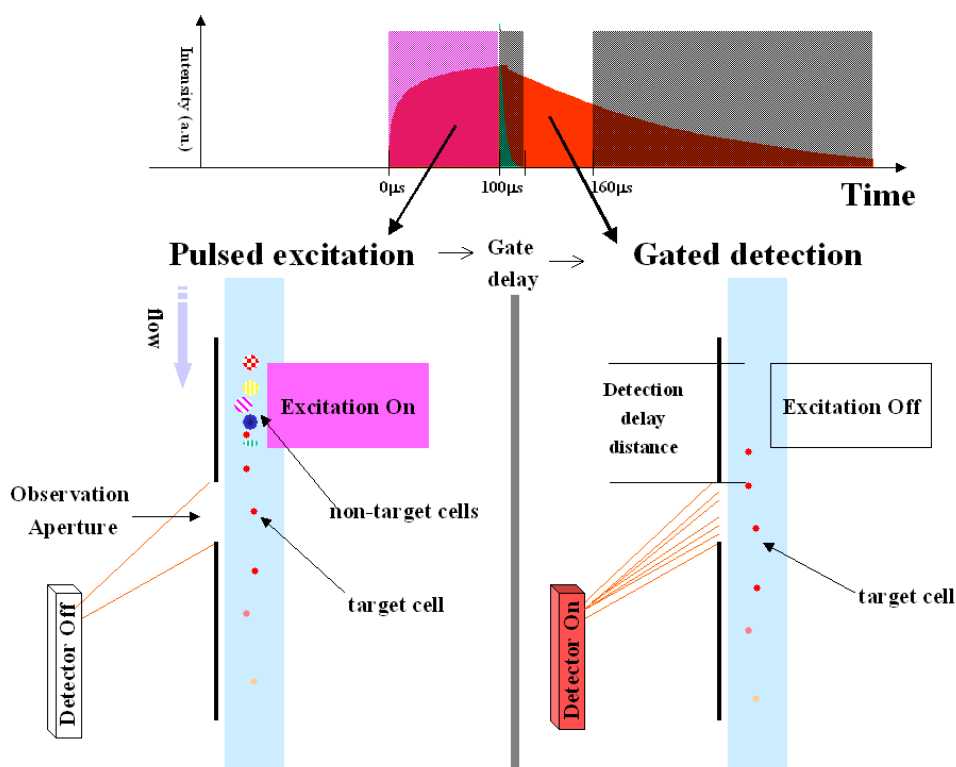
Figure 1-8 Schematics of TGL flow cytometry geometry. After an appropriate gate delay time, both light scattering and autofluorescence ceased and only long-lifetime luminescence from target cells remained to be detected. Reprinted from Ref. [57].

This scheme has been used in time-gated luminescence (TGL) microscopy, widely discussed in the literatures[2,17,53,56,74–92], to distinguish long-lifetime lanthanide probes from short-lived autofluorescence in the background. The TGL technique has also been applied in flow cytometry, firstly proposed by Leif *et al.* in the 1970s[16] to open up new opportunities using lanthanide chelates as fluorescent probes. A detailed theoretical analysis was described by Condrau *et al.* in 1990s[12,13], with the use of Eu chelates as probes with luminescence lifetime from 10 µs to 2 ms and further discussed by Jin *et al.* in 2007[18,19,57] where TGL flow cytometry was coupled with a UV LED capable of high operation rates to avoid undetected events in the dark detection time (see Fig. 1-8).

For luminescence decays with long lifetimes from lanthanide coordination complexes or other probes with long emission lifetimes, short-lifetime (<100 ns) autofluorescence background from biological specimens and scattering light is eliminated by applying a delay window with duration of 100 ns -1 μs following the excitation pulse before the detection gates open. The delay is achieved in two ways, time delay or spatial delay, as demonstrated in Fig. 1-9. For the wide-field TGL microscopy, time delay is usually chosen and implemented with a chopper[86] or gateable detector[93]. While for flow cytometry employing a TGL scheme, the delay window was initially achieved by spatially shifting the detection aperture downstream to the excitation spot in the rapid flow (normally > 1m/s)[12,13,18,19]. Subsequently a TGL flow cytometry integrating both spatial and time-delay techniques were developed to reduce the interference of the scattered excitation light in the flow stream, as shown in Fig. 1-8[94].
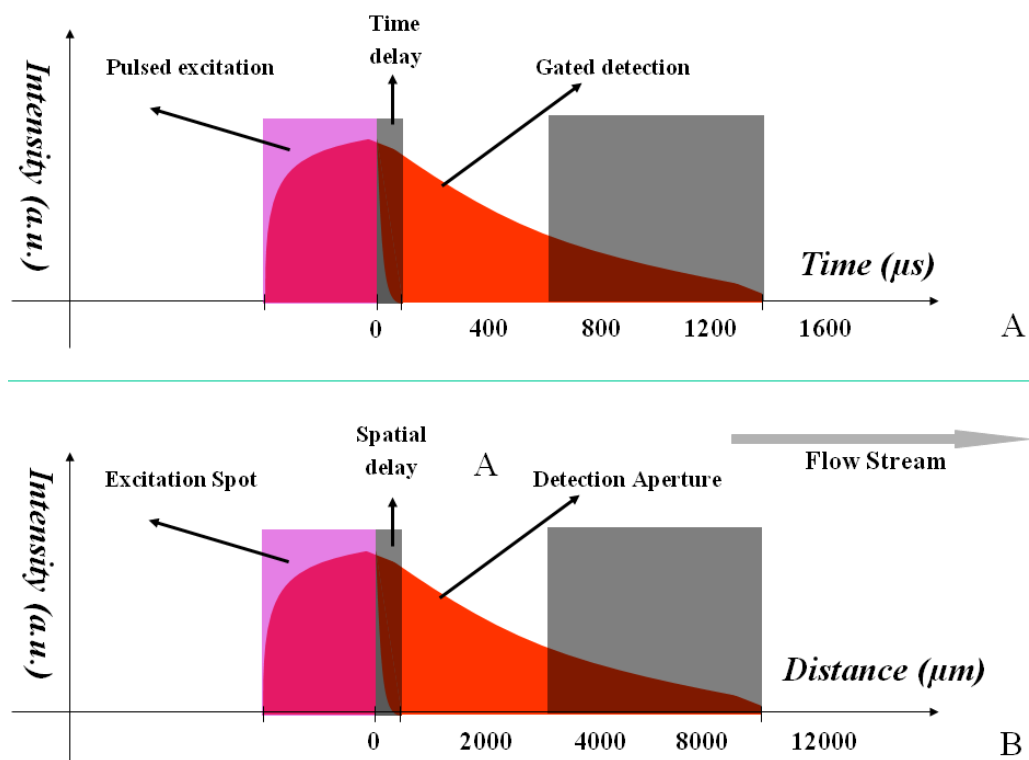
Figure 1-9 Temporal and spatial delay based TGL detection. (A) The general theory of TGL detection operation showing the large difference in luminescence decay in the temporal domain, where an appropriate time-gated detection window can eliminate both scattering and autofluorescence background; (B) Long-lifetime biomarkers in rapid flow can convert the temporal luminescence decay to a spatial decay along the flow axis (assuming luminescence lifetime 500 μs and flow velocity 5 m/s). Reprinted from Ref. [143].

1.3.3 Opportunities of Luminescence Lifetime Detection in Time-Resolved Flow Cytometry

As discussed previously, application of spectral domain detection alone imposes a number of limitations on performance: the presence of strong autofluorescence limits sensitivity and multiplexing is limited by detection-channel cross-talk due to the broad spectral width of the usual fluorochromes. It has been shown that temporal-domain coding together with spectral-based (i.e. wavelength) coding in fluorometric analysis[2,56] can achieve ultrasensitive discrimination of target signal against the autofluorescence and scattering noise from complex biosamples, and the number of multiplexed channels can be greatly increased.

However, using long-lifetime luminescent probes requires a much slower sample flow rate than are usual for the current time-resolved / time-gated flow cytometer systems. This thesis discusses a time-resolved flow cytometry which is microfluidic-based in order to decrease the flow velocity for the accurate and sensitive detection of long lifetime luminescence. The relatively slow flow stream is focused with a sheath-free technique which is based on acoustic standing waves, reviewed in the following section.

1.4 Time-Resolved Flow Cytometry in Microfluidics

In conventional flow cytometry, sheath fluid hydro-dynamically focuses cell or particle suspensions into a narrow sample stream. In combination with a tightly focused laser, this narrow sample stream creates a small interrogation volume that is analysed via high numerical (NA) aperture optics. The tight positioning ensures highly precise analysis, and the small interrogation volume enables largely homogeneous assays (wash-free), both of which are unique strengths of flow cytometry[8]. As a result, sheath flow focusing is still the most common methods that have been developed in microfluidic flow cytometers in recent years. Recently, Ligler's group[95,96] proposed a three-dimensional (3D) sheath flow focusing method by using the grooved microchannels based on the chevron design. This method created a vertical focusing. The height and width of the sample stream can be controlled by the chevrons and the sheath-to sample flow rate ratio.

Conventional sheath focusing flow cytometers can analyse cells at rates as high as 50,000 cells/s, with a high speed of flow velocity, more than one meter per second linearly. However, considering the typical laser beam height of 5-10 µm and flow linear velocity of 1-10 m/s in

the use of hydrodynamic focusing, the transit times through the analysis volume occur in a few μs, which is inadequate for the detection of luminescent targets with decay lifetimes of hundreds of microseconds to a few milliseconds. Alternative approaches to particle focusing such as acoustic[37–39], inertial[97], optical traps[98] and dielectrophoretic (DEP) positioning[99,100] have been developed and show promises in flow cytometry applications.

The introduction of chip integrated microfluidic systems has made it possible to place components in parallel along or across a microfluidic channel to achieve a number of new focusing approaches[101]. These sheath-less focusing technologies combined with microfabrication and microfluidics[36] have the advantage of concentrating particles to precise positions without the concurrent acceleration imparted by hydrodynamic focusing, which allows for high particle analysis rates at reduced linear velocities. Since these techniques do not require a sheath flow, fluid consumption and hazardous waste output are minimized[102].

Among these approaches, acoustic-based microparticle manipulation techniques appear to be ideal because they are sheath-less, non-invasive, simple-microfabrication and suitable for slow flow stream, which is the main purpose for using it on this long-lifetime detections platform. Apart from these features, acoustic standing wave technique for stream focusing is also quite well studied around academia and commercialized in industry.

1.4.1 Manipulation of Particles with Acoustic Standing Waves

Spatial control and manipulation of particulate matter in fluids by means of ultrasonic standing waves is an area that is gaining increased attention. All types of particles can be affected by ultrasonic standing wave forces as long as they differ from the surrounding medium in regards to its acoustic properties. August Kundt was the first to observe positioning of particles in an acoustic field, where he utilized dust in a resonator tube to calculate the speed of sound via the location of particles within the standing wave[103]. The fundamental theory of acoustic standing wave forces on particles has been described extensively by King[104], Gorkov[105], Nyborg[106] and Laurell *et al.*[107].

As shown in Fig. 1-10, the force induced on particles in an acoustic standing wave field is the result of both the primary F and secondary F_B radiation forces, where the primary force originates from the standing wave and the secondary forces are due to sound waves scattered by the particles. The primary radiation force (PRF) is, in general, responsible for the

strongest acoustic force exerted on the suspended particles in a standing wave field. Secondary forces are commonly in the orders of magnitudes smaller and are only influential at very short distances between particles, i.e. at very high particles densities. As an example, Ter Haar and Wyard[108] showed the relative magnitude of acoustic forces on red blood cells to be 2×10^{12} N for the PRF, the secondary interparticle force to be 2×10^9 N for cells in contact and 10^{14} N for cells 10 µm apart.
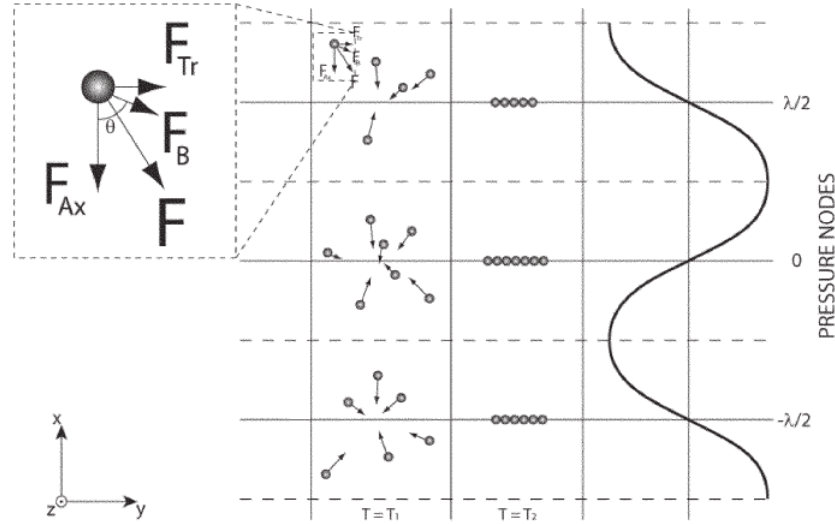
Figure 1-10 Acoustic forces that act on a particle: F_{Ax} is the axial component of the primary radiation force, F_{Tr} is the transverse component and F_B are the interparticle forces (Bjerknes forces). At time T_1 the acoustic forces have just begun to act on the particles and by time T_2 a steady state has been reached. Reprinted from Ref. [107].

The primary radiation force can be divided into the axial component F_{Ax} and the transverse component F_{Tr}. The axial PRF acts in the direction of the propagation of the acoustic wave field and is stronger than the transverse PRF, which is the cross-section of the channel. The axial PRF translates particles or cells to either the nodes or the antinodes of the standing wave. The transverse PRF is subsequently responsible for packing the particles closer together and to withhold their positions. The equations below define the axial PRF:

$$F_{Ax} = - \frac{(\pi p_0^2 V_c \beta_m)}{2\lambda} \Phi(\beta, \rho) sin2kx \qquad \textbf{(1-1)}$$

$$\Phi(\beta, \rho) = \frac{5\rho_c - 2\rho_m}{2\rho_c + \rho_m} - \frac{\beta_p}{\beta_m} \qquad \textbf{(1-2)}$$

Here V, p_0, β, ρ, λ, Φ, k and x refer to the volume of the particle or cell, pressure amplitude of the standing wave, compressibility, density, wavelength of the acoustic wave, acoustic contrast factor, wave number (defined as $2\pi/\lambda$) and the distance of the particle from the focusing nodes respectively. Subscripts c and m refer to the particle or cell and the surrounding medium or solution.

The particles are focused mainly because of the force F_{Ax}, which is proportional to particle volume and standing wave pressure amplitude squared. Because the particle volume is proportional to radius, the force drops dramatically when the particle size is decreased. And the acoustic pressure amplitude is proportional to the supplied voltage when the standing wave is driven with a piezoelectric ceramic (e.g., PZT)[109]. It follows that larger particles are more easily focused, and higher driven peak to peak voltage also assists acoustic focusing. Furthermore, the focusing force direction can be reversed as the acoustic contrast factor Φ changes, this depending on the densities and compressibility of the particles and the surrounding medium.[107] In this situation, the particles or cells will be focused in the anti-nodes instead of focusing at the nodes as in the stationary state.

1.4.2 One-Dimensional Acoustic Focusing in Rectangular Channels

Suthanthiraraj *et al.* have developed one-dimensional acoustic focusing flow channels using two different geometries, one involving fabrication in simple capillary devices, the other microfabrication by way of photolithography and deep reactive ion etching (DRIE)[38]. These acoustic focusing microchannels were integrated into in a flow cytometry system to achieve parallel multinodes one-dimensional acoustic focusing flow streams for high-throughput analysis on flow cytometry.

Fig. 1-11 shows a microchannel cross-section that is fabricated by DRIE. Silicon and glass are commonly utilized as the acoustic resonator because it can efficiently transmit acoustic power from piezoelectric actuators (e.g., lead zirconate titanate, PZT) into the fluid filled resonator chamber and display good acoustic reflection properties compared to other materials[110]. Meanwhile silicon and glass are favourable in microfabrication properties so photolithography and deep reactive ion etching (DRIE) based microfabrication techniques can be employed to create the two opposing reflector walls in the bulk material. A glass lid is used to seal the chamber of the channel and the PZT is attached underneath of the chip to provide the actuation.[38,111]
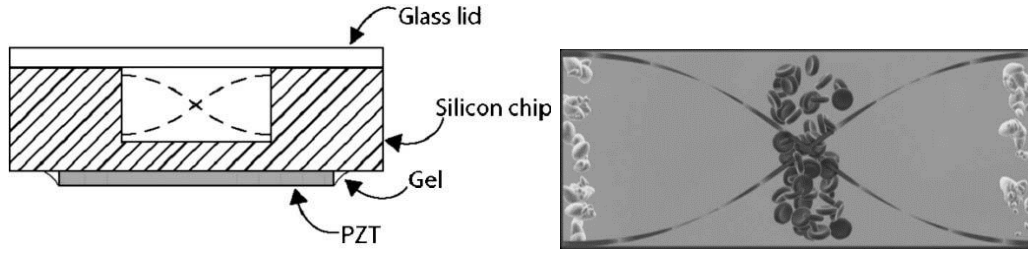
Figure 1-11 Left: Schematic cross-section of microchannel utilizing the acoustic focusing. The silicon channel is sealed by a silica glass lid and is actuated from below using a piezoelectric ceramic. Right: Illustrated cross-section of a microchannel showing negative acoustic contrast factor Φ particles (e.g. lipid particles) collected in the pressure antinodes by the side walls and positive acoustic contrast factor Φ particles (i.e. red blood cells) in the pressure node. Reprinted from Ref. [107].

Ultrasonic standing waves can be generated within microfluidic channels by exciting them with PZT, which expands and contracts with an applied sinusoidal voltage, thereby inducing periodic mechanical perturbations in the form of elastic waves that propagate through the microfluidic device[112,113]. By matching the driving frequency to a resonant mode of the micro-channel, an ultrasonic standing wave can be induced in the fluid with a discrete number of pressure nodes, depending on the ratio of the acoustic wavelength to the device geometry. Suspended particles respond to these standing waves by migrating to either its pressure node or its pressure antinode depending on the sign of the acoustic contrast factor Φ (as shown in Fig. 1-11).

To generate a single focusing node in the microfluidics, the frequency of supplied signal driving PZT has the relationship with the width of capillary channel as the following equation,

$$f = \frac{c_m N}{2L} \qquad\qquad (1\text{-}3)$$

Here, f is the frequency of the alternating current (AC) supplied signal, c_m is the speed of sound in the medium, about 1480 m/s when in water. N is the number of desired nodes or sample stream, equal to 1 for single-stream focusing. L is the width of the channel. The manufacturer varies the thickness of the PZT to establish the desired resonance frequency range.

1.4.3 Two-Dimensional Acoustic Focusing

Recently several designs that actuate the channel in both planes simultaneously (2D-focusing) have been presented[41,101,114,115]. Fundamental developments of sheath-less 2D acoustic focusing of particles in flow was first described by Goddard *et al.*[37], and this technique has been commercially applied in the Attune Acoustic Focusing Flow Cytometer (Life Technologies).
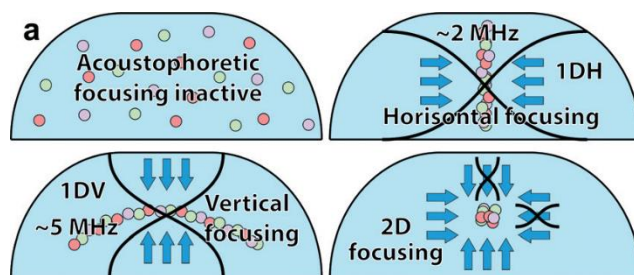
Figure 1-12 Schematics of 2D acoustophoretic alignment. Vertical (1DV) and horizontal (1DH) focusing is combined to create a 2D focusing node in a microchannel. Reprinted from Ref. [101].

Typical 2D acoustophoretic systems are designed to actuate the primary eigenmodes of the microfluidic channel such that an acoustic half wavelength standing wave is established and the corresponding pressure node is formed in the horizontal or vertical centre plane of the channel either because of wall-wall (horizontal focusing) or top-bottom (vertical focusing) resonance, as demonstrated in Fig. 1-12. Graves *et al.* proved that this can be done either by using two acoustic actuation frequencies, one for each direction, or by designing the channel in such a way that a single frequency can be used to form standing waves in both directions, when the cross-section of the microchannel is designed to be a square or a slightly off-square[41]. The two frequencies needed for 2D focusing can be provided by two acoustic actuators[116–118] or a single PZT transducer[41] driven at resonance frequency of either width or depth of microchannel cross-section. The acoustic focusing chips used in the system described in this thesis were very kindly supplied by Professor Graves.

1.5 Long Lifetime Luminescent Probes

Time-resolved fluorescence measurements with long-lifetime luminescent probes have attracted great attention because the time-resolved luminescence signals provide high

sensitivity in the detection of biomedical and environmental samples without autofluorescence interference. Additionally, the large range of lifetime from microseconds to millisecond allows large flexibility of accommodating narrow lifetime-based multiplexing channels without overlap. A variety of long-lived emissive probes have been designed and applied for bioimaging and biosensing via time-resolved photoluminescence techniques[78]. Amongst the most commonly used long-lifetime luminescent probes are organic lanthanide luminescence complexes, in-organic upconversion nanocrystals, transition metal-ligand complexes, doped semiconductor quantum dots, and non-metal probes. Applications of these long-lived luminescent probes including detection of intracellular metal cations, halogen anions, reactive oxygen, nitrogen and sulfur species, and biomolecules, and also monitoring intracellular pH values, temperature, and hypoxia with improved detection sensitivity and accuracy has been reported. Further details are given below.

1.5.1 Long Luminescence Lifetime

Fluorescence or luminescence lifetime refers to the average time that a fluorophore stays in the excited state after excitation[119]. Depending on the different electron distributions, inner structures and different relaxation processes of the excited ions, the luminescence lifetime varies from femtoseconds up to tens of seconds and even to several hours. Time-resolved lifetime measurements in the range of femtoseconds to nanoseconds requires sophisticated systems and expensive hardware, while luminescence with very long lifetimes compromise the signal strength due to the reduced photon emission. Compared to the short-lived fluorescent materials with lifetime less than nanoseconds and long-persistence (afterglow) luminescent materials with emission lifetime longer than several seconds, luminescent materials with emission lifetimes in the range of microseconds to milliseconds have useful properties for high-contrast analytical science and offer a balance between hardware requirements and the speed of analysis.

The long-lifetime luminescence phenomenon is governed by the electron spin selection rule and the Laporte selection rule in quantum mechanics. The spin selection rule states that electrons can only transit between energy levels with an identical spin quantum number, while other transitions, e.g. between singlet states to triplet states, are spin forbidden. The Laporte rule is a spectroscopic selection rule that applies to centrosymmetric molecules and atoms. It states that in these cases, electronic transitions that conserve parity are forbidden,

for instance, *d-d* transitions and *f-f* transitions. Allowed transitions must involve a change in parity, such as *d-f* transitions.

In reality, however, such forbidden transitions can happen, although usually with much lower probability compared to allowed transitions. An example of a forbidden transition is the well-known phosphorescence which relies on the radiative transitions from triplet excited states to the singlet ground state. Lanthanides and transition-metal complexes are noted for their long luminescence lifetimes owing to the spin-forbidden nature of their luminescence. Fig. 1-13 shows the Jablonski diagram of typical absorption, fluorescence and delayed fluorescence (phosphorescence) processes in lanthanide(III) chelates, which encapsulates the broad phenomenon of photoluminescence. The ground state and the first singlet and triplet excited states are depicted by S_0, S_1, and T_1, respectively. After absorption of a photon, long-lived lanthanide probes do not emit immediately but undergo intersystem crossing before radiative decay to the ground state. A small energy gap between S_1 and T_1 can facilitate the intersystem crossing process. The delayed fluorescence shows a substantially elongated lifetime in the microsecond scale.
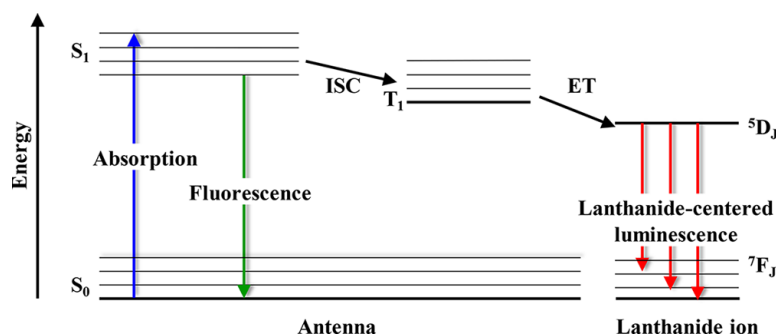
Figure 1-13 Simplified Jablonski diagram illustrating the photoluminescence processes in lanthanide(III) chelates. ISC = intersystem crossing and ET = energy transfer. Reprinted from Ref. [78].

1.5.2 Probes with Long Luminescent Lifetime

In Tab. 1-1 we summarise typical metal ions that are often used to synthesise the long-lived luminescent materials. The long-lifetime (from several to hundreds of microseconds) of these luminescence materials arises either due to the energy transfer from the triple state to the singlet state or due to *f-f* transition, both of which are commonly considered as the forbidden transition processes as we discussed above. Considering the excitation and emission wavelengths, most of these rare earth ions (except Yb-Tm and Yb-Er pairs of

elements) exhibit down-conversion luminescence mechanism, absorbing excitation at shorter wavelengths and generating emission at longer wavelengths, when they are linked with organic frames/ligands.

Table 1-1 Long-lived luminescent probes.

Element	Mechanism	Example Form	Typical Peak Excitation (nm)	Typical Peak Emission (nm)	Typical Lifetime (µs)	Quantum Efficiency	Ref.
Ru*	T→S	bipyridine complex	350	600	148	0.071	[141]
Rh*	T→S	diimine complex	310	505	162-176	0.008-0.017	[139,140]
Pd*	T→S	porphyrin complex	380	660	1100	0.17	[138]
Ir*	T→S	polypyridine complex	280	560	11.38	0.0792	[136,137]
Pt*	T→S	porphyrin complex	400	680	45.8	0.05	[135]
Eu†	4f→4f	β-diketone complex	325	610	384	0.506	[132–134]
Tb†	4f→4f	phenylpyridine complex	325	545	2700	0.58	[131]
Sm†	4f→4f	trifluoroacetone complex	360	650	96	--	[130]
Dy†	4f→4f	trifluoroacetone complex	315	575	27	--	[129]
Er†	4f→4f	upconversion nanocrystal	980	540,	20~550	0.00005-0.003	[17,128]
Tm†	4f→4f	upconversion nanocrystal	980	455,475,650,800	25~670	0.0045-0.012	[1,127]
Au*	T→S	Cyclometalated complex	UV/Vis	530	5~270	0.101	[126]
Re*	T→S	Proteinbound luminophore	290	550	2.7	0.05-0.12	[125]
Ag*	T→S	Supramolecular complex	355	412	3.9, 4.9	--	[124]
Cd*	T→S	Coordination polymers	340	510	120 and 1200	--	[123]
Mn*	3d→3d	Doped Semiconductor nanocrystal	365	570	50~1000	0.7	[122]
Si	T→S	Silica nanoparticle	365	460	60	0.1	[121]
PK‡	T→S	Protein Kinase ARC-Lum probes	337	675	19~266	0.7	[120]

Note: (*) indicates transition metal probes and (†) lanthanide probes. (‡) protein. T: triplet stage; S: singlet state.

The lanthanides comprise 15 chemical elements with atomic number from 57 to 71. Excepting Lanthanum (La) and Lutetium (Lu), the remaining 13 elements typically form trivalent ions Ln^{3+} with the similar electron configuration of

$$1s^2\ 2s^2\ 2p^6\ 3s^2\ 3p^6\ 3d^{10}\ 4s^2\ 4p^6\ 4d^{10}\ 4f^{0\sim13}\ 5s^2\ 5p^6,$$
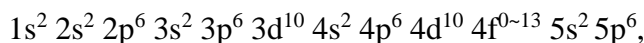
often represented for brevity as $[Xe]\ 4f^{0\sim13}$. The partially-filled 4f orbitals shielded by 5s and 5p electrons provide well-defined energy levels which are only weakly influenced by physical and/or chemical surroundings, as depicted by the well-known Dieke Diagram[142] for depicting energy levels of Ln^{3+} in $LaCl_3$. Consequently, the emission peaks of lanthanide (III) 4f-4f transitions are characteristic of the elements, and have much narrower spectral bandwidth compared to other luminescent materials.
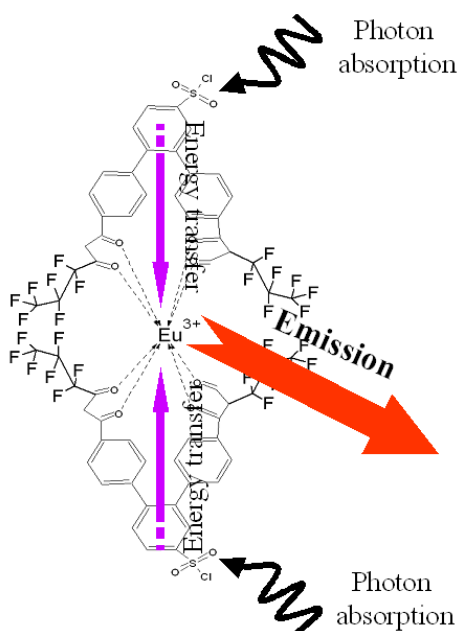
Figure 1-14 Schematic diagram illustrates luminescence from a lanthanide complex (lanthanide ion chelated by an organic antenna ligand). The antenna ligand absorbs the excitation photons then transfers the energy non-radiatively to the lanthanide ion that emits long-lived luminescence. Reprinted from Ref. [143].

A variety of organic ligands/chelates have been designed to form luminescent complexes with Ln^{3+} ions, so that they can absorb excitation light more efficiently and transfer the sensitized energy to Ln^{3+} for luminescence emission, as shown in Fig. 1-14. These ligands also function as a scaffold for biomolecular conjugation and cell staining. Developing long-lifetime lanthanide bioprobes started in the late 1970s coincident with conception of the TGL

method, leading to development and implementation of four lanthanide probes (Eu, Tb, Sm, Dy) in the 1980s[144–147]. In 1998, Yuan *et al.* developed a new Tetradentate β-diketonate-europium chelate (BHHCT) with long lifetime around 500 µs and high quantum yield of 20%, and successfully bound it to proteins for time-resolved fluoroimmunoassay[133]. In 2001, Yuan *et al.* reported a new nonadentate ligand (BPTA) to chelate Tb^{3+}, with a luminescence quantum yield of 1.00 and lifetime of 2.681 ms[131]. In 2012, Zhang *et al.* developed new class of Tetradentate β-Diketonate-Europium Complexes (BHHBCB with 40% quantum efficiency and lifetime of 0.52 ms) that could be covalently bound to proteins as biolabels for highly sensitive time-gated luminescence bioassay in clinical diagnostic and biotechnology discoveries[132]. Recently, Sayyadi *et al.* have developed a novel biocompatible europium ligand BHHTEGST displays superior synthesis yield, stability, binding and emission characteristics (40% quantum efficiency)[148]. These major advances in materials have enabled lanthanide complexes to be applied for a variety of biosensing and bioimaging applications. For the present experiments, long-lifetime lanthanide-chelate probes are used; these include those (e.g. Eu-BHHCT) used in previous reports of time-resolved flow cytometry[12,13,18,19], and more recent Eu complexes (e.g., Eu-BHHBCB) with enhanced stability and emission characteristics.

1.5.3 Applications of Long-Lifetime Probes

As a dominant signal transduction strategy to probe cellular or subcellular targets in the past decades, the target molecules are tagged by a reporter dye featuring distinctive optical properties typically colour (wavelength) in fluorescence-based detection[149,150]. Conventional fluorescence bioprobes, including organic dyes and fluorescent proteins are usually sensitive enough to label and detect subcellular information. However, many naturally occurring substances are autofluorescent under UV or visible wavelength excitation, and traditional fluorescence bioprobes lose much of their relative sensitivity in the presence of strong autofluorescence. This is particularly true in the detection of rare events. Another difficulty in microbial cell detection is that microorganism of interest usually exists in an immense pool of other microorganisms, which constitute an enormous source of background. Probes with long lifetime luminescence can easily remove the interference of autofluorescence and scattering in the background (as in Fig. 1-15), quite suitable for the applications of waterborne and foodborne pathogen detection[1,2,17] and bioimaging and biosensing, e.g. urine[82] and blood samples from patients[88].
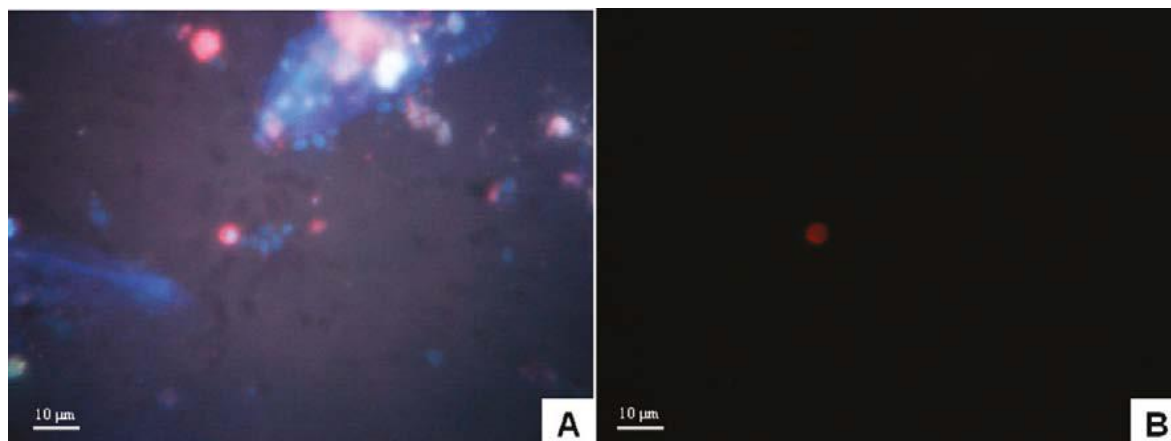
Figure 1-15 Fluorescence (A) and time-resolved luminescence (B) images of a Eu^{3+} complex labelled *Cryptosporidium parvum* oocyst within fruit juice concentrate. Reprinted from Ref. [151].

The excited state lifetimes (and quantum yields) of lanthanide complexes are strongly dependent on the coordination environment of the lanthanide ion[119]. The lanthanide chelates can be loaded into cells by permeation/uptake[152–154] or immunoassay methods[132]. Binding events, changes in hydration/solvation and changes in ligand coordination mode to Ln^{III} can each fundamentally affect the emission lifetime of the complex, inducing changes of hundreds of µs in some cases[155]. More specifically, the luminescent lifetime τ of lanthanide complex can be influenced by a number of biochemical components in the intracellular/intercellular environment[59,156,157] and lifetime may even be different for different growth phases of the same cells. With lifetime quantification, it is possible to study basic cellular functions and phenomena such as cellular metabolism, DNA and RNA content, ATP synthesis, mitochondrial function, protein conformational changes, protein–protein interactions, protein mis-localization intracellularly, and cell signalling[15,53,54,59–67,158,159] by applying the long-lived luminescence probes without cellular autofluorescence.

1.6 Thesis Outline

Flow cytometry is a broadly-applied methodology in bioscience research and clinical practice for high-throughput identification and characterization of particles, cells or microorganisms suspended in fluid samples. However, conventional flow cytometry based on spectral decoding suffers from autofluorescence interference and spectral overlap of fluorochromes. Time-gated luminescence (TGL) detection combined with long lifetime

probes is highly effective in removing the autofluorescence noise arising from the non-target cellular background of biosamples and providing high detection sensitivity and contrast. In conjunction with sheath-less acoustic focusing techniques applied on microfluidic flow cytometry, the so-called time-resolved microfluidic flow cytometry (TRMFC) developed in this thesis is able to detect the luminescence signal from long-live probes accurately and sensitively. A flow diagram of the reviewed literatures about the related topics in the above sections is summarized in Fig. 1-16.
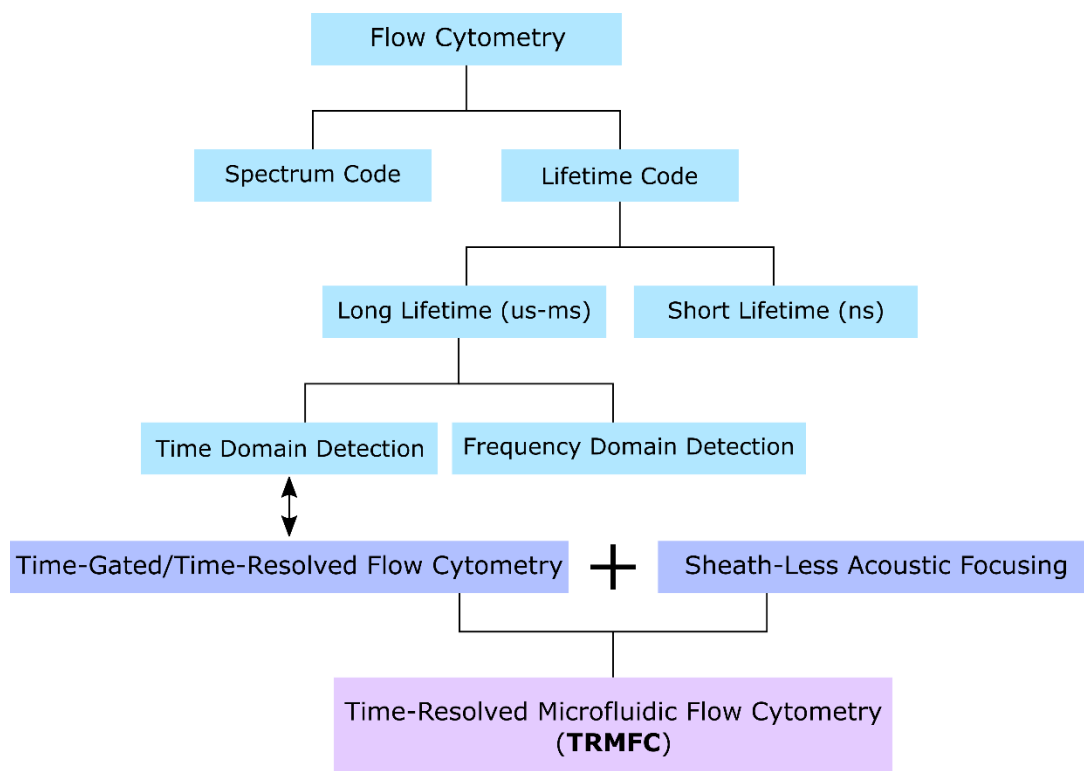
Figure 1-16 Flow diagram of the reviewed literatures in topics of flow cytometry.

This thesis reports results design, construction and operation of time-resolved microfluidic flow cytometry (TRMFC) employing acoustic focusing of the sample stream and methods for long lifetime luminescence detection, aimed at background-free, lifetime-based multiplexing biosensing in practical low-cost devices. The outcomes of the project are presented in the main body of the thesis in the following four chapters.

Chapter 2 describes the instrumental design of the time-resolved microfluidic flow cytometer (TRMFC). To enable temporal detection in flow cytometry for long-lifetime luminescent probes, firstly the flow velocity must be decreased compared to the conventional flow system. Here we utilize a microfluidic channel coupled with acoustic PZT chip for stream focusing in a relatively slow flow rate. The instrumental design, components selections and settings

of the microfluidic, the optical illumination and detection, and the electronic control system are presented in this chapter.

Chapter 3 illustrates how the acquired luminescence signal data is processed and the method of decoded overlap of events in detail. The data is analysed to extract lifetime measurements in real-time, and the operating parameters are optimised to ensure accurate lifetime determination and maximum sample throughput. To detect the luminescence with a long decay, the excitation and detection optical apertures are both wide-field, which allows that several detection events may occur in the observation window simultaneously (event cross-talk or overlap). Overlap probability in wide field detection was analysed and according to this, optimised settings for the parameters detection aperture size, flow velocity and sample concentration for the time-resolved microfluidic flow cytometry were provided. Analysis of signal trains for overlapping events has been undertaken: dual-event overlap can be resolved using a computational fitting program which inspects the length and the peak of the signal profile. Multiple overlap of more than 2 events in one detection cycle are rejected from subsequent analysis for lifetime, intensity and counting data.

Chapter 4 reports the evaluation of capabilities (i.e. determination of lifetime, intensity and counting efficiency) of the time-resolved microfluidic flow cytometer with calibrated samples of Eu doped polymer microbeads. These results are cross-validated using time-gated orthogonal scanning automated microscopy (OSAM) conducted for the same samples. The effect of acoustic focusing on the determination of lifetime, intensity and counting efficiency is also analysed for different flow rates.

Chapter 5 reports the development of a pilot lifetime-multiplexed bioassay by staining two cell lines with three different types of Eu chelates. The factors that could affect the luminescence output of the Eu chelate stained cells, i.e. lifetimes and intensities, are analysed in subsequent sections. Finally output-stabilized DU-145 stained by Eu-BHHCT and C3 by Eu-CDHH were selected into the lifetime-multiplexing panel, and their distinct lifetime and intensity ranges enabled demonstration of lifetime-based multiplexing detection on TRMFC.

Chapter 6 summarises the key research outcomes and main technical results of the TRMFC in this thesis, and discusses the future prospects and opportunities of improvement of this technology, including engineering of the microfluidic device, optimisation of operating

conditions, validation of analytical results, and ultimately application to real biomedical diagnostics.

Chapter 2:   Instrumentation

2.1 Introduction

2.1.1 Background of System Design

The current approach to discriminating multiple target cells from a biosample of complex composition with flow cytometry is primarily based on measuring the intensities of a range of fluorescent or luminescent bioprobes with different emission wavelengths (colours) typically spanning the visible spectrum. This is called spectral multiplexing. However, the sensitivity and selectivity of detection for individual colour-coded fluorescent probes is commonly limited by strong cellular autofluorescence covering a broad spectral range which masks the target spectral detection channels. Furthermore, emission wavelengths and bandwidth of the spectral detection channels must be carefully selected to prevent overlap, i.e., cross-talk, between neighbouring spectral channels, which limits the number of resolvable spectral channels that can be implemented, especially where the intensities in different channels are substantially different. It follows that a major challenge remains in analysing complex biosamples, like blood and urine, for multiple analysts of interest.

These key limitations of spectral multiplexing can be substantially addressed using *temporal* multiplexing, whereby luminescent bioprobes with a single emission wavelength can instead be distinguished by their different characteristic luminescence lifetimes. Because cellular autofluorescence typically has short lifetimes, 1-10 ns, use of long-lifetime luminescent probes (for example, lanthanide-based probes with lifetimes from tens of microseconds to milliseconds) in conjunction with simple delay-gate detection methods enables autofluorescence signal to be effectively suppressed, while simultaneously differentiating probes with different lifetimes to enable temporal multiplexing. Further, the multiplexing capability can be readily extended by combining lifetime coding with a number of spectral (colour-coded) channels.

To enable temporal multiplexing in flow cytometry using long-lifetime luminescent probes, it is necessary to design the flow system to enable the probe lifetimes to be measured

individually with high detection accuracy, and to achieve maximum throughput with minimal crosstalk arising from immediately prior or subsequent targets. There are several key issues which need to be taken into account in such system design:

i. The hydrodynamic focusing technique commonly used to focus the sample on-axis in conventional flow cytometers requires high sample stream velocity, typically at least 1 meter per second linearly, resulting in analysis rates approaching 50 000 sec^{-1} on particle-by-particle basis. That means the transit time across the detection window is usually less than 20 μs, too short a duration to collect sufficient data to determine luminescence decay-times in the hundreds of microsecond or milliseconds. It follows that sample flow velocities for time-resolved microfluidic flow cytometry based on lanthanide probes need to be at least 50 times slower than for conventional flow cytometers, so that hydrodynamic focusing is no longer viable. Sample flow velocities ~20 mm/s suggest the use of microfluidic flow devices, but how then can the target cells/particles in the sample be forced into a single, on-axis stream to enable sequential analysis of single targets as in conventional flow cytometry?

ii. The transit time of target events across the detection window can be increased by extending the detection window along the flow direction to enable longer lifetimes to be determined. But what are the limits to extending the detection window?

iii. The background autofluorescence signal can be suppressed using what is effectively a time-gating technique wherein the excitation and detection apertures at the sample are separated by a distance related to the flow velocity, but can this same purpose be realised with a simpler instrumentation design?

Addressing these key questions have been central to the design of the microfluidic time-resolved flow cytometer described below. Analysis of operating conditions optimised to achieve maximum detection throughput and precision in lifetime determination will be discussed in Chapter 3.

2.1.2 Overview of Time-Resolved Microfluidic Flow Cytometer

The key systems comprising the time-resolved flow cytometer which has been developed in this project are the microfluidic flow system, the optical illumination and detection system, and the electronic control system, as illustrated schematically in Fig. 2-1.
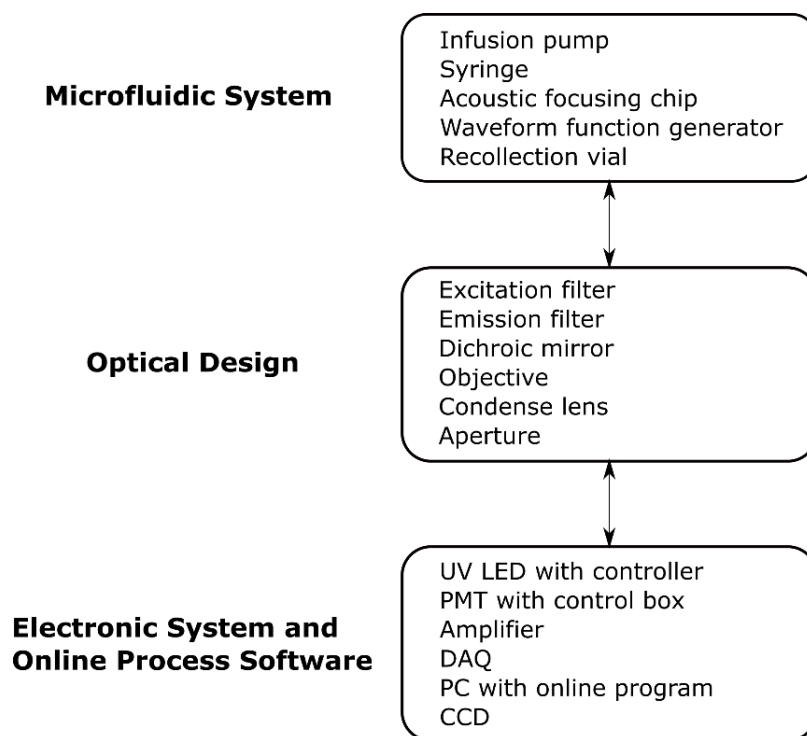
Figure 2-1 Overview scheme of the time-resolved microfluidic flow cytometer.

The heart of the microfluidic flow system is an acoustic focusing microfluidic chip capable of delivering target (particles/cells) well focused in the centre of the microfluidic channel cross section over the length of in the detection window, and which maintains a sample flow velocity allowing sufficient transit time across the detection window to measure luminescence lifetimes in the 100 µs to 1 ms range.

The optical excitation and detection system are based on a commercial epifluorescence microscope with modified optical excitation source (UV LED 365nm) and detector (PMT), including band-pass filter for emission at 615 nm from Europium complex luminescent probes. A single photon counting sensor (PMT) is used to acquire luminescence signal intensity, and a digital camera for recording images.

Electronic system provides control signals for pulsed operation of the UV LED excitation source and delay-gating of the PMT, and also for detection and processing of the fluorescence signal, and subsequent signal acquisition through DAQ to PC for later data analysis. The control signals were synchronised by an on-line Labview program, which also sampled the amplified voltage-converted fluorescence signal for lifetime decoding and event counting.

2.2 Microfluidic Flow System

The key component of the microfluidic flow system is the purpose-designed microfluidic flow channel incorporating the acoustic focusing chip (acoustofluidic system). The microfluidic flow system is completed by standard microfluidic system components including infusion pump, syringe, and sample recollection vial, as shown in Fig. 2-2.
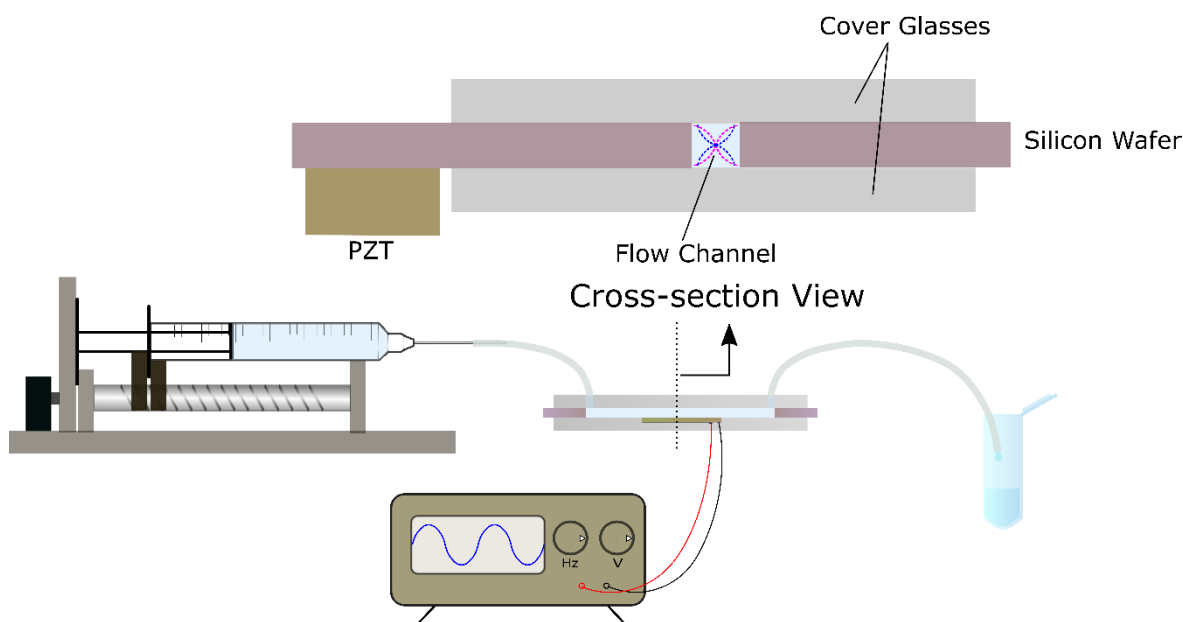
Figure 2-2 Acoustic focusing microfluidic system.

The design of the microfluidic flow channel is subject to a number of constraints. The cross-sectional dimensions must be chosen to provide laminar sample flow with linear velocities giving transit times across the detection window appropriate for measuring the expected luminescent lifetimes, but at the same time need to be matched to a half-wavelength of the acoustic focusing signal to provide focusing along the central axis of the flow channel. The length of the flow channel must be chosen to allow adequate length of the optical detection window, and also provide for pump pressures within an acceptable range. Overall it is desirable to maximise sample flow rate so that sample processing times are as high as possible. Chapter 3 details how the various flow parameters, dimensions of the optical detection window, and excitation and detection cycle parameters are optimised to achieve best lifetime measurements at maximum target detection rates.
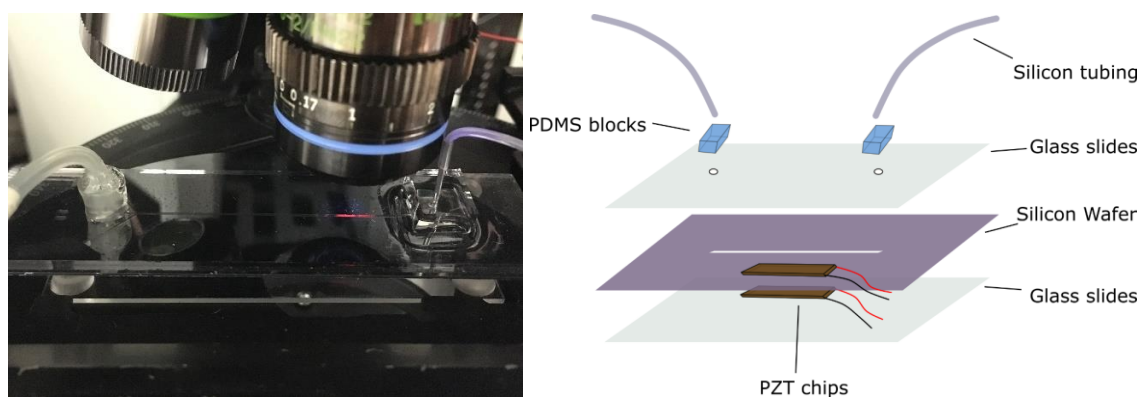
Figure 2-3 Microfluidic flow chip and fabrication process[111].

The microfluidic flow channel was fabricated from a silicon wafer (length: 90 mm, width: 35 mm, thickness: 0.52 mm) which was subsequently sandwiched between two glass slides (see Fig. 2-3), A slot with width of 0.58 mm was created in the silicon wafer using standard deep reactive ion etching (DRIE) technique. The silicon wafer was sandwiched between two glass slides (dimensions 25 mm × 90 mm × 1 mm) by anodically bonding (410 °C, 1.2 kV, 30 min),with inlet and outlet holes provided on the top slide, to give a 0.52 high × 0.58 mm wide rectangular cross-section flow channel[38]. A PZT chip (30 mm × 5 mm) with positive and negative soldered leads was bonded with super-glue to the underneath side of silicon wafer to provide the acoustic focusing transducer. A second PZT serving as a feedback monitor, and identical to the drive PZT, was attached on the opposite (top) side of the drive PZT. The feedback PZT allows the precise acoustic resonance frequencies of the drive PZT to be determined. Flexible silicon tubing was added at the inlet and outlet holes and sealed with PDMS blocks. The microfluidic chip was securely mounted onto the XY stage of a commercial epifluorescence microscope (BX 51, Olympus), with the microfluidic flow channel directly underneath the objective.

Figure 2-4 Nexus 3000, Chemyx pump.

Liquid samples are drawn into syringes of appropriate volume taking care to avoid air bubbles. The chosen syringe is mounted on a commercial syringe pump (Nexus 3000, Chemyx, shown in Fig. 2-4), which is compatible to syringes with size from 0.5µl to 140ml. The flow rate can be set on the pump panel within a large range from 1.6 pl/min to 150 mL/min with a step resolution of 0.012 microns that ensures precise infusion and withdrawal rates. When the microfluidic flow system is activated, target (luminescent) particles well-suspended in the liquid sample travel from the syringe through silicone rubber tubing (inner diameter: 1/16 inch, outer diameter: 1/8 inch) and then into the acoustic focusing microfluidic flow channel for detection. After analysis the sample is recollected in a polypropylene vial. The particles in the microfluidic channel are forced in the centre of the stream by standing acoustic waves generated by the PZT chip, which is activated by the signal from a dual-channel waveform function generator (DG1022, Rigol Technologies, Inc., see in Fig. 2-5).

Figure 2-5 DG1022, RIGOL, Arbitrary waveform function generator.

2.2.1 Acoustic Focusing in the Microfluidic Flow Channel

The strength of acoustic focusing is proportional to supplied voltage squared[107], thus increase in the applied voltage results in higher pressure amplitudes, and thus, more rapid acoustophoresis. The peak-to-peak voltage of the sinusoidal drive signal was set to $20V_{pp}$ so as to achieve best focusing results.

According to Equation 1.3 in Chapter 1.4.2, the resonance frequency is determined by the microchannel size. For the chosen cross section dimension of the rectangle chamber is 0.52 × 0.58 mm, the theoretical resonance frequencies for water sample are calculated as 1.276 MHz for single node stream focusing in horizon direction and 1.423 MHz in vertical direction respectively. To get an accurate determination of the resonant frequency in practice,

we performed a frequency sweep at a 10 kHz and then 1 kHz step near the expected resonant frequency, whilst measuring the response signal from the feedback PZT. The frequency observed at the feedback PZT was identical to that of the drive PZT, but the amplitude varied sharply as the resonant frequency was approached from either side. Using this technique, the empirical resonant frequencies were determined as 1.272 MHz and 1.430 MHz for the horizontal and vertical directions respectively.

Note that the resonant frequency is set entirely by the height and width of the chamber cross-section for given sample density. Sample flow velocity or target particle size do not have any significant influence on resonant frequency.
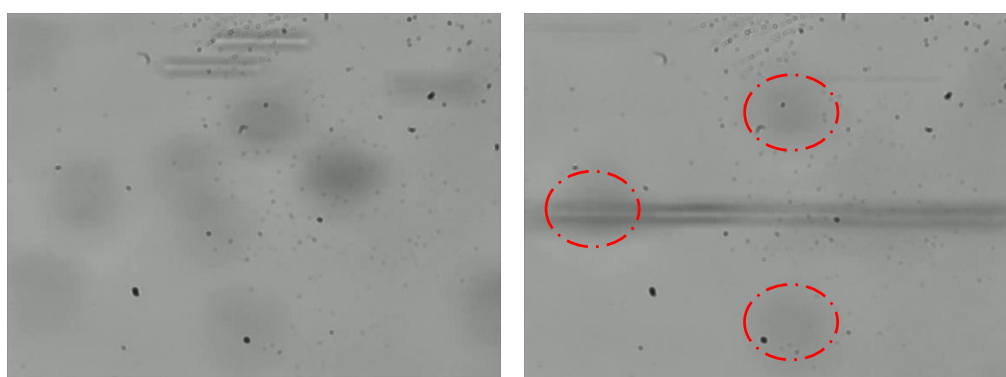
Figure 2-6 15 µm blank polymer beads suspended in MiliQ water, travelling at 0.01 ml/min before and after acoustic focusing is switched on at 20V$_{pp}$, 1.272 MHz AC drive-signal. The beads are seen to be well-focused in horizontal direction, though black dots shadow in right chart (labelled with red dash circles) indicate some beads are not manipulated into the focusing stream but moving in lower layer of microchannel.

2.2.2 2D Acoustic Focusing

From Fig. 2-6 it is evident that in the horizontal focusing mode, while the majority of the particles are well focused in a single stream on the microscope focal plane, there remain some particles travelling slowly, unfocused in the bottom of the flow channel layer. Because the polymer beads are slightly denser (about 1.05 g/cm^3) than the MiliQ water (1.00 g/cm^3), they tend to settle towards the bottom of the flow channel as they progress along the channel, especially when the flow velocity is low. This can be addressed by adjusting the density of the sample with added saline, however, it is impractical to do so where the sample is of a complex nature. A more practical solution is to generate a vertical force in the flow channel

so as to focus the target particles in the vertical plane, and this has been achieved by applying simultaneous acoustic focusing in both the horizontal and vertical planes, that is, 2D focusing.
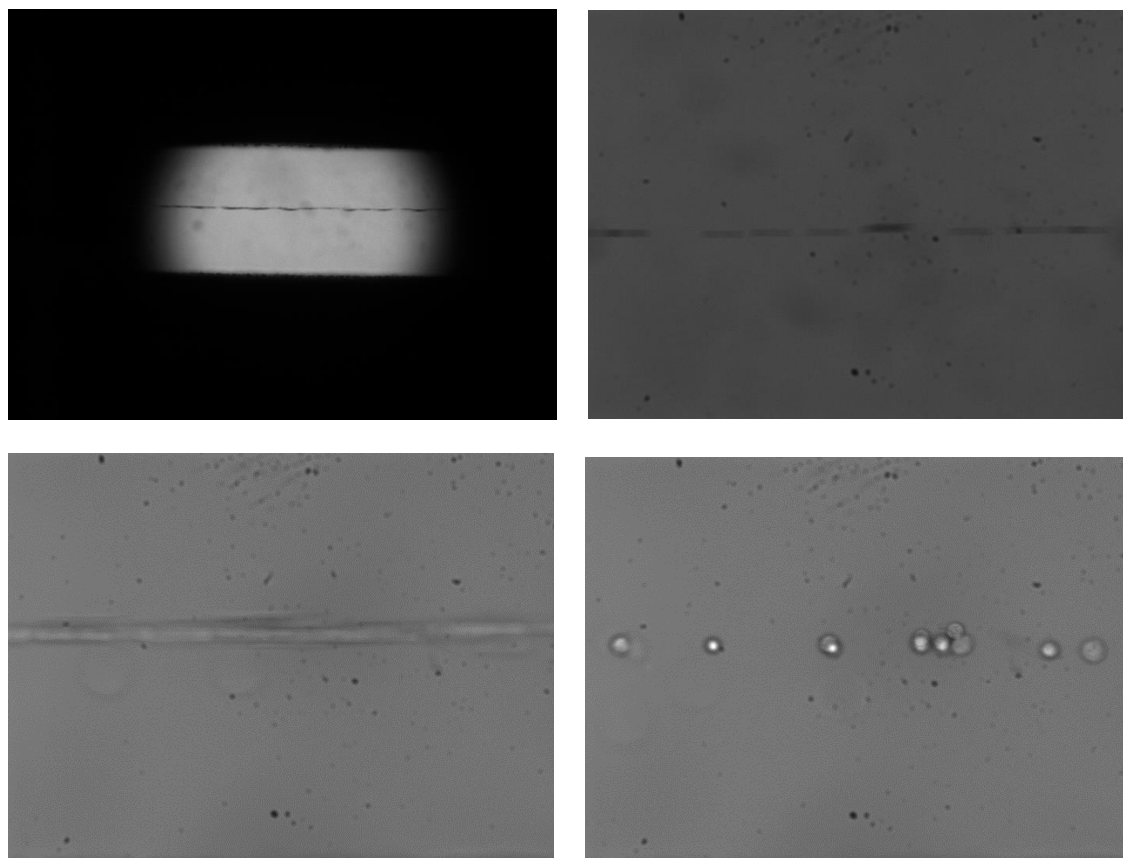
Figure 2-7 2D acoustic focusing: 8.5 µm blank polymer beads (upper panel, 10X, Edmund, NA 0.25) and DU-145 cells (lower panel, LUCPLFLN 40X, Olympus, NA = 0.6), flowing at 0.01 ml/min.

2D acoustic focusing can be achieved by switching the PZT drive frequency from the horizontal resonant frequency (1.272 MHz) to the vertical resonant frequency (1.430 MHz) at a cyclic rate determined by the time required to establish effective focusing. As particles in the microchannel require about 200 ms to be well focused[41], so the cycling rate between frequencies should be no more than 5 Hz. The PZT drive for 2D focusing was set as 20 V_{pp} sinusoidal AC at 1.272 MHz for horizontal and 1.430 MHz for vertical focusing, at a 5Hz cycle rate.

2.2.3 Maximum Flow Velocity in Microfluidic Channel

Though the resonance frequency for acoustic focusing is independent of sample flow velocity in the microfluidic channel, the flow velocity can affect the focusing efficiency.

This is because approximately 200 ms duration is required to ensure target particles in the microfluidic channel are well-focused on-axis, and if the flow velocity is such that the transit time through the effective PZT acoustic focusing zone is less than 200 ms, then focusing is adversely affected. Focusing can be improved by increasing the drive voltage up to 50 V_{pp}, but for such high-voltage drive heating of the PZT becomes excessive, increasing risk of damage to the device. In practice, we have set the maximum PZT drive voltage at 20 V_{pp}.

Target luminescent micro particles or cells of interest in the current project have diameters normally in the range 5 µm to 20 µm, thus 5 µm polymer beads have been used to determine the maximum flow velocity or flow rate for which acoustic focusing is of adequate quality. For 5 µm beads used as a standard the maximum flow rate for adequate focusing was 10 µl/min corresponding to maximum flow velocity 33 mm/min (0.553 mm/s) and this value was set for all the subsequent experiments and calculations.

2.3 Optical Layout
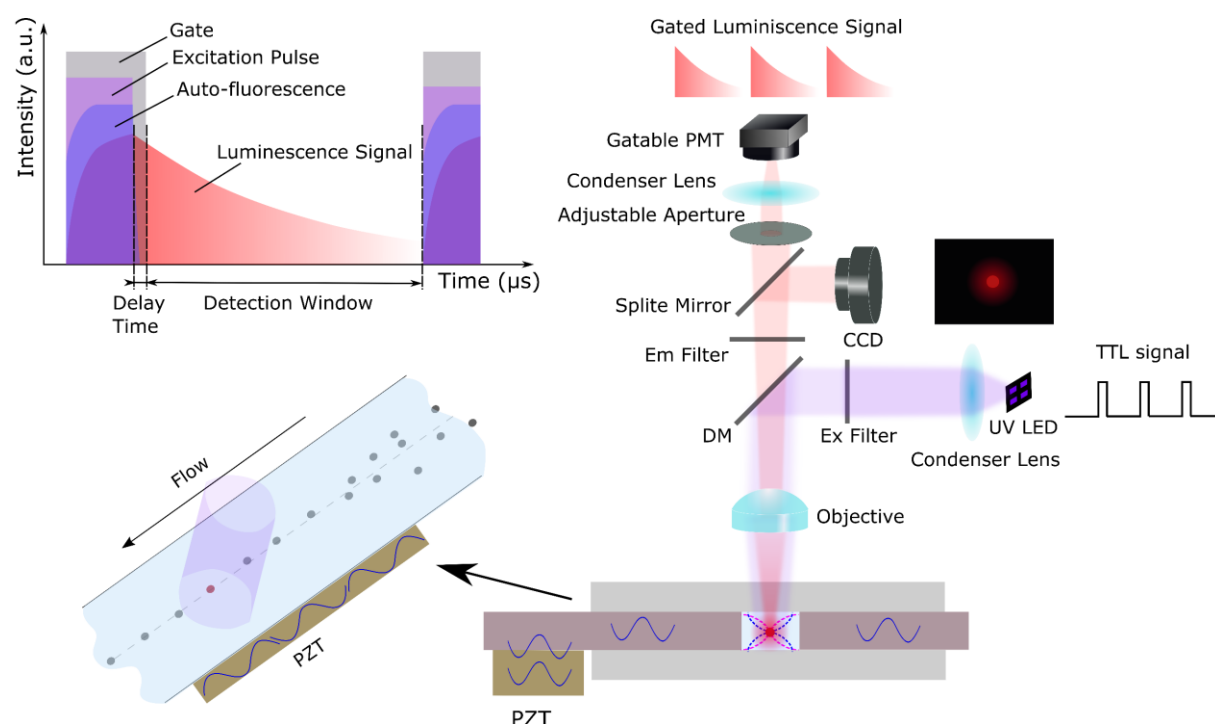
Figure 2-8 Optical configuration.

The microfluidic flow channel is mounted on the X-Y stage of a commercial epifluorescence microscope (BX 51, Olympus). The lanthanide probes (most frequently europium complex Eu-BHHCT[85,133,160]) which have been used throughout current project,

have absorption maxima in the UV region (335 nm) and emit strong long-lived (>100 µs) luminescence around 615 nm. The excitation source is an ultraviolet light-emitting diode (UV LED, M365LP1-C1, Thorlabs, total beam power 505 mW at 1700 mA as maximum current) with peak wavelength at 365 nm and bandwidth 9 nm. The excitation light is filtered by a UV-band-pass filter (U-360, Edmund Optics) and then reflected by a 45° mounted low-pass dichroic mirror (DM, T400LP, Chroma) before passing through a long working distance objective (LUCPLFLN 40X, Olympus, $f = 45$ mm, $NA = 0.6$). The particles/cells doped with Eu^{3+} complexes passing through the flow channel are excited by the wide-field UV beam, focal aperture size typically of diameter 0.5 mm at the flow channel. The 615nm Eu^{3+} emission passing through the dichroic mirror (DM) is filtered by a band-pass filter (ET615/40m, Chroma) and then delivered to either a time-gated photomultiplier tube (PMT, H10304-20-NF, Hamamatsu, cathode radiant responsivity R=78 mA/W at λ=612 nm, electron amplification gain GE=10^6) or a digital camera (Lu165M, Lumenera) optionally with a moveable mirror placed at 45°. For maximum emission collection efficiency, the PMT was mounted at the focal distance of a convex lens ($f = 50$ mm, Thorlabs). An aperture (SM1D12D, Thorlabs, SM1 ring-actuated iris diaphragm, Ø0.8 - Ø12 mm) was mounted in PMT side for adjustment of detection spot size. Mounting the PMT and CCD camera on the standard observation ports of the BX51 microscope required custom-fabrication of adaptors (Fig. 2-10).

2.3.1 Optics Selection

As shown in Fig. 2-9, UV-visible absorption analysis (NanoDrop 2000 UV spectrometer, Thermo Scientific) of the Eu chelate BHHBCB indicated a maximum UV absorbance at around 335 nm and peak luminescence intensity at 615 nm. The transmission (T) of excitation filter, dichroic mirror and emission filter are also plotted (dash line) in Fig. 2-9.
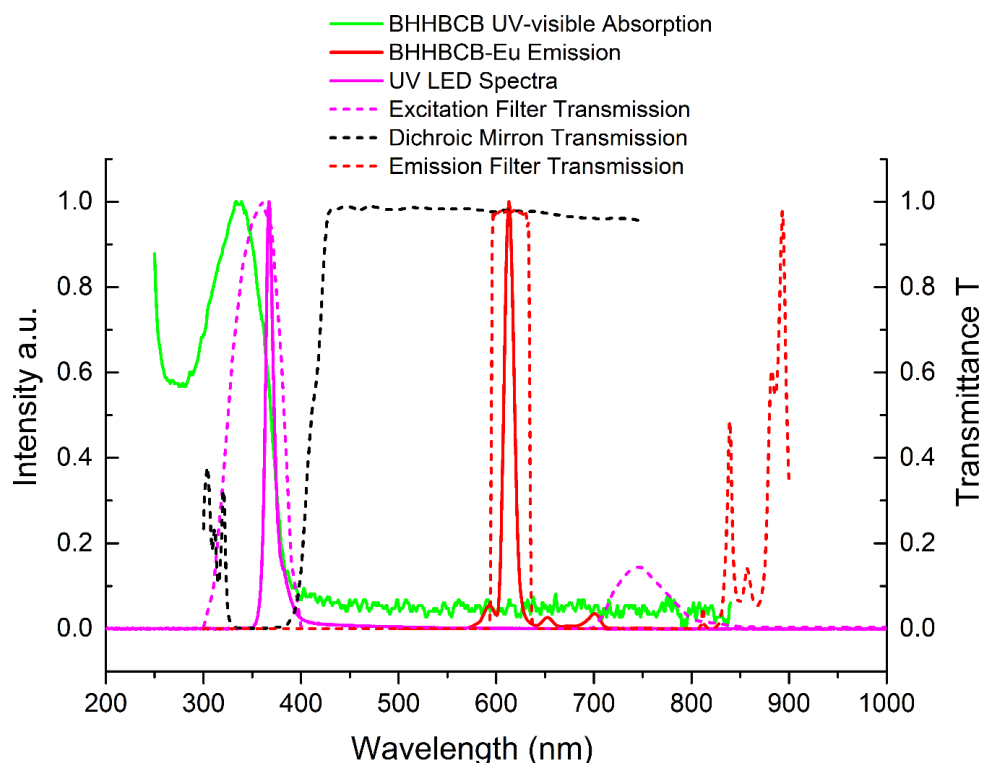
Figure 2-9 Spectrum of excitation (green solid) and emission (red solid) of Eu chelate, spectra of UV LED (purple solid), and transmittance (T) of excitation filter (purple dash), emission filter (red dash) and dichroic mirror (black dash) that we selected for this platform.

A Thorlabs M365LP1C1 collimated UV LED was chosen as the light source, comprising the M365LP1 mounted UV-LED and an aspheric collimation optic (ACL5040U-A, Thorlabs, Ø50 mm, f=40 mm, NA=0.60, AR-coated: 350-700 nm). The collimated LED was mounted in an Olympus BX/IX port-compatible housing on the BX 51 platform. The single short-focal length aspheric lens can collimate the highly divergent emission of the laser diode, which is mounted at the focal point of the aspheric lens, without introducing spherical aberration or losing significant beam power. The LED is equipped with a heat sink to promote power stability and long operating life.

A long working-distance objective was needed on this platform as the microfluidic chip structure, the upper glass slide on the 0.52 mm × 0.58 mm microchannel is 1mm thick. Accordingly, an adjustable 40X UV objective from Olympus (LUCPLFLN 40X) with WD of 2.70 - 4.00 mm, was selected for this purpose.

2.3.2 Wide Field Illumination and Detection

As discussed in more detail below and in the following chapter, the longer the transit time of a target particle across the excitation-detection window, the more accurate are luminescence lifetime determinations. Since it is desirable to have the highest possible volume flow rates to minimise sample processing times, achieving the largest possible transit time translates to the largest possible excitation and detection window, thus wide field illumination is chosen. Note however that a large illumination and detection aperture also increases the likelihood of more than one target particle entering the field of view during a lifetime measurement, which adds further complication to lifetime determination for individual particles. To address this, an adjustable aperture was introduced to change the detection aperture size, making transit time independent to constant illumination aperture. The detection aperture size and corresponding transit time will be discussed in more detail in Chapter 3.

In practice the size of the excitation aperture is limited by the width of microfluidic channel since where the aperture impinges on the edges of the microfluidic channel a high level background optical signal is observed. This is due to UV-excited broadband emission from the silicon. A fraction of this broadband passes through the 615 nm emission filter and appears as a strong background to the 615 nm signal from the Eu^{3+} emission from labelled microbeads or cells of interest. This effect was measured by placing one of the silicon wafer edges directly under the objective and measuring the emission signal under CW UV excitation, and comparing the optical signal to the situation where the excitation aperture is confined within the width of the channel (i.e., the walls of the channel are not illuminated nor are they visible). These experiments were conducted with the microchannel fulfilled with pure MiliQ water. Accordingly, the UV illumination aperture was confined to a 0.5 mm diameter spot centred on the 0.58 mm wide flow channel.

For the majority of experiments, the illumination/detection aperture was imaged via collection optics to the photocathode of PMT, which generated photocurrent for subsequent analysis as described in the following section. Visualisation of target particles/cells transiting the illumination aperture was provided by a CCD camera (Lu165M, Lumenera). As shown in Fig. 2-8, the emission light was split into two orthogonal directions after passing through the emission filter, with the PMT on the vertical axis and CCD on the horizontal axis (i.e.,

the camera port). The length of both of light paths could be adjusted to image the emission plane onto both sensors.
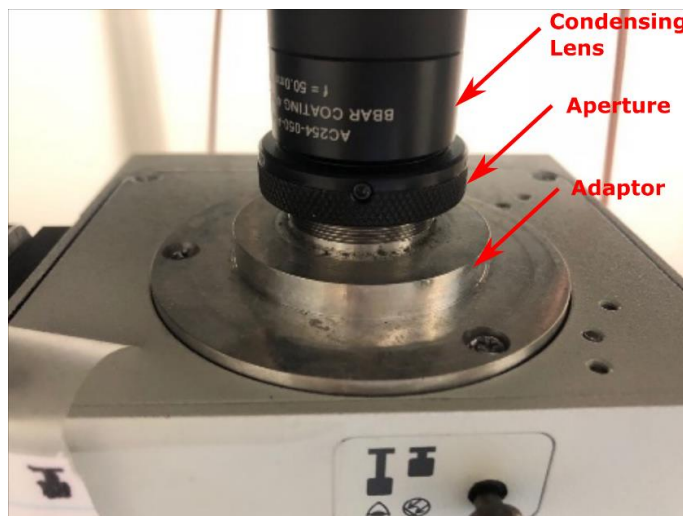
Figure 2-10 SolidWorks design of adaptor, an adjustable aperture and a condensing lens for projecting emission to PMT sensor plane.

In the case of the PMT, the adjustable aperture with a 50 mm condensing lens was mounted on a custom-designed adaptor (Fig. 2-10) on the vertical port to image the illumination-independent detection window onto the PMT. The transit time of luminescent targets passing through the detection aperture that projected on PMT sensor is actuated according to diaphragm diameter, which will be discussed and calculated in next chapter.

2.3.3 Pulsed Excitation and Gated Detection

The key concept of time-resolved detection in a flow system involves periodic pulsed excitation and gated detection of luminescence as the target particles/cells transit the active (illumination/detection) window, analysis of the recorded luminescent signal enabling the luminescence lifetime of the targets to be determined. The UV LED is pulsed periodically, triggered by the TTL signal from custom-programmed on-line Labview software. The PMT with gate function, allows high-speed gate operation with 100 ns minimum gate width and maximum 100 kHz repetition rate, driven by a TTL signal from Labview program.
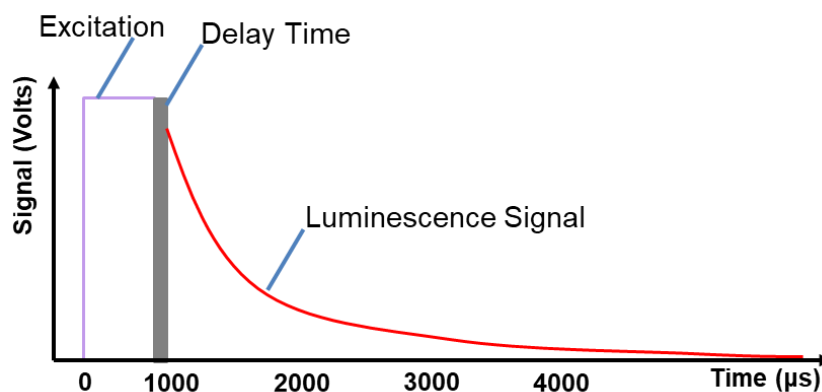
Figure 2-11 Sequence of TTL of UV, delay window and detection in a TGL cycle.

The PMT is gated off for the duration of each UV excitation pulse plus a short delay time (~5 µs) after the UV pulse is terminated, so as to avoid detection of short-term autoflourescence which otherwise appears as background signal (Fig. 2-11). The luminescence decay time of the target can be determined by analysis of the signal generated by high-frequency sampling of the intensity of the emission when the PMT operates in ungated (on) mode. The trigger signal for the UV excitation pulses and PMT gate are synchronised by the electronic control system, which also initiates data acquisition and analysis as described below.

2.4 Electronic Control System and Real-Time Analysis Software
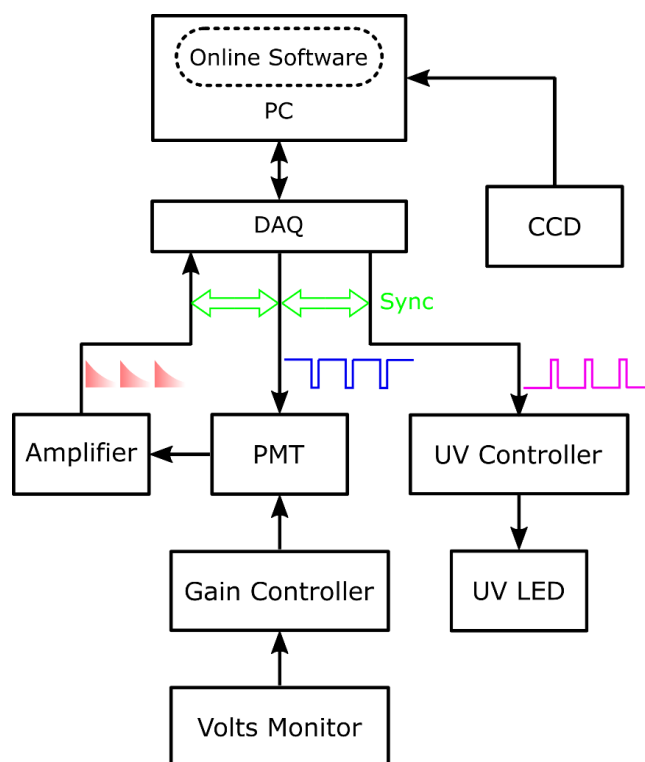
Figure 2-12 The electronic control scheme of the TRMFC.

Electronic control and data acquisition and analysis are coordinated by custom-programmed Labview software on PC (Fig. 2-12). This system communicated with the active devices, i.e., PMT and UV LED, through a PC-based multifunction data acquisition card (DAQ, PXIe-6358, National Instruments). As shown in Fig. 2-12, two AO ports of the DAQ were dedicated to delivering the pulsed driving signal to the PMT and UV-LED controller, while an AI port was dedicated to input of the luminescence signal data from the PMT. The AI/O signals were synchronised to the AI sample clock. A monochrome CCD camera (Lu165M, Lumenera) was connected to the PC directly through a USB port to transmit images and videos. Note that a 100/0 split mirror was mounted in the double port tube of the BX51 microscope, so that either the PMT or CCD camera can be selected to access the luminescence signal.

2.4.1 Electronic Devices

The UV LED driver received a control signal via the SMA connector from the PC and DAQ, using the external modulation input port. This was controlled by a TTL signal initiated by the Labview software, allowing users to set TTL on/off timing (800 µs /1200 µs) and

cycle frequency (500 Hz). The LED driving current and current limit were set to determine the beam power of the LED.
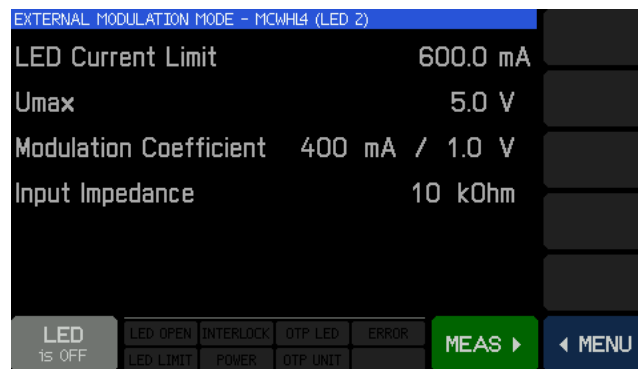
Figure 2-13 Front panel of LED driver working at external control mode.

The PMT received the pulsed gating signal (1195 µs gating on, with 805 µs delay from start of the LED pulse) via a SMA connector to PC and DAQ, and the output luminescence current signal accessed through a second SMA connector. PMT gain was adjustable with a custom-made control box, which was assembled with a potentiometer for resistance programming to vary the gain, as illustrated in Fig. 2-14. The PMT control voltage was normally set at 0.9 V corresponding to 10^6 gain.
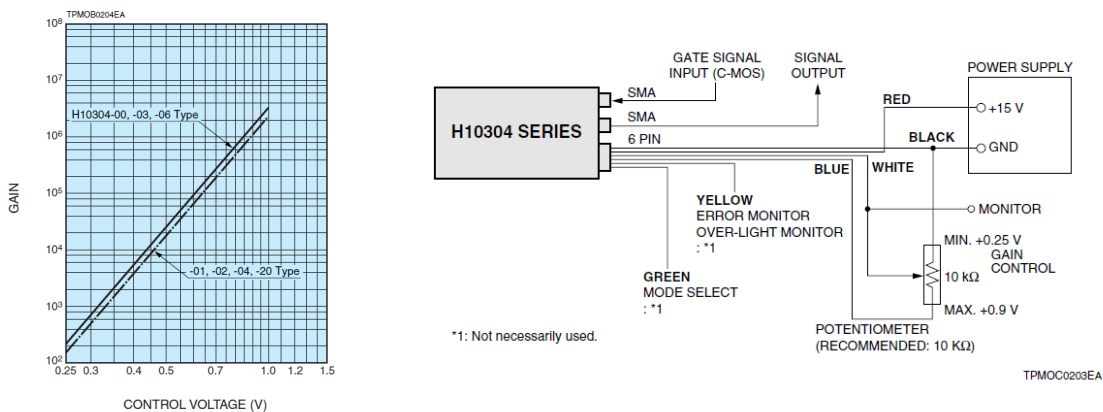
Figure 2-14 PMT gain over control voltage and the design scheme of gain control box.

The output current signal from the PMT was amplified into a voltage signal via a low noise amplifier (DLPCA-200, FEMTO, Germany; transimpedance switchable from 10^3 to 10^{11} V/A, Fig. 2-15). The gain used in the experiment was determined by the luminescence magnitude, and was normally 10^5 V/A, alternately 10^4 V/A if saturation was reached for strong signals.
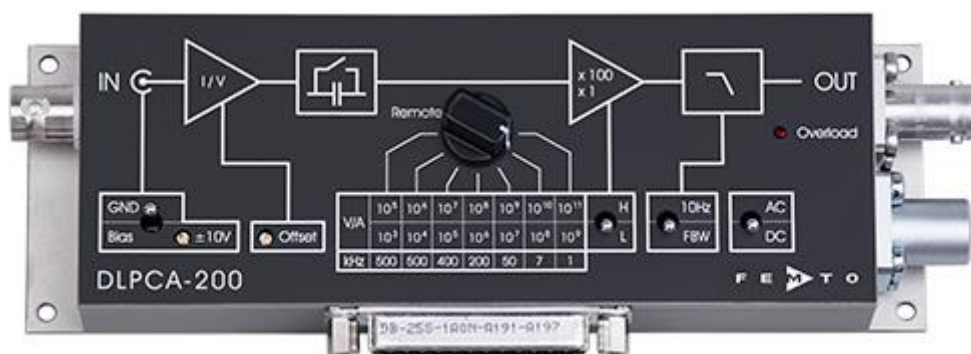
Figure 2-15 DLPCA-200, FEMTO, Germany, transimpedance switchable from 10^3 to 10^{11} V/A

All the images and videos of bright field or UV excitation in the microfluidic channel were captured by a Lumenera (Lu165M) CCD camera (Fig. 2-16). Luminescence emission transmitting up the vertical axis of the BX51 microscope from the objective was fully reflected by the 45° turning mirror to the monochrome 9.0mm×6.7mm CCD sensor of the camera, which has high responsivity across the visible range from 450 nm to 680 nm. The 1392×1040 resolution images at 15 fps or binned 640×480 images at 30 fps were live streamed to PC through a high speed USB 2.0 port.
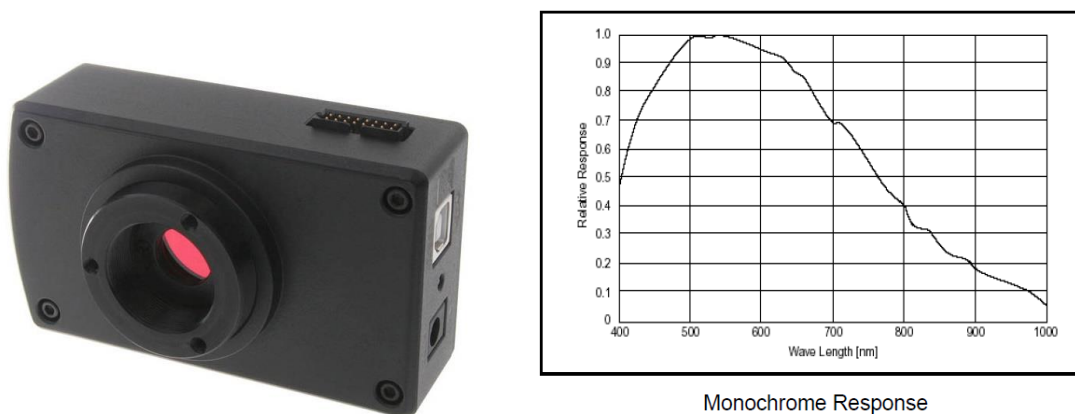
Figure 2-16 CCD camera, Lu165M, Lumenera and monochrome response over 400 nm-1000 nm wavelength.

2.4.2 Real-Time Control and Processing Software

The online program outputs the pulsed driving signals of UV LED and PMT through DAQ and samples the amplified luminescence signal from PMT at the rate of 200 kHz, i.e., one reading every 5 µs, via analogue input of the DAQ. And the AI/O signals were synchronised to the AI sample clock, which was programmed by the real-time software. In addition to

controlling of the electronic devices, the program determined the lifetime, counted events and differentiated populations as described in the next chapter. The program was also capable of resolving overlapping events in the situation of well-controlled sample concentration, as discussed in Chapter 3. All the raw luminescence data was saved on the PC disk for offline analysis as required.
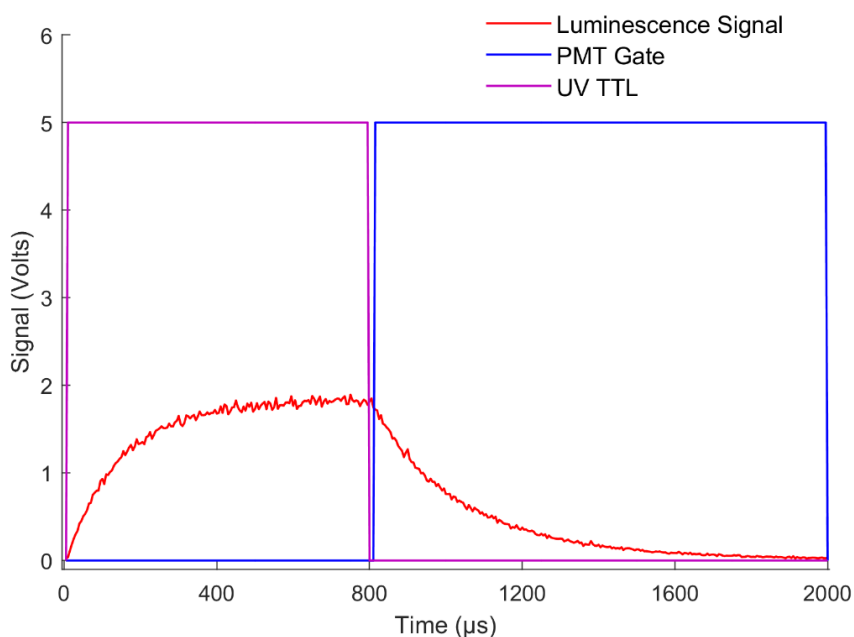
Figure 2-17 Timing sequence of PMT, UV, and luminescence decay

Fig. 2-17 illustrates the timing sequences of control signals including PMT gating pulses (green), UV-LED control TTL (blue) and amplified luminescent signal from input port (orange). There are several factors which determine the sequence timings to achieve optimum system performance:

i. The duration of the UV excitation pulse is chosen to reach maximum luminescence intensity from target particles or cells at the end of the excitation pulse (see Fig 2.17).

ii. Longer detection times result in more precise lifetime calculation, however, this also results in decreased sample throughput. Ideally the detection duration is matched to a minimum 3 decay lifetimes of the luminescent targets, however in the case of very long lifetimes this may be limited to only 1 lifetime. Because the lifetimes of the luminescent probes used here generally ranged from 100 µs to 1 ms, the detection duration was typically set at 1 ms.

iii. Biological autofluorescence lifetimes are typically in the tens of nanosecond, normally <1 µs, thus the 5 µs delay before PMT detection switches on is a convenient choice.

Based on the above factors an LED excitation pulse of 800 µs, with a 5 µs delay when the PMT was gated off was used. At the end of the delay period the PMT gate was removed and the luminescence signal detected for 1195 µs until the end of the sequence is terminated by applying the gate signal to the PMT. This sequence is repeated at 500 Hz so that for a typical the transit time of a target across the illumination/detection aperture some excitation-detection sequences are recorded (shown in detail in Chapter 3). The detection signal was saved in PC disk and simultaneously analysed by the online software to determine the lifetimes of the targets and accordingly differentiate them into specific lifetime populations. The method of lifetime calculation and discrimination will be discussed detailed in Chapter 3.

Chapter 3:   Methodology

3.1 Introduction

In the previous Chapter 2, the instrumental design, components selections and settings for the custom-built time-resolved microfluidic flow cytometry have been presented. In this chapter the detected luminescence signal data is described in detail, how the data is analysed to extract lifetime measurements in real-time, and how the operating parameters are optimised to ensure accurate lifetime determination and maximum sample throughput. Included is analysis of signal data when multiple luminescent targets are present in the detection window and how this is dealt with. The performance of the time-resolved microfluidic flow cytometry is evaluated using standard 5 µm Eu-doped polymer beads as luminescent targets in aqueous flow in Chapter 4, providing the foundation for preliminary lifetime multiplexing with Eu chelates stained cells, to be presented in Chapter 5.

3.2 Signal Train Analysis

To realize the time-resolved detection in flow cytometry, accurate lifetime decoding of luminescent targets is the first key step to be achieved. The following sections describe the detected signal characteristics and how the signal data is analysed to provide accurate luminescence-lifetime measurements in continuous flow.

3.2.1 Signal Inspection from Populations Towards Events

As described in the Chapter 2.4, the current output from the gated PMT was converted to a voltage signal and amplified by 10^5 (or 10^4 if saturated) before transmission to the PC via the DAQ card. Fig. 3-1 shows the digitised signal recorded at the PC for a MiliQ water solution of well-suspended Eu polymer beads (~10000 beads/ml) detected in flow on the platform.
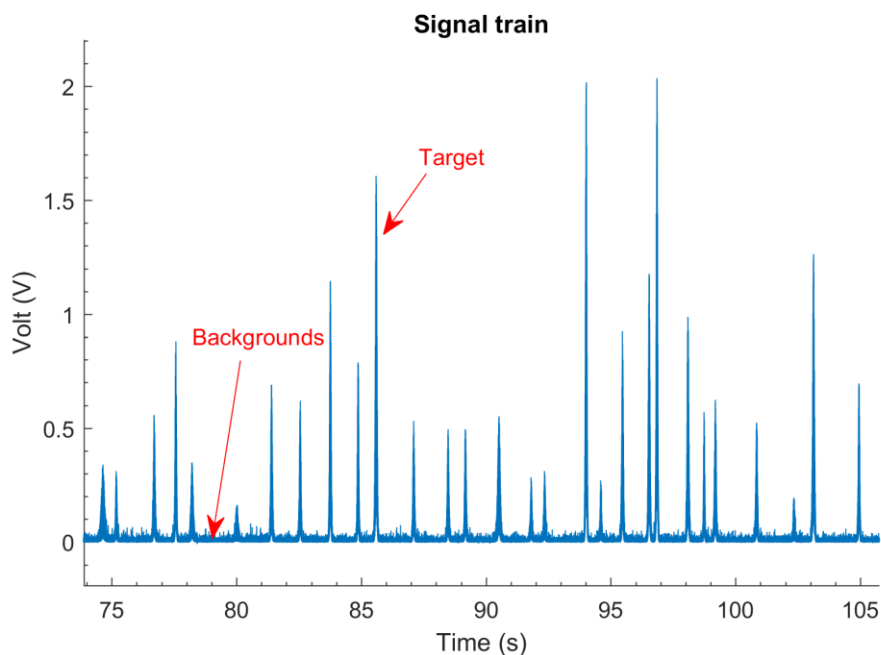
Figure 3-1 Original signal train of luminescence that DAQ transmit to PC.

In the figure the sharp peaks correspond to the presence of Eu labelled targets in the detection aperture and the low noisy background corresponds to detection cycles where no target is present in the detection aperture. Although any signal resulting from autofluorescence is eliminated by time-delay detection after the excitation pulses are terminated, system noise arising from stray light from the environment or from the detector itself cannot be avoided. Another major source of background is expected to be from the long-lived UV-induced visible luminescence from metal impurities in the glass cover slip of the fluidic channel, though this should be a constant in the current experiments.

For the intensity signal sampling rate 200 kHz used here, the interval between successive data samples is 5 µs and there are 2×10^5 data points per second on the signal train. We consider the structure of the signal presenting in a single peak corresponding to detection of a target event (specifically the peak indicted by the arrow in Fig. 3-1).
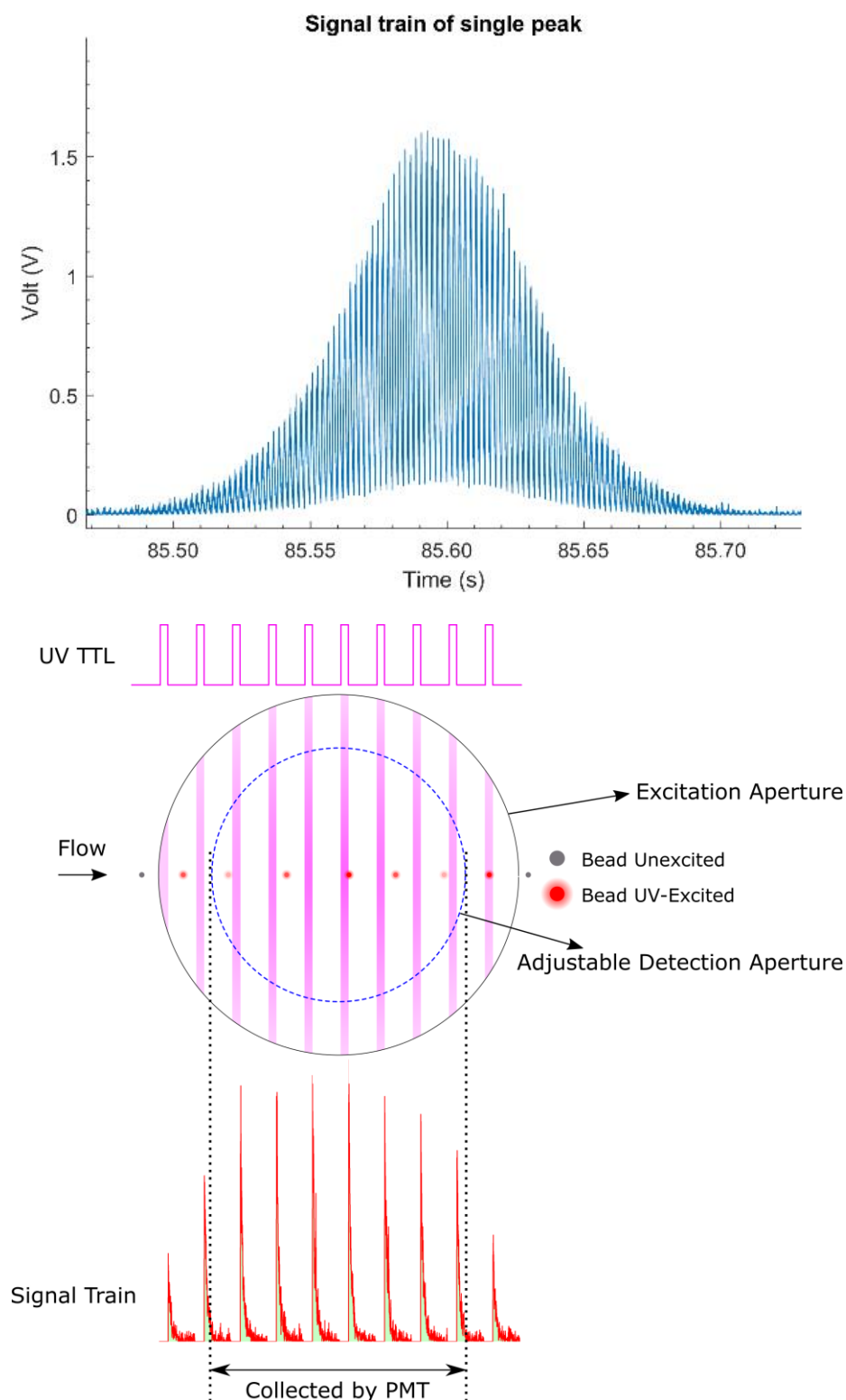
Figure 3-2 Signal train of one of peaks (upper panel) when a target intersecting the detection aperture is detected. The lower panel demonstrates how the peaks formed when a single bead flowing along the excitation aperture and detection aperture in the fluidic channel. The red dots are from the same bead at different positions downstream of the flow.

As shown in upper panel of Fig. 3-2, one single peak consists of a series of TGL cycles, within a Gaussian-shaped envelope spanning approximately 200 milliseconds. Fig. 3-2 lower panel demonstrates how the cycles were formed under pulsed UV excitation when a luminescent target transits the detection aperture. For each excitation-delay-detection cycle, a luminescence decay signal from the PMT is recorded, resulting in a train of decay curves at the cycle interval as the target passes by.
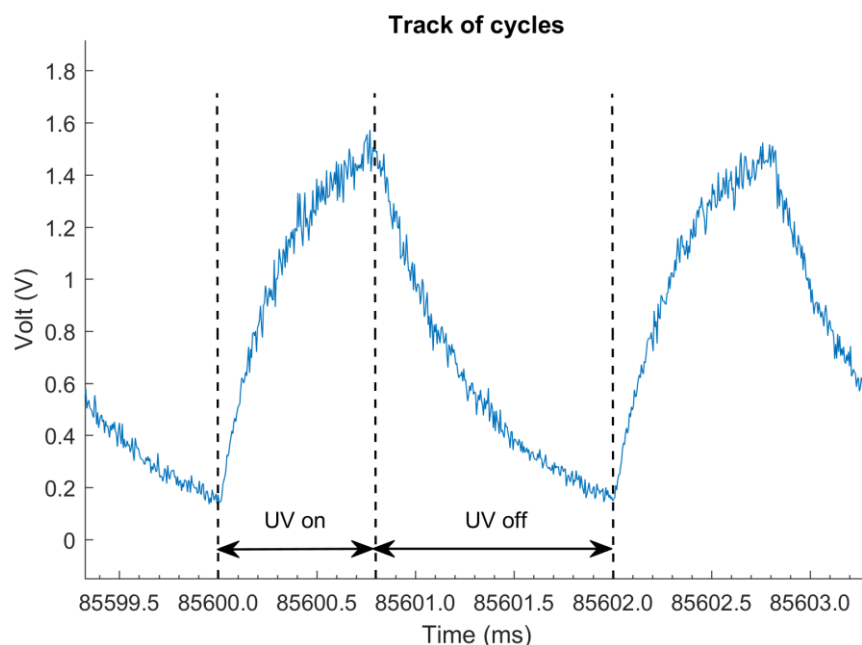
Figure 3-3 Signal data digitalized by PC in TGL detection cycles; here the PMT was ungated to examine the signal shape in whole TGL cycle.

To show the signal data for an individual cycle, we further zoom in at around 85.6s in Fig 3-2 on the millisecond scale, as illustrated in Fig. 3-3. Note that this set of data was collected when the PMT was ungated so as to examine the signal shape corresponding to repetitively pulsed UV excitation. During the excitation pulse (800 µs), the intensity signal arising from both autofluorescence and target luminescence increases; when the excitation ceases, the signal decays for the remaining period of the excitation-detection cycle (1200 µs). In the usual experiments, the PMT is gated off for the full duration of the excitation pulse plus an additional short delay (5 µs) as presented in Chapter 2.4. The luminescence lifetime of the target is extracted from the averaged decay curves in the TGL cycles when UV is off, as illustrated in Fig. 3-3.

3.2.2 Signal Pre-Processing and Featured Parameters
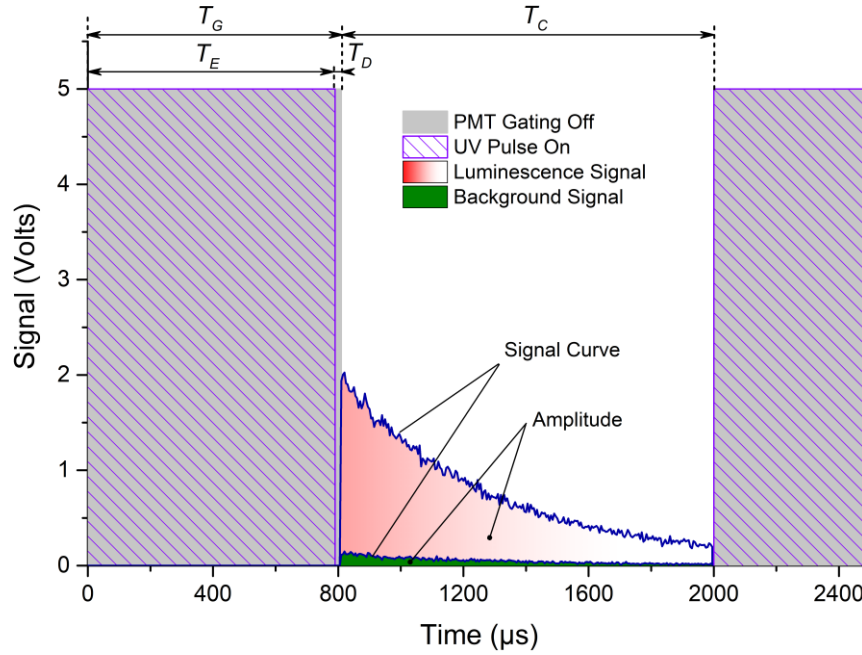
Figure 3-4 Experiment data curves of target luminescence and system background noise, the area under the curve is defined as amplitude. The PMT is gated on for detection duration $T_C = 1195$ µs, with delay $T_D = 5$ µs after the excitation pulse of duration $T_E = 800$ µs. Data was collected at a sampling rate of $f_{sam} = 200$ kHz.

For subsequent analysis, the raw signal train is pre-processed to remove background and identify signal arising from targets. As shown in Fig. 3-4, where experimental data is plotted in blue curves, it is evident that the large signal (red area) corresponds to target events and the small signal (green area) to background when there is no target.

To separate targe signals from the low intensity background, a threshold is applied. Although the simplest approach to setting a threshold is to use a signal voltage value, this is not reliable in the limits of low signal due to high signal noise. In order to overcome this problem, the threshold is set using a time integrated voltage calculated for each TGL detection window so as to average out random signal noise. Specifically, for each TGL cycle the signal voltage is integrated over the detection time T_C as:

$$A_T = \int_{T_G}^{T_G + T_C} V \, dt \tag{3-1}$$

where V is the voltage of signal and dt is in units of μs. The threshold value A_T for discrimination of target signal from background is then set empirically as described below.

The value of the threshold A_T was determined from signal observed for pure MiliQ water, PBS and a commercial AutoMacs buffer as control samples (containing no target particles) in a dark room environment. For threshold values, the number of artefact events was counted and plotted as in Fig. 3-5. As can be seen, the number of false-positive events arising from noise decrease dramatically logarithm fluids on a logarithmic scale as the threshold value A_T was increased. The different sample fluids had little effect on the observed threshold for artefact events. To achieve 100% counting accuracy for target events the threshold value A_T is set at 4.0 V·μs for all subsequent data analysis for this system.
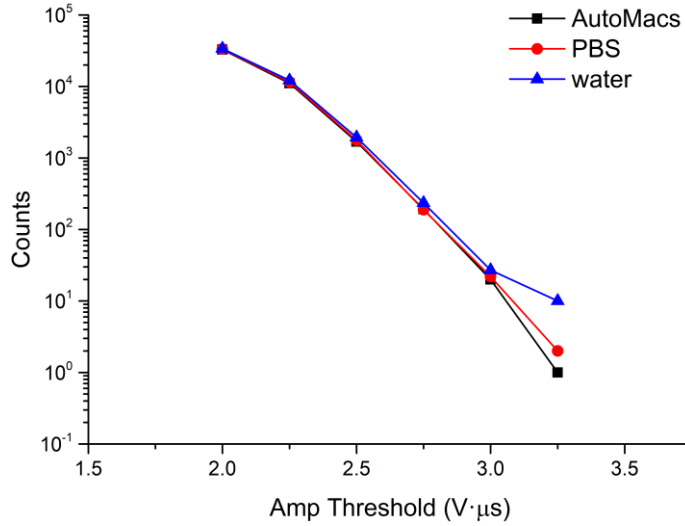
Figure 3-5 False-positive event counts for different A_T threshold setting.

After the removal of the background data in the signal train by applying an A_T threshold of 4.0 V·μs, the signal arising from luminescent targets are picked out as separate trains (Fig. 3-6). The duration of a single pulse train corresponds to the transit time T_W of a target crossing the field of view (FOV) and there are N TGL cycles containing in each pulse train. N and T_W has a direct proportional relationship as below,

$$T_W = N \cdot T_L \tag{3-2}$$

where T_L is the period of the TGL cycle, equal to the sum of T_G and T_C.

As the target transit time T_W is also proportional to FOV diameter L directly and inversely proportional to flow velocity v, as shown in Equation 3-3:

$$T_W = \frac{L}{v}$$ (3-3)

It follows that a larger FOV increases the transit time and the number of TGL cycles, whereas increasing flow velocity decreases T_W and N.

For flow velocity 0.553 mm/s corresponding to flow rate 0.01 ml/min, and FOV 100 µm, the transit time T_W is calculated as 180.83 ms. Applying Equation 3-2, the TGL cycle number N within a single pulse train is expected to be ~90.
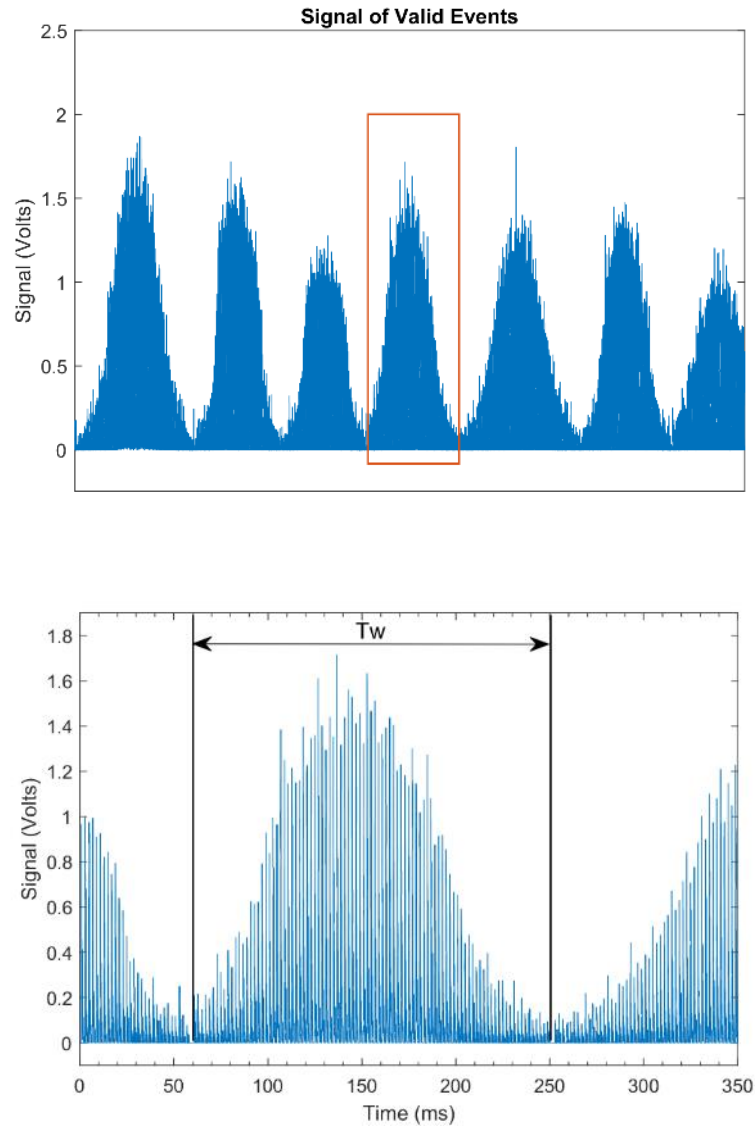
Figure 3-6 Separate signal trains after the removal of the background and the time width of the single train T_w represents the target transit time.

When the data for a single target transit event has been extracted, determining the luminescence lifetime for single event is comparatively straight forward, discussed in the following section.

3.2.3 Lifetime Determination of Single Event

The luminescence lifetime for a target can be determined from the data in a single event pulse train using two different approaches. First method (A) calculates the lifetimes for each TGL cycle individually before averaging them to get the final lifetime for the event. The second method (B) requires summing all the TGL decay curves in the pulse train first and then calculating the lifetime for the summed curve. For both approaches the lifetime is determined by fitting the intensity data to a mono-exponential curve using the non-linear least squares method in Matlab to obtain the initial intensity I_0 and the lifetime τ according to the following equation,

$$I(t) = I_0 e^{-\frac{t}{\tau}} + c \tag{3-4}$$

where c is the constant background noise. The coefficients I_0 and τ are extracted with 95% confidence.

The lifetimes obtained by the two methods differ because the lifetime is generally not linear with respect to the magnitude of the signal, though the disparity we observed experimentally was comparatively small. Specifically, the lifetime values varied less than 15 µs, typically less than 10 µs in lifetimes ~250 µs, as illustrated in Fig. 3-7, comparing lifetime determinations by the two methods, the CV for method A is 2.3 %, and for method B 2.2 %. The data set used for this comparison was collected with a water solution of Eu polymer beads with uniform lifetimes around 235 µs.
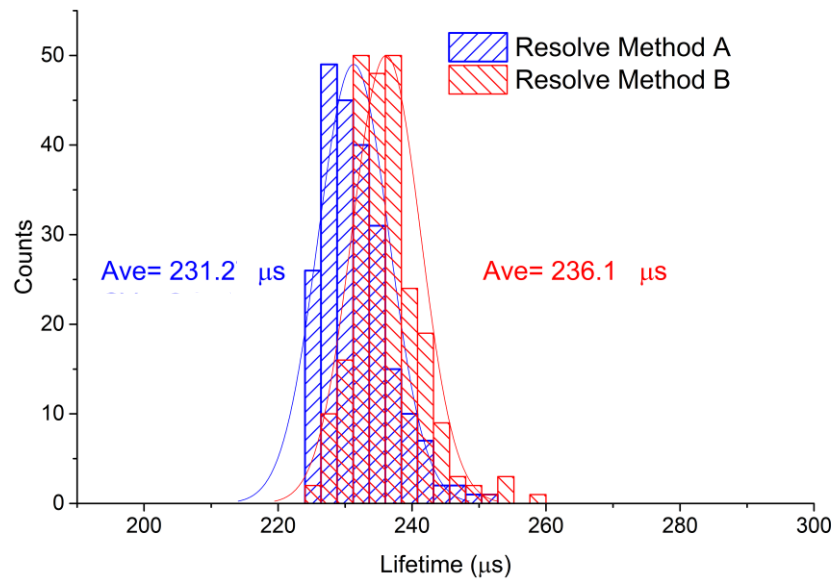
Figure 3-7 Comparison of two methods of lifetime resolving.

It is apparent from the above test data, that method B results in more accurate lifetime determination with lower CV, thus method B was adopted method for all subsequent experiments and lifetime determination.

3.3 Overlapping Events in Wide-Field Detection

After the removal of background by applying the A_T threshold the signal pulse trains for individual target events are arranged in a serial array, separated by a zero raw data set for later analysis (Fig. 3-6). but in practice not all the signal pulse trains have a simple Gaussian envelope as shown in Fig. 3-6, that the signal arises from transit of a single target across the detection aperture. Fig. 3-8 below shows a variety of signal pulse trains with different profiles that are observed when more than one target is present in the detection aperture at a time.
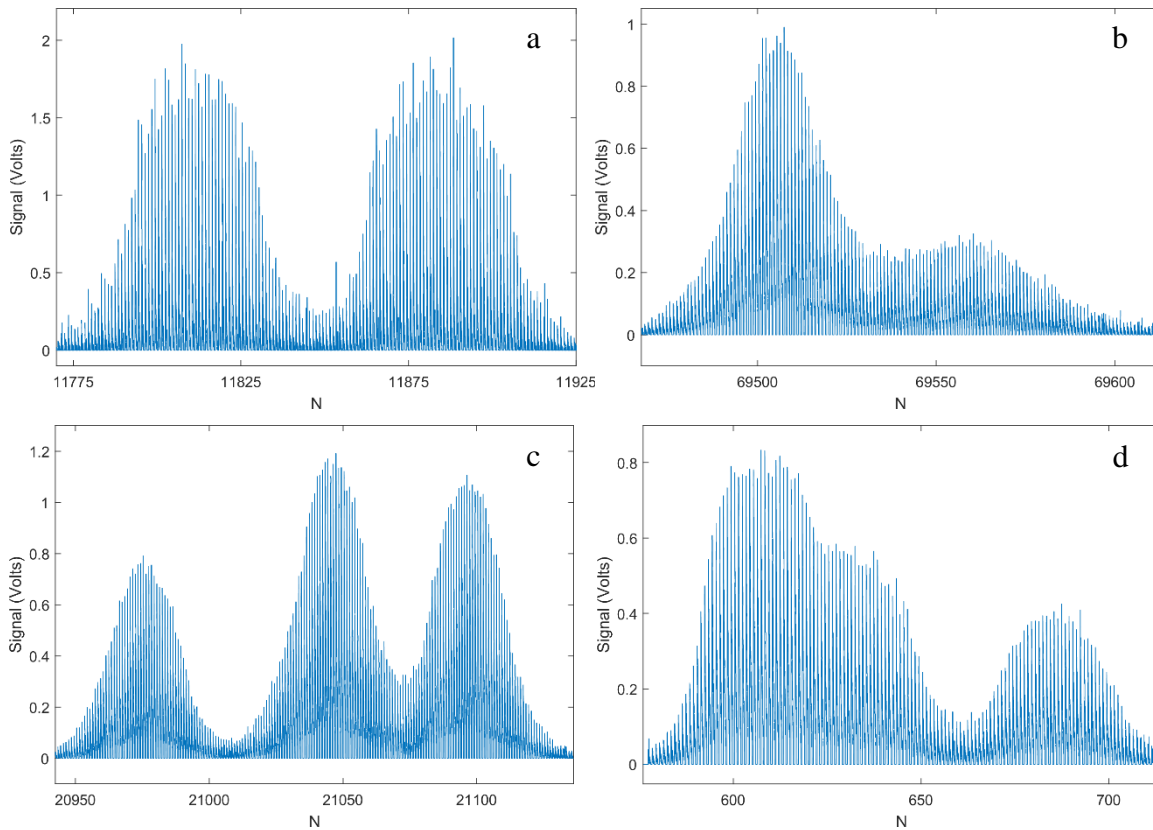
Figure 3-8 Signal segments with different profile in the overlap situations.

In the case of the two upper signal profiles in Fig 3-8 it is evident that two targets have entered the detection window in a very close succession. As a result, there is a period of time when the two targets are interrogated simultaneously. It is obvious that two targets represented in the Fig. 3-8b are closer to each other than those in Fig. 3-8a, and in this case the intensity observed for the second target is noticeably smaller than for the first target. Similarly, Figs. 3-8c and 3-8d show a signal train where three target events overlap in the detection aperture.

Clearly instances of target overlap raise difficulties in determining the luminescence lifetime for individual targets. The probability of detecting overlapping events is a function of the size of the excitation and detection apertures illustrated in Fig. 3-9.
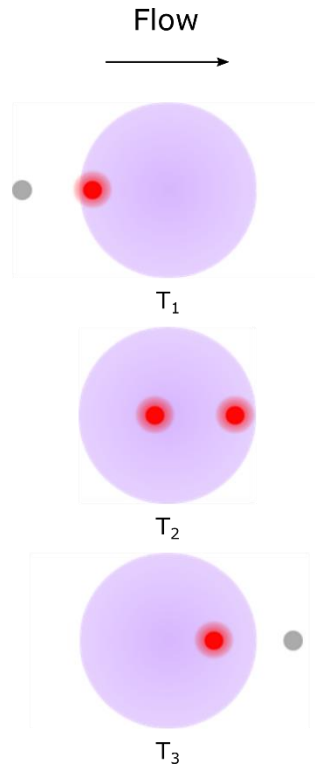
Figure 3-9 Overlap of target events in a wide-field detection platform.

However, as explained in Chapter 2.3.2, wide field illumination is necessary for this platform because multiple TGL cycles are needed for accurate determination of lifetime. Equally it is important that no target event is missed so that a 100% event detection rate can be achieved (for example, in rare-event detection, such as early-stage cancer diagnosis, it is critical not to miss any suspect targets).

Accordingly, the decoding algorithm must be adapted to handle multiple target events, in particular, to determine whether a second, or even a third etc. event in a detection pulse train is of the same or different type (i.e. characterised by the luminescence lifetime). This task becomes increasingly complex as the number of events being detected in the same pulse train rises.

To limit the complexity and provide robust performance for practical applications, here we choose to control the sample throughput, so that the probability for three or more events occurring in the field of view is very low whilst the lifetime decoding algorithm is adapted to address the case of one or two events.

3.3.1 Overlap Probability Modelling

Assuming the sample concentration is constant and the events are well dispersed, the counting process of individual events entering the detection window is a homogeneous Poisson process, which can be denoted as $\{N(t), t \geq 0\}$. The number of events occurring in a given period of time, in particular the transit time of a target across the detection window T_W, follows a Poisson distribution. that is, the probability of the random variable $N(t + T_W)$ $- N(t) = N(T_W)$ being equal to n is given by

$$P(N(T_W) = n) = \frac{(\lambda T_W)^n}{n!} e^{-\lambda T_W} \tag{3-5}$$

where λ is the average number of events per interval for the Poisson process, which is related to the concentration of the sample C and the volumetric flow rate Q by $\lambda = CQ$, i.e. representing the throughput.

T_W is related to length of detection window L and flow velocity v, given by

$$T_W = \frac{L}{v} = L \Big/ \frac{Q}{A} = \frac{LA}{Q} \tag{3-6}$$

and

$$\lambda T_W = CQ * T_W = CQ * \frac{LA}{Q} = LCA \tag{3-7}$$

where A is the cross-sectional area of the microchannel, $0.52\ \text{mm} \times 0.58\ \text{mm}$ on this platform.

It follows that the probability of the random variable $N(t + T_W) - N(t) = N(T_W)$ being equal to n is given by

$$P(N(T_W) = n) = \frac{(LCA)^n}{n!} e^{-(LCA)} \tag{3-8}$$

Increasing the flow rate Q increases the system throughput λ, but does not affect the overlap probability. As noted in Chapter 2.2.4, the maximum flow rate Q is limited by the degree of acoustic focusing and is set to 0.01 ml/min experimentally. However, the size of detection window L and sample concentration C have direct influence on the overlap probability. Fig. 3-10 illustrates how the overlap probability ($P(N(T_W) \geq 2)$) is affected by target concentration and detection window size.
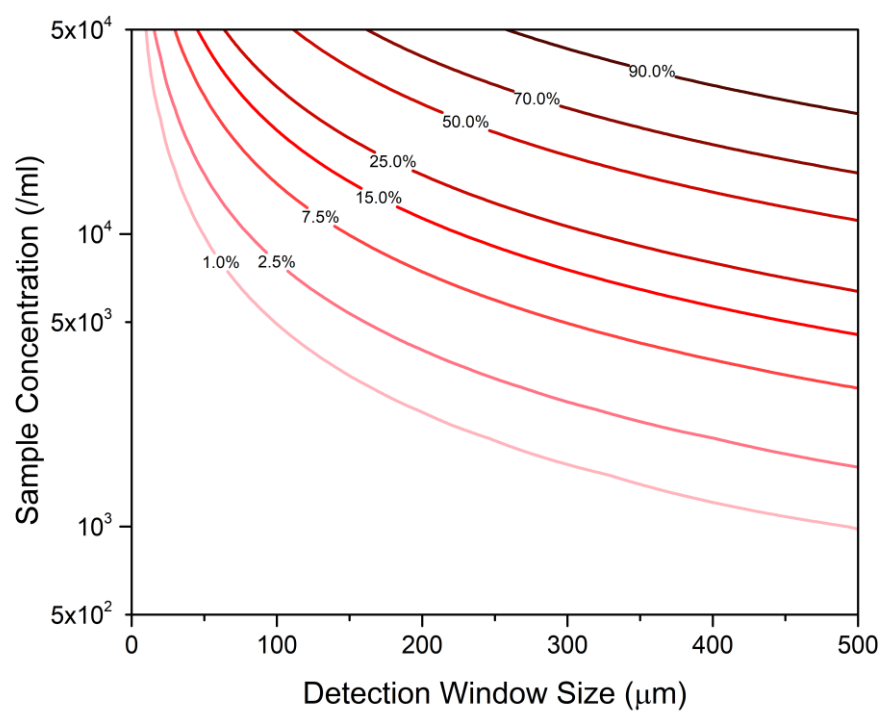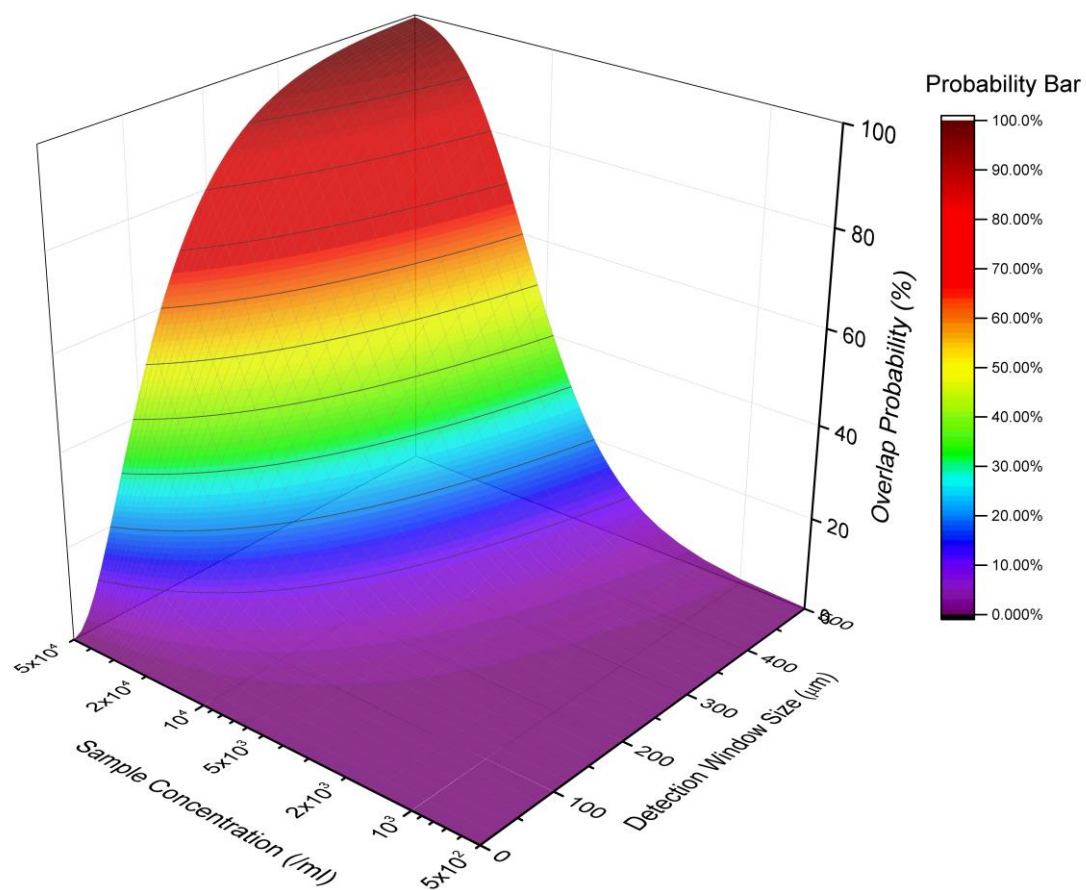
Figure 3-10 Overlap possibility (when $n \geq 2$) towards detection window and sample concentration.

Clearly high concentration and large detection aperture both increase the possibility of overlap, though the size of the detection aperture has a more rapid effect.

The probabilities of one, two and three or more events appearing in the field of view at the one time and consequently in a single pulse train, depend on the same critical parameters. The probability $P(N(Tw) \geq 3)$ that three or more events overlap in a single pulse train is

$$P(N(T_W) \geq 3) = 1 - P(N(T_W) = 0) - P(N(T_W) = 1) - P(N(T_W) = 2) \qquad \textbf{(3-9)}$$

Substituting Equation 3-5 into 3-9, it follows that,

$$P(N(T_W) \geq 3) = 1 - [1 + \lambda T_W + \frac{1}{2}(\lambda T_W)^2]e^{-\lambda T_W} \qquad \textbf{(3-10)}$$

The probabilities $P(N(T_W) = 1), P(N(T_W) = 2)$ and $P(N(T_W) \geq 3)$ are plotted as a function of the composite variable λT_W in Fig. 3-11. As λT_W increases, the probabilities for one or two coincident events increase over a short range and then decrease rapidly as the probability of three or more coincident events increases dramatically.
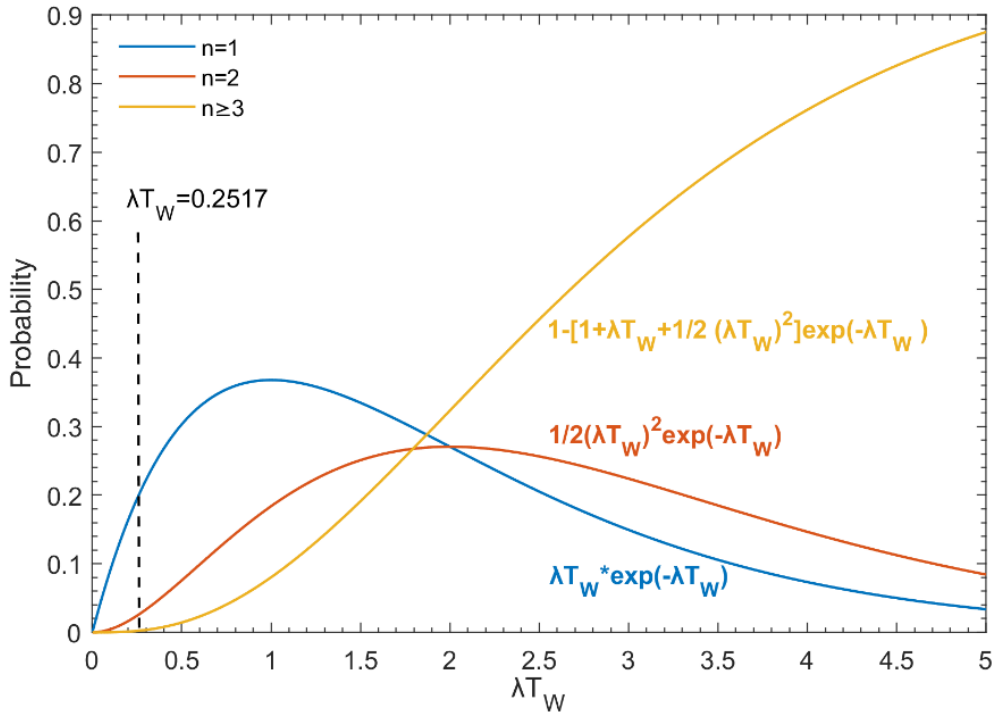
Figure 3-11 Probabilities of one, two and three or more coincident events as a function of λT_W.

3.3.2 Detection Area and Sample Concentration

As illustrated in Fig. 3-10, increasing the target concentration in the sample and the size of the detection aperture increases the probability of overlapping detection events. Thus the settings for detection aperture size and sample concentration are critical for optimizing the performance of the system to achieve the highest possible accuracy in determining the luminescence lifetimes of the targets and the highest sample throughput.

In the situation where three or more target events appear in the field of view at the same time, that is within a single pulse train, it becomes problematic to determine the individual target lifetimes since three or more exponential functions are hard to solve when the initial intensity and decay rate for each function are unpredictable. Thus we set the condition that the probability $P(N(T\text{w}) \geq 3)$ is low, less than 1% of the sum of probabilities $P(N(T\text{w}) = 1)$ + $P(N(T\text{w}) = 2)$. In this case, we need only address the cases where there is only one event recorded in a single pulse train, or a maximum of two overlapping events, and pulse trains in which three or more events are discarded, whilst still achieving 99% detection efficiency. That is, operating conditions are set such that

$$\frac{P(N(T_W)\geq 3)}{P(N(T_W)=1)+P(N(T_W)=2)} = \frac{1-\left[1+\lambda T_W+\frac{1}{2}(\lambda T_W)^2\right]e^{-\lambda T_W}}{\left[\lambda T_W+\frac{1}{2}(\lambda T_W)^2\right]e^{-\lambda T_W}} \leq 1\% \tag{3-11}$$

From which we obtain the limiting value

$$\lambda T_W \leq 0.2517 \tag{3-12}$$

which corresponds to the vertical dash line in Fig. 3-11. Substituting Equation 3-7 into 3-12, we find

$$LC \leq 0.835 \ /mm^2 = 8.35 \times 10^{-7}/\mu m^2 \tag{3-13}$$

where L has units of µm and C events/ml in Equation 3-12. Taking the limiting value for LC as in Equation 3-12 and the equation for system throughput $\lambda = CQ$, we conclude that while higher target concentration increases detection throughput it simultaneously limits the size of detection aperture. These two relationships are illustrated in Fig. 3-12.
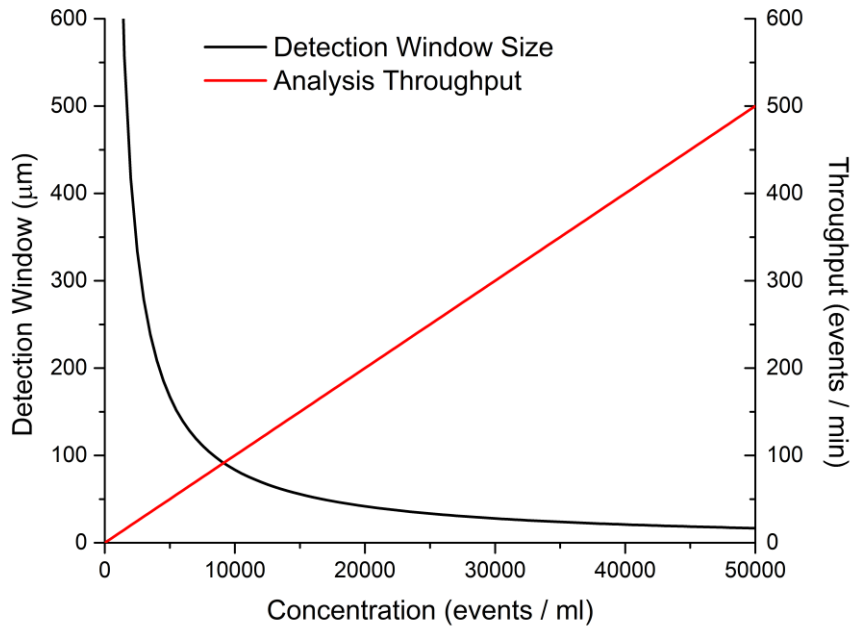
Figure 3-12 The relationship of detection window size and detection throughput as a function of target concentration.

Though the detection throughput could be improved by increasing the target concentration and reducing the size of the detection aperture, there is a lower limit to the latter because of the limits to accurate determination of the (long) luminescence lifetimes of the targets. Recall also that the maximum sample flow rate is set at 0.01 ml/min so as to achieve adequate acoustic focusing, thus the maximum flow velocity is

$$v = \frac{10^3 * Q}{60 * A} = \frac{50Q}{3A} = 0.553 \; mm/s = 0.553 \; \mu m/ms \qquad \textbf{(3-14)}$$

Since the TGL cycle period is 2 ms, targets move a distance 1.106 µm along the microfluidic flow channel in one single TCL cycle at this velocity. With the detection aperture diameter set at $L = 100$ µm for the current system, the transit time Tw for a target crossing the detection aperture is 181 ms at the maximum flow velocity, and the corresponding number of TGL cycles during the transit time is N=~90. The target concentration for maximum throughput is then calculated from Equation 3-13 to be 8350 targets/ml. A little lower concentration, C=8000 targets/ml, was adopted for all experiments to avoid errors in lifetime determination arising from triple or greater target overlap in the detection aperture. Note that this maximum concentration does not represent a serious limitation for many applications and a higher sample throughput may be possible for lower

target concentrations, however, there remains a limitation on maximum flow rate arising from the effectiveness of acoustic focusing.

3.4 Lifetime Determination for Overlapping Events

For the set detection aperture size and maximum target concentration and flow rate, and assuming random arrival rates of targets at the detection aperture, we expect that 77.75 % of TGL cycles will not detect an event, 19.57 % will detect a single event and 2.46 % will detect a double event, the remaining 0.22% detecting three or more events overlapping in the field of view.

The method for determining the luminescence lifetime for single events has been described above, Chapter 3.2.3. The strategy for determining individual lifetimes in a double event is first to distinguish the double-event signals from all the signals observed and then to apply a lifetime decoding algorithm to measure the two lifetimes. Note that all pulse trains corresponding to three or more events are discarded as previously discussed.

3.4.1 Double-Event Signal Recognition

Comparing the single-event pulse trains in Fig. 3-6 and double-event pulse trains in Fig. 3-8, it is comparatively straightforward to identify the features of a double-event signal from the increased number of TGL cycles and the double peaks in the overall signal profile (envelope).

Accordingly, we apply a peak detection algorithm on the smoothed signal profile as Fig. 3-13. Here the blue curve is the plot of maximum signal voltage for every TGL cycle in the pulse train. Note that the background has been removed by applying the integrated signal threshold value A_T as described above (in detail in Chapter 3.2.2) and neighbouring signal trains have been separated by a zero in the signal. The pink line plots a smoothed fitting (*Savitzky–Golay* filter) to the blue, and the peaks of the pink have been labelled with triangle symbols. Additionally, the triangles are coloured red if only one peak was detected in a single pulse train, whereas green and yellow triangles denote the two peaks of a double event detected in the pulse train.
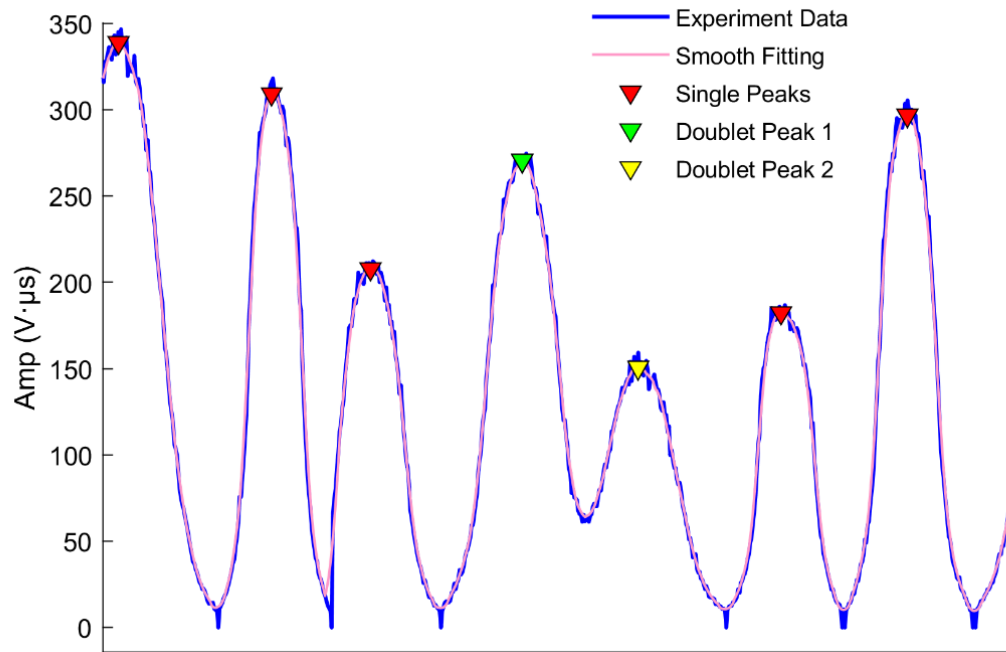
Figure 3-13 Peak detection on the smoothed *A* profile of experiment data.

The number of TGL cycles / signal length (*N*) in each pulse train was also determined to distinguish single- from double-event pulse trains.

The TGL cycle number *N* and the corresponding appearance of double peaks are analysed statistically and each individual pulse train mapped in Fig. 3-14 for cycle number *N* and peak position. Those pulse trains with a single peak are identified with red squares and those with two peaks green squares (the first peak) and yellow squares (the second peak), connected by a dash purple line.

The red squares can be fitted in a line (blue) with slope of 0.4887, demonstrating that profile peaks occur in the middle position of the signal pulse train, and verified the symmetry of the pulse train profile. The distribution of cycle number (sapphire) and peak position (orange) of single event signals are illustrated in Fig. 3-14 also. Average of cycle number *N* and peak position in single event signals are 94.75 and 46.40 respectively, cross-validating the theoretical calculation in Chapter 3.3.2 indicating the expected number of *N*=90 of TGL cycles within a single-event pulse train for the set experimental conditions.
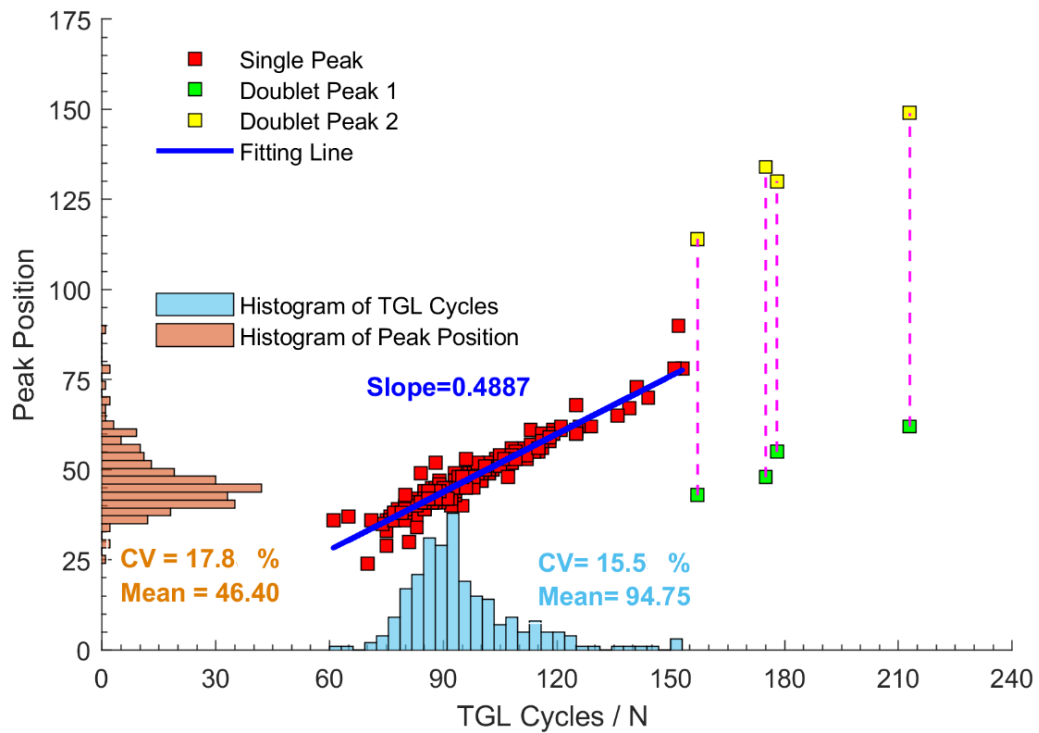
Figure 3-14 TGL cycles number distribution in each segment and the corresponding peak position.

We see also that double-event signals have a longer pulse trains, typically 150 cycles or more, and each has a second peak located after the 100*th* TGL cycle, the first peak located in the same range as those for single-event pulse trains. Thus a double-event signal can be clearly identified from the length (*N*) of the pulse train and dual peaks in the profile.

3.4.2 Determining Lifetimes from Double-Event Signals

When a double-event signal is detected in the real-time voltage data stream, an algorithm for resolving doublet lifetimes is applied to that pulse train. As illustrated in Fig. 3-15, a double-event signal may comprise exponential decay functions with the same (upper chart) or different (lower chart) lifetimes, as well as different signal amplitudes for each event. The two peaks are first detected, and are labelled by green and yellow triangles respectively as described previously. A range of TGL cycles between the two peaks generate signal which results from the combined luminescence of the two targets present in the detection aperture. However, the TGL cycles in advance of the first peak and those following the second peak generate signal arising from the two targets separately. TGL cycles from these two zones (highlighted by the green and yellow boxes) are taken as representative of single target

luminescence and lifetimes calculated from the data by the method discussed above (Chapter 3.2.3). The two events identified from this analysis are recorded as separate events and added to the accumulated event count. Note that the events with two lifetimes in lower panel of Fig. 3-15 are two different biological cell lines (prostate cancer cell DU-145 and bladder cancer cell C3), which are stained separately with two Eu chelates (BHHCT-Eu on DU-145 and BHHBCB-Eu on C3) with different luminescence lifetimes (the protocol and measurements will be presented in the following Chapter 4).
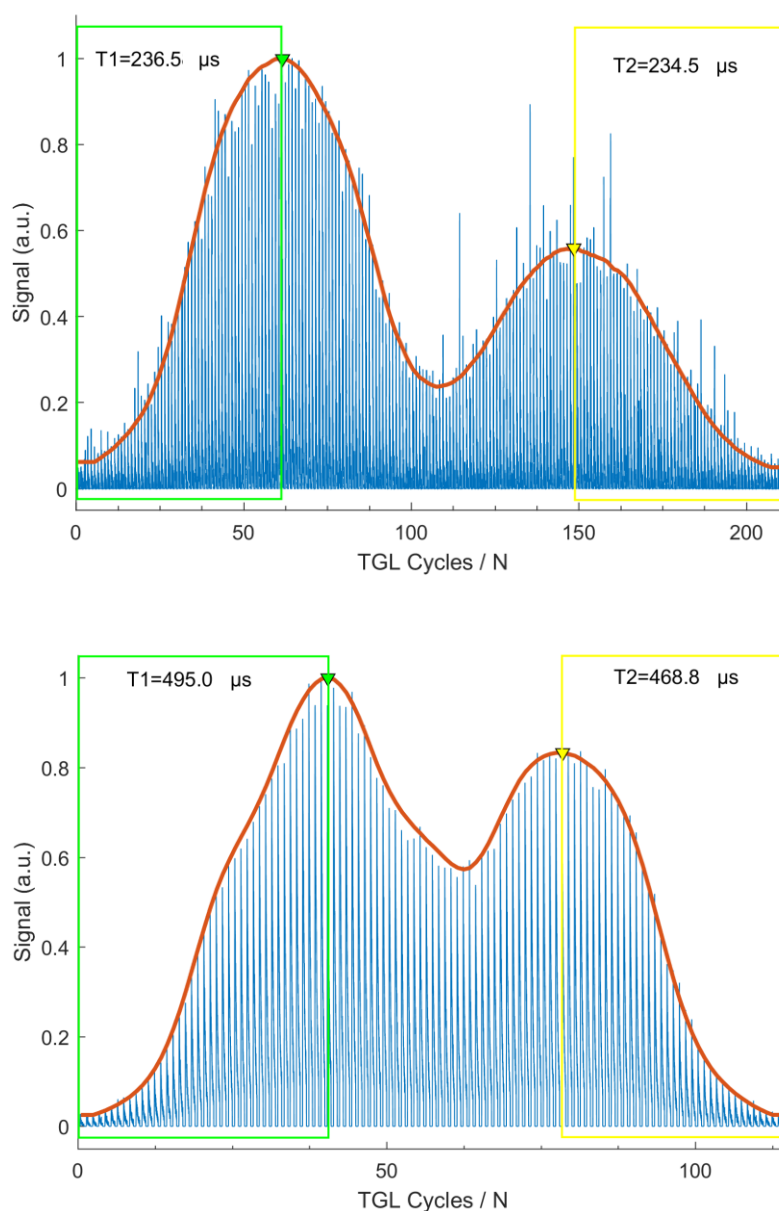
Figure 3-15 Determination of lifetimes for a double-event pulse train. Upper chart: two events with the same lifetime (~235 µs); Lower chart: two events with different lifetimes (~495 µs and ~470 µs).

3.5 Summary

In this chapter, the method of signal processing and extraction of lifetimes from signal trains arising from individual luminescent target have been developed. Overlap probability in a wide field detection was analysed and according to this, suggested settings of parameters of detection aperture size, flow velocity and sample concentration for the time-resolved microfluidic flow cytometry were provided. Overlapping signal trains of cross-talked events were demonstrated and two events overlapping situation can be resolved with the developed program by inspecting the length and the peak of the signal profile. In the next chapter, detection capacity of time-resolved microfluidic flow cytometry will be evaluated with calibrated Eu polymer beads on determination of lifetime, intensity and counting efficiency, which will be cross-validated to the results measured on time-gated microscopy. The acoustic focusing efficiency, and the effect of increasing flow velocity on acoustic focusing efficiency and on detection accuracy of long-live luminescence will be also discussed in Chapter 4.

Chapter 4:   System Evaluation

4.1 Introduction

In Chapter 2, design concepts for microfluidic time-resolved microfluidic flow cytometry were described for a microfluidic flow system, the optical illumination and detection system, and the electronic control system. This included detailed discussion of the instrumental setup, components selections and parameter settings to implement a platform for detecting and analysing long lifetime luminescence (tens of microseconds to millisecond range) from particle or cellular targets. To detect the luminescence with a long decay, the excitation and detection optical apertures were both wide-field, which allowed that several detection events may occur in the observation window simultaneously (event cross-talk or overlap). The probability for such overlap was modelled and analysed in Chapter 3 and it was determined through analysis of sample flow velocity, sample concentration and detection aperture size, which settings for these parameters are optimum to deal with maximum acceptable overlap probability, to give maximum practical throughput.

In this chapter, the capabilities of the time-resolved microfluidic flow cytometer are evaluated where calibrated samples of Eu doped polymer beads with a single defined luminescence lifetime are analysed for identification of target particles via luminescence lifetime determination. Counting efficiency is determined for a calibrated target sample. These results are cross-validated using time-gated orthogonal scanning automated microscopy (OSAM) conducted for the same samples. The effect of acoustic focusing on the determination of lifetime, intensity and counting efficiency are also analysed with calibrated Eu doped microspheres by setting different flow rates, which have an effect on the focusing efficiency. This further validates why acoustic focusing is necessary for detection of long-lived luminescent targets in time-resolved microfluidics flow cytometry, and the reason the flow rate 0.01 ml/min was set.

4.2 Evaluation Materials

A Polystyrene bead sample (Newport Instruments, San Diego, CA, US, $D = 5$ µm, specified concentration $c\% = 0.5\%$ w/v) doped with Eu(TTFA)$_3$ with uniform luminescent lifetimes in the microsecond range has been used for calibration of the time-resolved microsecond flow cytometer. These microspheres (Fig. 4-1) with density of 1.05 g/cm^3 are characterised by narrow-band luminescence at ~615 nm, and luminescence lifetime around 250 µs under the excitation peak wavelength at ~370 nm, which is suitable for evaluation of lifetime decoding on the time-resolved flow platform. The bead diameter $D=5$ µm, is the minimum value in the range of events size that we could be testing on this instrument (5 -20 µm).
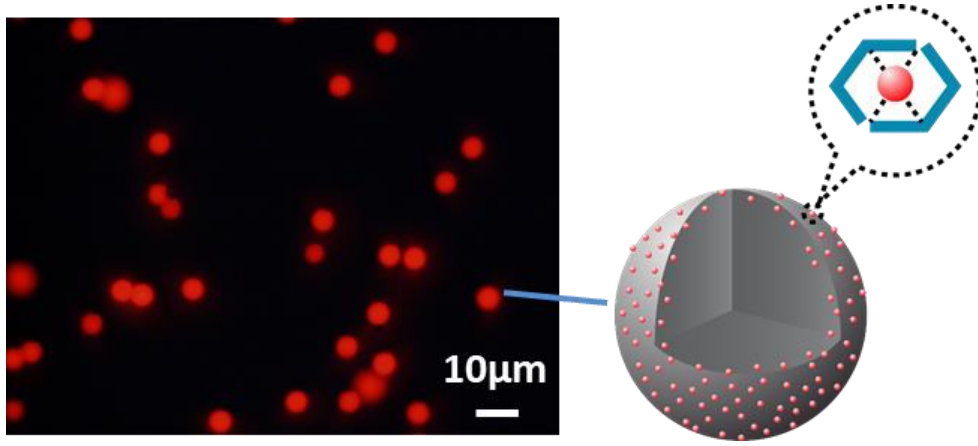
Figure 4-1 5 µm TTFA-Eu doped polymer beads under UV excitation.

Density of polystyrene is $\rho=1.05$g/cm^3, so the expected number concentration of the beads c_n based on the manufacturer-specified w/v concentration is given by:

$$c_n = \frac{6 \times c \times 10^{10}}{\pi \rho D^3} \; /ml \qquad\qquad\qquad \textbf{(4-1)}$$

from which we calculate the bead number concentration of the sample to be 7.28×10^7/ml.

4.2.1 Count with Commercial Flow Cytometry

The actual values of the polymer bead number concentration in diluted suspension were measured on a commercial flow cytometry (BD Influx cell sorter, BD Bioscience) by counting events in a certain examined volume. We diluted the original beads suspension by 50 times, by adding 10 µl of the well-mixed solution into 490 µl MiliQ water. The prepared

samples were then analysed on the Influx cell sorter for 100 seconds with 350 µl of suspension examined in each run. The counts of events in the suspension were calculated based on the forward scatter (FSC) and side scatter (SSC), as plot in Fig. 4-2.
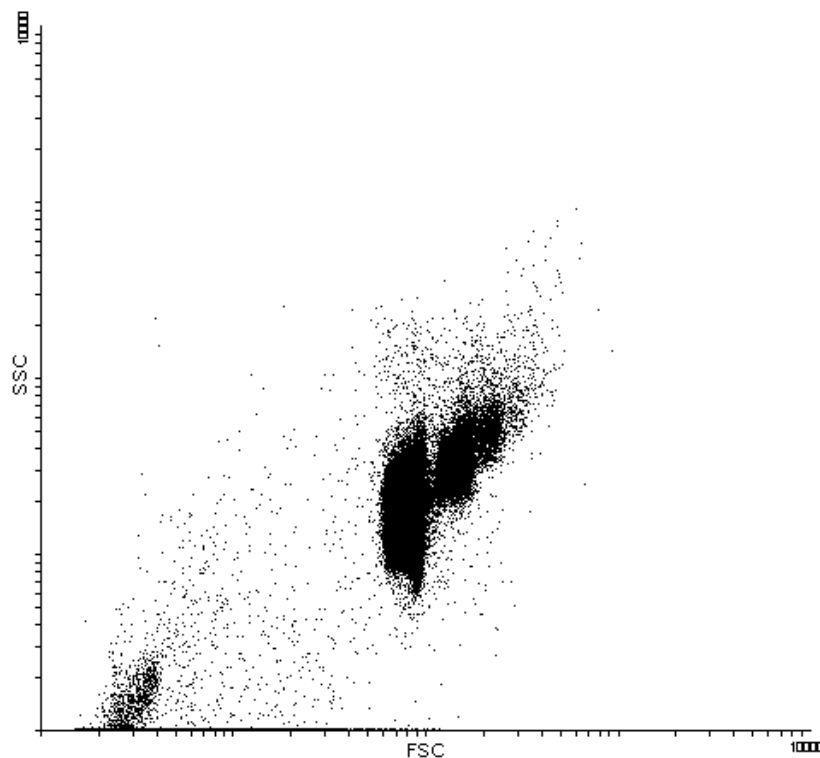
Figure 4-2 Events counts in 350 µl of Eu doped polymer beads suspension (50 times diluted of the original suspension), on a commercial flow cytometry, BD Influx.

Three samples of 350 µl 50 times diluted beads suspension were measured on the platform, counting 156570, 178681, 174118 events respectively. So the average events count is 169790 in 350 µl suspension, resulting in a measured number concentration of around for the original sample as 2.43×10^7/ml, which is 33.38% of the manufacturer-specified number concentration.

Table 4-1 Count of three beads suspension samples detected on BD Influx.

	A	B	C
Detection time	100 s	100 s	100 s
Detected volume	350 µl	350 µl	350 µl
Count	156570	178681	174118

4.2.2 Lifetime Inspection on TGL Microscopy

The luminescence lifetimes of the beads were initially measured on a time-gated luminescence microscopy (TGL microscopy)[56,143] after spin-coating the polymer beads on the glass slides. Image processing software was employed to calculate the luminescence lifetimes after taking a series of periodical delayed images; the user interface provides a false colour scale of lifetime for convenient visualisation. Fig. 4-3 shows a typical example of screenshots of lifetime measurements for the TTFA-Eu beads derived from TGL microscopy, wherein the mean lifetime of the beads in the FOV is determined to be 250 µs. The average lifetime of pixels within each bead are labelled manually on Fig. 4-3.
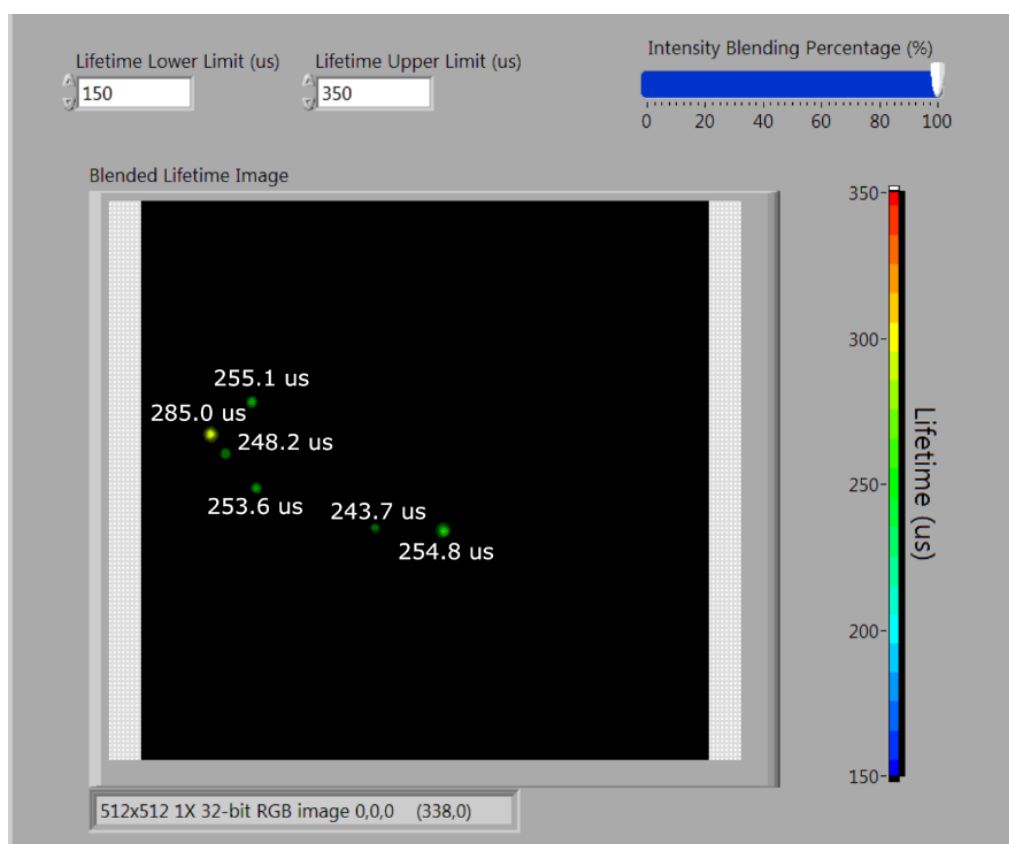
Figure 4-3 Lifetime of 5 µm Eu-doped calibrated beads are examined using TGL microscopy, and the average lifetime of pixels within each bead are labelled manually aside.

After detecting 13 of the Eu beads in a few different FOV, the luminescence lifetime of the beads distributes in the range 242 ± 17 µs according to the measurement results on TGL microscopy, as in Tab. 4-2.

Table 4-2 Lifetimes of polymer beads detected on TGL microscopy.

No.	Lifetime of Beads (µs)
1	285
2	248
3	255
4	254
5	244
6	255
7	235
8	229
9	225
10	235
11	227
12	231
13	228
Mean	242
CV	7.0 %

4.2.3 Measurements on OSAM

To get more detailed statistical analysis of these calibrated Eu-doped polymer beads, we measured the lifetime, intensity and counts of the beads on the time-gated orthogonal scanning automated microscopy (OSAM)[93]. Three samples were prepared by adding 10 µl of the 2000 times diluted Eu beads suspension on a glass slide and covered by a 5 cm × 2.5 cm slip respectively. OSAM scanned the glass slide within a 50000 µm × 24000 µm area of the cover slip, starting at one of the slip corner as the origin. The OSAM worked in a time gated mode with 106 µs gating time, wherein during the first 100 µs, the UV excitation was on. The excitation frequency was 1 kHz, so the TGL period was 1 ms. The long decay luminescence of the Eu doped targets was collected in an 894 µs interval after a 6 µs delay time towards the UV excitation. The coordinates of the targets on the slides and their luminescence lifetimes were resolved and recorded after the automated scanning of OSAM, as shown in Fig. 4-4 and Tab. 4-3.
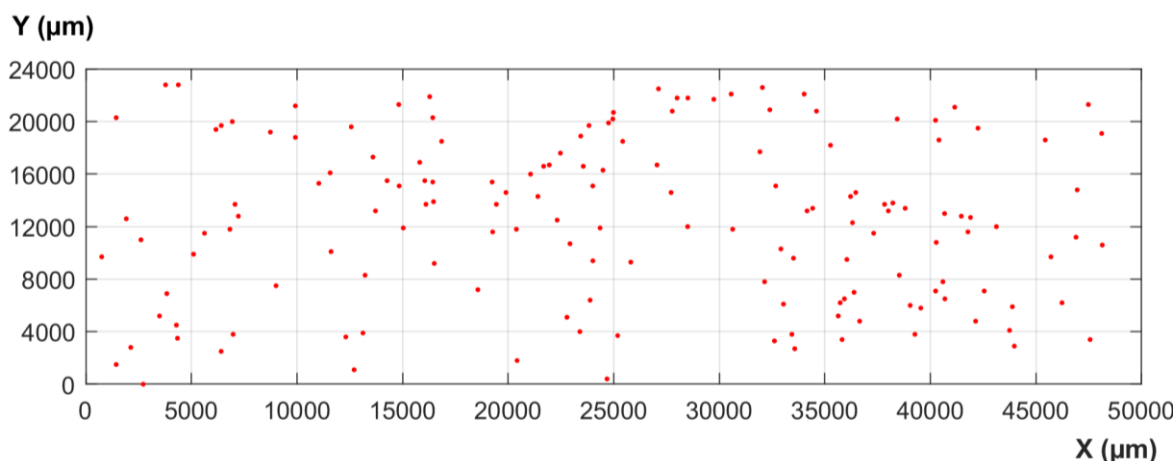
Figure 4-4 Eu doped polymer beads detected on one of the glass slides by OSAM. The scanning area is 50000 µm × 24000 µm.

The lifetime, intensity and counts of the beads detected on three slides are as shown in Tab. 4-3. The intensity is defined as the area under the luminescence decay curve. As measured on OSAM, the lifetimes of the calibrated beads are in the range 250 ± 7 µs, with a coefficients of variation (CV) of less than 2.9 %, which is consistent with, but more accurate than the detection results of TGL microscopy. The intensity has a broader distribution in 50 ± 25 µV·s, with CV around 50%. This could be because the beads themselves have a large range of intensity owing to the size variation, and also considering the beads between glass slides and cover slip could be off focal plane when they are not all in the same layer, which will contribute to broadening the intensity distribution as well. The average counts on the slides are 136, so the number concentration of the original suspension of the beads is calculated as 2.72×10^7/ml, close to the results we got from commercial flow cytometry, BD Influx.

Table 4-3 Lifetime, intensity and counts of the targets detected on three glass slides by OSAM.

	Slide 1	Slide 2	Slide 3
Lifetime (µs)	251±6	249±7	252±7
CV of Lifetime	2.5%	2.9%	2.6%
A (µV·s)	51±24	49±29	48±23
CV of A	47.6%	59.1%	47.9%
Target Counts	136	160	111

The preliminarily measured Eu-doped polymer beads are used as the evaluation samples to evaluate the capacities of time-resolved microfluidic flow cytometry (TRMFC) on

detection of long-lived targets. As discussed in Chapter 3, the number concentration of samples detected by time-resolved microfluidic flow cytometry is required to be no higher than 8000 /ml for minimum counting event overlap probability. The beads suspensions for system evaluations of the TRMFC were prepared by diluting the original suspension 10^4 times with MiliQ water to get samples with concentration around 2500 beads/ml according to the OSAM and BD Influx counts. The suspension of beads was well mixed by vortex for 20 s before each counting run. Ultimately the results of lifetime-determination, luminescence intensity and count efficiency by TRMFC will be cross-validated against those results obtained for BD Influx, TGL microscopy and OSAM, as in Table. 4-4.

Table 4-4 Schema for cross-validation of results for TRMFC and analysis of Eu-doped bead samples on different platforms

Evaluation items	BD Influx	TGLM	OSAM	TRMFC
Lifetime		√	√	√
Intensity			√	√
Count efficiency	√		√	√

4.3 Detection Accuracy

According to the discussions in Chapter 2 and Chapter 3, the acoustic focusing based time-resolved flow cytometer was working under pre-set parameters (see Tab. 4-5) when evaluating the system capacities of lifetime, intensity and counts resolving by long lifetime luminescent targets detections. All subsequent experiments were conducted in the same settings as below unless detailed otherwise.

TTFA-Eu doped beads suspensions were prepared as mentioned above in 4.2 for detection on time-resolved microfluidic flow cytometry. Prepared sample (0.5 ml) was added into four vials respectively after vortex for 20 s to ensure the beads are well suspended. The four identical samples (denoted S1-S4) were then drawn into a 1 ml syringe to load into the microfluidic flow pump system for detection in the time-resolved microfluidic flow cytometer. Note that based on the dilution and volume of each of the samples, the number of calibrated beads which might be detected is approximately 1250, however, due to a number of processes the number which are presented to the microfluidic channel for detection are substantially reduced, as discussed below.

Table 4-5 Prearranged parameters on acoustic focusing time-resolved microfluidic flow cytometry.

Items	Parameters
Acoustic Device	F_1 = 1.272 MHz (horizon), F_2 = 1.430MHz (vertical)
Driving Signal	Shifting frequency f_s = 5Hz, V_{pp} = 20V
Flow Rate	10 µl/min
Flow Velocity	0.553 mm/s
PMT Gain	10^6 A/A
Amplifier Gain	10^4 V/A
Sampling Rate	200 kHz
TGL Cycles Period	2 ms
UV Pulse On / Off	0.8 ms / 1.2 ms
PMT Pulse On / Off	1.195 ms / 0.805 ms
UV w/ PMT Delay	5 µs.
Detection Aperture	100 µm
Sample Concentration	2500 events/ml
A_T Threshold	4.0 V·µs

Fig. 4-5 shows the luminescence lifetime distributions detected for polymer beads in the S1-S4 samples. Average lifetimes and coefficients of variation (CV) for the lifetime distribution are given in Table 4-6. The results show the average lifetime of the calibrated Eu beads measured by the TRMFC is around 250 µs, matching well with the results of the same beads detected on the OSAM (Tab. 4-3), with CV of 2.4%, showing quite narrow distributions.
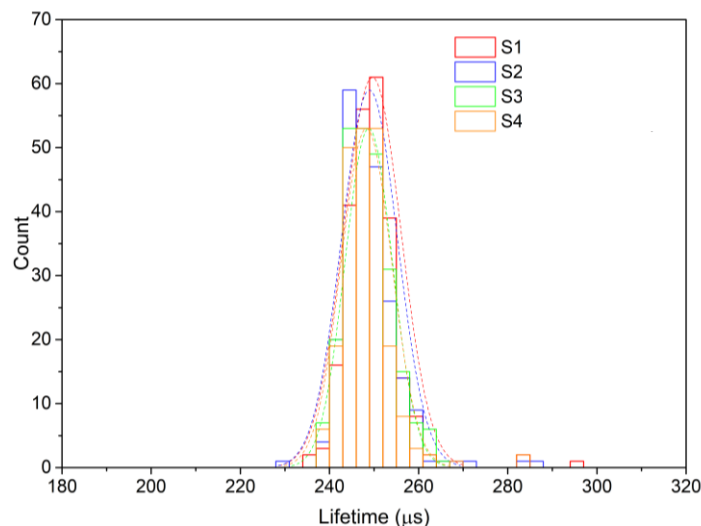
Figure 4-5 Lifetime distributions of measurements of four Eu-doped polymer beads samples. Lifetime CV of S1-S4 is about 2.5 %.
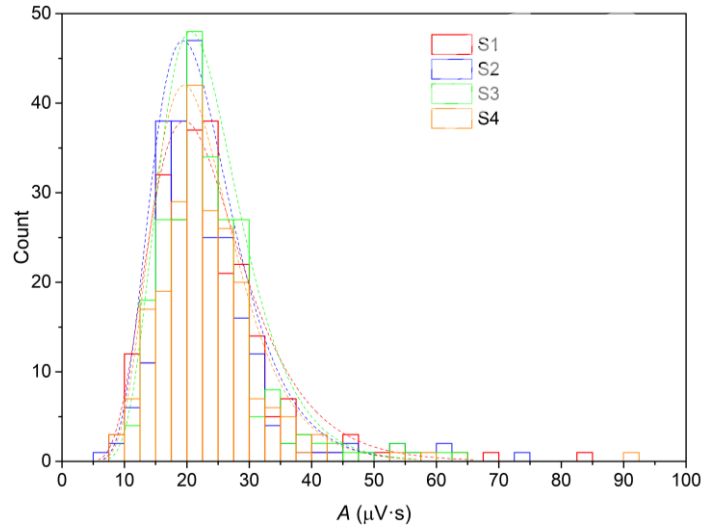
Figure 4-6 Amplitude distributions of four samples of Eu-doped polymer beads. Amplitude CV of S1-S4 are about 40%.

We defined the area under the signal decay as amplitude (A), which is used to describe integrated intensity of events. Amplitude distributions of samples S1-S4 are shown in Fig. 4-6. The average integrated intensity of the beads is about 23 µV·s, with CV of around 40%, where the average and the variation are both lower compared to the measurements on OSAM in Tab. 4-3. The integrated intensity results of measurements on OSAM and TRMFC are not the same because of different amplifier gains (10^4 V/A on TRMFC and 10^5 V/A on OSAM) and different TGL period and duty (gate on/off: 805 µs / 1195 µs for TRMFC and 106 µs / 894 µs for OSAM). The variation of intensity detected on TRMFC (~40%) is lower than OSAM (~50%) because the acoustic stream focusing technique on TRMFC helps to force the flowing targets onto the focal plane of the objective, making the intensity results more accurate. The targets are distributing in the different layers in between the glass slides for the OSAM measurements, which could be improved by spin coating the samples on the glass surface[1].

Table 4-6 Detection results of S1-S4 for time-resolved microfluidic flow cytometry.

	S1	S2	S3	S4
Volume (ml)	0.5	0.5	0.5	0.5
Lifetime (µs)	250±6	249±6	249±5	248±6
CV of Lifetime	2.6%	2.5%	2.1%	2.3%
***A* (µV·s)**	24±11	23±9	24±9	23±9
CV of *A*	45.0%	38.4%	35.6%	37.2%
Counts	245	239	242	224
Count Efficiency	19.6%	19.1%	19.4%	17.9%

The expected counts of the Eu calibrated beads which might be detected in 0.5 ml of 2500 beads/ml samples should be approximately 1250 based on the measurements on BD Influx (Tab. 4-1) and OSAM (Tab. 4-3). But the counts of S1-S4 obtained for TRMFC (Tab. 4-6) are less than 20% of the expected number. The primary cause of this is that the polymer beads settle to the bottom of the (horizontally-mounted) syringe pump over the 50-minute duration of the measurement due to their higher density than MiliQ water (the syringe is fixed in position so that it cannot be agitated to maintain a uniform suspension). This issue can be circumvented by changing the orientation of the syringe pump to the vertical and/or resolved by matching the liquid suspension density to that of the polymer beads, for example by using a saline buffer.

However, because density matching depends on the specific targets, it is not a general method to solve the problem. The syringe pump of the TRMFC was therefore remounted to the vertical axis, and the counting efficiency tested with the same dilution of microbeads suspension four times, 20 mins for each measurement (denoted S1'-S4', 0.2 ml, ~500 events expected to be detected). The counts of S1'-S4' are detailed in Tab. 4-7, 450-500 events detected, which are more than 90% of the input sample number, a vast improvement compared to the previous experiments with horizontal syringe pump, wherein less than 20% of the expected events were counted.

Table 4-7 Detection results of S1'-S4' for time-resolved microfluidic flow cytometry (vertical syringe pump).

	S1'	S2'	S3'	S4'
Volume (ml)	0.2	0.2	0.2	0.2
Lifetime (µs)	250±6	249±6	249±5	248±5
CV of Lifetime	2.2%	2.3%	2.2%	2.1%
A (µV·s)	22±10	22±9	21±10	22±11
CV of A	45.6%	39.8%	46.8%	50.5%
Counts	478	457	501	456
Count Efficiency	95.6%	91.4%	100.2%	91.2%

Compare the results in Tab. 4-6 and Tab. 4-7, the lifetime and intensity measurements are consistent, meaning that the orientation of the syringe pump did not change the accuracy of lifetime and intensity detection. However, the count efficiency increased from ~19% to more than 90% because the pump was vertical so that the settling beads could still flow into the tubing from the syringe and then through the microfluidic channel. The count efficiency

could be further improved by vertically orienting the microfluidic channel as well, which is currently mounted horizontal on the stage of an upright microscope (BX51, Olympus). For commercial flow cytometers currently available, the sample fluidic stream is commonly vertical, and the it is likely that optimising the physical arrangement of the time-resolved microfluidic flow cytometer can give further enhancements in performance.

4.4 Evaluation of Acoustic Focusing

As we found in the experiments of 4.3.1, the acoustic focusing increased the intensity resolving accuracy by forcing the targets onto the same layer as the focal plane of the objective on time-resolved microfluidic flow cytometry compared to OSAM. In this section, we analyse the performance of the TRMFC for detection of calibrated microbeads sample, but for different acoustic focusing settings, to understand how well focused the beads are in the microfluidic channel and what the effects of acoustic focusing at different levels have on the resolving accuracy of the system.

4.4.1 Acoustic Focusing Efficiency

In order to analyse the efficiency of acoustic focusing in the stream, videos (696×520, 26 frames/second, 405 pixels / 100 µm) of focusing of 15 µm blank polymer beads in the microfluidic channel were recorded with a digital camera (Lu165M, Lumenera) under bright field of view. These videos of the acoustic focusing dynamics commenced with beads flowing freely with the acoustic drive turned off, and then when the beads were forced to the stream centre but flowing in different layers when one-dimension acoustic drive (1D acoustic, horizontal across the channel) is activated, and finally the beads focussed in a linear train when two-dimension acoustic (2D acoustic, horizontal and vertical across the channel) is activated (as shown in video screenshots in Fig. 4-7).

Frames of acoustic off, 1D acoustic focusing and 2D acoustic focusing were extracted respectively in 5 seconds clips (130 frames in each condition), and the 696×520 images were processed in Matlab to count pixels along the width of the frames where beads are flowing by. The histogram of pixels in Fig. 4-7 represent the distribution of beads in the stream across [-64.2 µm, 64.2 µm] the microfluidic channel, where 0 µm is the centre.

Table 4-8 Data for of microbeads distribution across the microfluidic channel in three focusing settings.

	Acoustic off	1D Acoustic (Horizontal)	2D Acoustic (Horizontal-Vertical)
PZT Driving Signal	NA	F_1=1.272MHz(Horizon) V_{pp}=20V	F_1=1.272MHz(Horizon) F_2=1.430MHz(Vertical) f_s = 5Hz, V_{pp} = 20V
Pixel	292±132	235±10	263±10
Distance from central plane/axis	8.0±32.7µm	-6.3±2.5 µm	0.6±2.6 µm
CV of Pixel	45.3%	4.3%	4.0%

The statistics of results for the data of Fig. 4-7 are listed in Tab. 4-8, where we find that when the 1D acoustic was turned on, the beads are forced to the middle of the channel, however there was about 6 µm deviation to the centre of the stream. With 1D focusing, even though the beads are pushed to the middle from the top view with CV of 4.3%, they distributed in different layers, three beads in lower level of focal plane shown as dark shadows in 1D Acoustic Focusing of Fig. 4-7. When the acoustic drive in both orientations was on, the beads are in the middle of the channel (pixel 263, 0.6 µm) with CV of 4.0%, and they flow along a single axis at the centre of the microfluidic channel, coincident with the focal plane of the detection optics, so permitting for accurate intensity measurements.
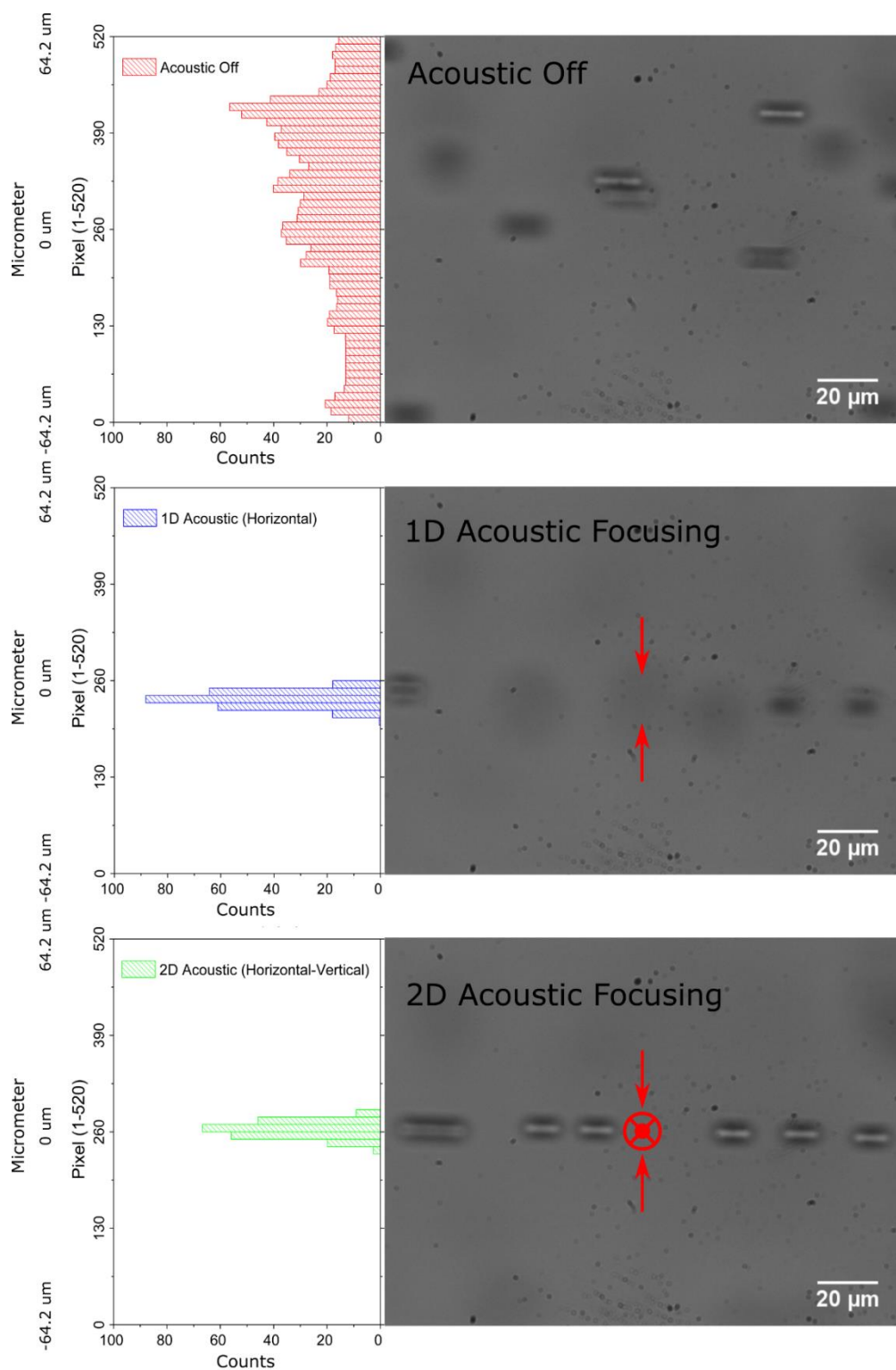
Figure 4-7 15 µm blank polymer beads travelling in the microfluidic channel at 0.01 ml/min flow rate, and their distributions across the channel width under three focusing conditions (unfocused, 1D acoustic focusing and 2D acoustic focusing) are plot.

4.4.2 Detection Accuracy Comparison

The effect of acoustic focusing on determination of luminescence lifetime was examined using 5 µm Eu doped calibrated beads, as prepared in Chapter 4.2. The analysis was conducted for two focusing conditions, with 2D acoustic focusing on and off. A volume 0.1 ml of the microbeads suspension (~2500 beads/ml) was analysed for acoustic drive on and off respectively. The results are shown in Tab. 4-9.

Table 4-9 Detection results of calibrated Eu beads with and without 2D acoustic focusing.

	Acoustic on (2D)	Acoustic off	Acoustic off
Test Time (mins)	10	10	25
Lifetime (µs)	250±6	249±6	250±7
CV of Lifetime	2.4%	2.4%	2.8%
A (µV·s)	25±8	16±8	17±8
CV of A	30.7%	45.7%	46.9%
Counts	231	61	158
Count Efficiency	92.4%	24.4%	25.3%

Note that the expected target counts in 0.1 ml of beads suspension is ~250 events. Since the count number for the first acoustic off experiment (the second column in Tab. 4-9), was only 24.4 % of the expected counts, a third sample of microbeads suspension was examined for acoustic focusing off over a test time of 25 mins. In this latter case 0.25 ml of sample flowed through the channel, with 625 beads expected to be counted, though only 158 events were detected (25.3% of the expected number, similar to the other acoustic-off experiment). By contrast for the experiment with acoustic focusing applied, 231 events, 92.4% of the expected counts were detected with all the other experiment conditions the same as Tab. 4-5. It is easy to understand the reason of losing counts when acoustic is off because the beads distribute outside of the detection aperture, which is 100 µm, determined by overlap probability discussed in Chapter 3. Thus the acoustic focusing is necessary to force all the events into the detection aperture in the middle of microfluidic channel with a minimum of events going undetected.

The lifetime determination results are similar for all three samples analysed independent of the focusing conditions in Tab. 4-9. However, the integrated intensity measured for the unfocused beads (~17 µV·s) is lower than for 2D acoustic focusing (25 µV·s). This is because without acoustic focusing most of targets are not in the focal plane of the optical detection system when they flow through the detection aperture.

It follows that the acoustic focusing function is necessary in the time-resolved microfluidic flow cytometry. Though the lifetime determination is little affected, accuracy of intensity measurements and particularly count efficiency are decreased dramatically when acoustic focusing is not activated.

4.5 Effect of Flow Velocity

As the flow velocity increases, the effectiveness of acoustic focusing[38,107] declines as discussed in Chapter 1, so that characterisation of the luminescence signal from targets is also affected. In this section, in order to understand the effect of increasing flow velocity on the detection results, we compared the focusing degree, accuracy of lifetime and intensity and count efficiency of calibrated Eu doped polymer microbeads (diameter 5 µm) when they are flowing at different rates in the microfluidic channel, with acoustic focusing on.

4.5.1 Effect on Focusing Efficiency

Videos (26 frames/second, 696×520, 405 pixels / 100 µm) of 5 µm Eu doped beads travelling in the stable, 2D acoustic focused stream were recorded for seven different flow rates under continuous wave (CW) UV excitation. Clips of one minute were randomly selected in seven videos respectively and processed frame by frame in Matlab to image the trace of beads traversing the microfluidic channel, so as to analyse the efficiency of acoustic focusing over different flow rates. The trace of all UV excited Eu beads in one minute of videos can be visualised by accumulating all the frames into one image, as shown in Fig. 4-8.

The transverse distribution of microbeads for four flow rates, 0.006 ml/min, 0.010 ml/min, 0.15ml/min and 0.020 ml/min are shown in Fig. 4-8. The Eu beads show white colour in greyscale images under UV excitation, as presented in the images: the white band represents the profile of microbeads distribution. In the first two images, the trace bands are narrow and concentrated, however in the latter two the transverse profile becomes scattered and the width increases dramatically as the flow rate raised, to ~108 µm when the flow rate was 0.020 ml/min. This indicates that a significant number of targets would not be visible to the detection system at high flow rates, 0.020 ml/min or higher, because diameter of the detection aperture is only 100 µm as discussed in Chapter 3. In this context it is noted also

that the maximum permissible flow rates for effective acoustic focusing depend also on the size of the target particles: the larger the diameter, the higher the maximum flow rate.
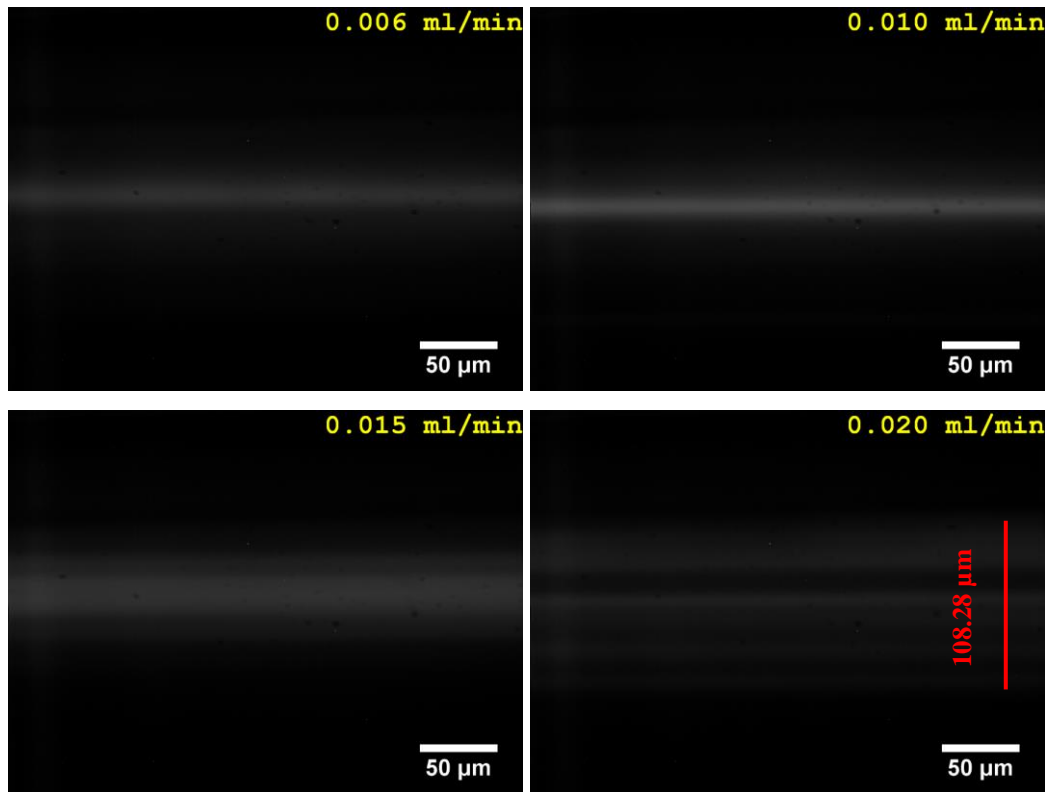
Figure 4-8 Transverse distribution of Eu microbeads under UV excitation at different flow rates.

Though the white bands are both narrow in pictures of 0.006 ml/min and 0.010 ml/min in Fig. 4-8, the band for 0.010 ml/min is the brighter of the two, since a larger number of beads are detected for the same ample concentration and exposure time, coincident with the higher flow rate. Note that the shift vertically of the trace bands in the two images is due to minor movement of microscopy stage between the two experiments.

The transverse distributions of microbeads population across the width of the channel are plotted into histograms for 7 different flow rates as in Fig. 4-9, with related statistical data given in Tab. 4-10.

Table 4-10 Distribution of trace band of 5 µm beads across the width of the channel at different flow rates.

Flow rate	Flow velocity	Pixel	CV of Pixel
0.006 ml/min	0.332 mm/s	252±13	5.1 %
0.008 ml/min	0.442 mm/s	256±15	5.8 %
0.010 ml/min	0.553 mm/s	265±16	5.9 %
0.012 ml/min	0.664 mm/s	251±21	8.3 %
0.015 ml/min	0.830 mm/s	247±27	11.1 %
0.017 ml/min	0.940 mm/s	252±39	15.5 %
0.020 ml/min	1.106 mm/s	251±63	25.0 %

As we can see in Fig. 4-8 and Tab. 4-10 that the stream can be perfectly focused by the acoustic in the flow rate of 0.010 ml/min, which is also consistent with the calculations of the maximum flow velocity permitted for beads well-focused in Chapter 2. However, in practical lifetime detections, the resolving results are still acceptable (see in Fig. 4-11) when the flow rate increases to 0.020 ml/min, wherein the detection throughput has been improved twice compared to that at 0.010 ml/min. Though the beads are not finely focused into a string along the microchannel at the rate of 0.020 ml/min, the targets are still visible within the size of FOV (dimeter 100 µm) in a narrow ~108 µm trace band.
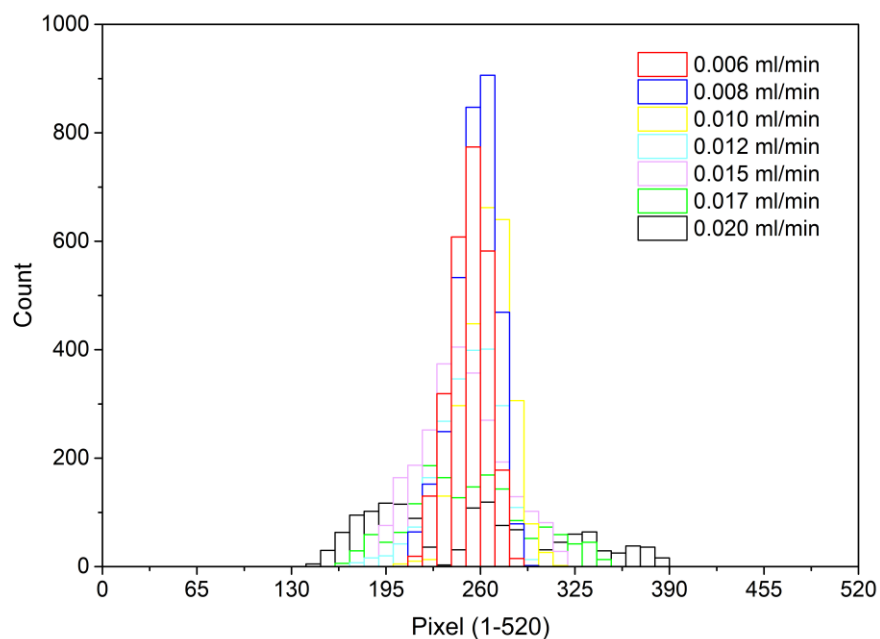
Figure 4-9 Histogram illustrating transverse profile of microbeads flow through the channel at different flow rates.

4.5.2 Effect on Detection Accuracy

Increase in fluid flow rate is seen to decrease acoustic focusing efficiency, and the highest flow rate is 0.02 ml/min in order to count all the events in the sample suspensions. It follows that flow rate also influences the detection accuracy, i.e., lifetime determination, intensity and count efficiency, in the detection of Eu doped calibrated beads. In the following experiments using the same volume of microbeads suspension, 0.1 ml, and stable 2D acoustic focusing, lifetime determination, intensity and counts efficiency were examined for five different flow rates spanning 0.006 to 0.03 ml/min, as shown in Tab. 4-11.

Table 4-11 Resolving results of detecting 5 µm Eu calibrated beads at different flow rates.

Flow rate	Time	Lifetime(µs)	CV of Lif.	A (µV·s)	CV of A	Count
0.006ml/min	1000s	249±4	1.8%	23±6	28.3%	49
0.010ml/min	600s	249±5	2.2%	24±8	30.7%	225
0.015ml/min	400s	249±6	2.3%	25±9	34.0%	267
0.020ml/min	300s	249±6	2.3%	24±9	36.6%	273
0.030ml/min	200s	250±6	2.3%	19±7	36.6%	112

There are five groups of data in Tab. 4-11, with three of them measured at lower flow rates than 0.020 ml/min, one group equal to it and the last one higher. Comparing the data for the five flow rates, we see that the lifetime distribution differs little between groups, though the CV slightly increased as the flow rates rise. The same trend was seen for intensity results, however the average intensity for 0.030 ml/min flow rate is much lower than the four lower rates because the low focusing efficiency at high flow rate results in many beads transiting outside the focal plane of objective of the detection system. The results show that neither flow rate nor the acoustic focusing have any great effect on measured lifetimes, but higher flow rate decreases the accuracy of intensity measurements.

As for the count of target events, the counts data might be expected to be similar for all five flow rates because the volume (0.1 ml) of microbeads samples are the same. The expected counts are ~250 according to the measurements by BD Influx and OSAM reported in Chapter 4.2. However, the number of counted events for the lowest flow rate of 0.006 ml/min is ~50, only 20 % of the expected counts. Though all the experiments here were conducted with the syringe pump vertically oriented, the microbeads are inclined to stick to the wall of syringe or the microfluidic channel over the long run times (approaching 20 minutes) at the lowest flow rates. When the flow rate was increased to 0.01 ml/min, reducing

run time and microbeads loss to the walls, the event count was 225, ~90 % of the expected number, quite consistent with the results in Chapter 4.3. As the flow rate increased to 0.015 ml/min or 0.020 ml/min, the event counts are both about 270, effectively 100% of the expected count number given experimental uncertainties associated with sample concentration. However, the event count number decreased to 112 when the flow rate is increased to 0.030 ml/min, with count efficiency reduced to 44.8%. This can be explained by the conclusions in Chapter 4.5.1, where we demonstrated that an increasing number of beads lie outside the detection aperture at flow rates above 0.02 ml/min due to ineffective acoustic focusing.

It is noted that according to the acoustic focusing results shown in Tab. 4-10 and Fig. 4-8, we had set the flow rate at 0.010 ml/min for best TRMFC performance, however considering highest sample throughput while maintaining sufficient detection accuracy as shown in the preceding sections, flow rates between 0.015 ml/min-0.020 ml/min are certainly viable. Alternatively, a possible method we could consider to increase the detection throughput is by measuring the rise to the maximum of the individual target peaks, instead of resolving them in the way discussed in Chapter 3. In this circumstance, the second peak of a double events could still be discriminated using the rising signal points and the maximum in most cases (unless the peaks are superimposed). The number of data points per event would be fewer, and the event throughput rates could be increased.

4.6 Summary

Calibrated suspension samples Eu doped polymer beads (~2500 beads/ml) have been used to evaluate the detection accuracy of lifetime, intensity and count efficiency on time-resolved microfluidic flow cytometry (TRMFC). The calibrated beads were firstly measured on commercial flow cytometry (Influx cell sorter, BD), time-gated microscopy (TGL microscopy) and time-gated orthogonal scanning automated microscopy (OSAM) for cross validating the results on TRMFC. The lifetime determination results on TRMFC (250 µs, CV ~2.3%) are consistent with those on OSAM and TGL microscopy (250 µs, CV ~2.6%), and the range of intensity distributions of calibrated beads detected on TRMFC (CV ~45%) are narrower than those on OSAM (CV ~50%), due to the acoustic focusing capability of TRMFC. However, the counting efficiency for target events using TRMFC was initially only ~20% of the number of OSAM and BD Influx, which was caused by the settling of the denser

beads in a relative slow flow stream within the horizontally-oriented syringe pump. This was solved by mounting the syringe pump on the vertical axis, improving the counting efficiency from less than 20% to more than 90% of the expected number.

The acoustic focusing efficiency was evaluated by comparing the flying trace of 15 µm blank polymer beads under bright field when acoustic was off, 1D acoustic and 2D acoustic mode. Accuracy in discriminating luminescence lifetime, intensity and counting efficiency of 5 µm Eu calibrated beads were also measured and compared under two conditions to analyse the effect of acoustic focusing on detection results. In order to make all targets transit the detection aperture within the focal plane of the objective, 2D acoustic focusing is required. As for the effect of acoustic focusing on detection results, the average lifetimes and the CV are relatively insensitive to acoustic focusing geometry, but average detected intensity is lower and the distribution is broader when there is no acoustic focusing because Eu beads are detected at positions out of the focal plane. Worse, the counting efficiency is very low without acoustic focusing, but rises to 90% and as high as 100% when acoustic focusing is activated. In brief, 2D acoustic focusing is an essential element in the time-resolved microfluidic flow cytometry system to ensure best detection accuracy, particularly in respect of counting efficiency.

The effect of increasing flow velocity on the acoustic focusing and detection accuracy were analysed with 5 µm Eu beads flowing at different rates. Through analysis of videos of flowing UV-excited beads, it is clear that increase of flow rate beyond an optimum value will reduce the efficiency of acoustic focusing dramatically. Flow rates under 0.010ml/min can provide the best focusing results for 5 µm polymer beads and while flow rates higher than 0.020 ml/min results in weaker focusing and loss of targets outside the detection aperture. When evaluating the effect of flow rates on detection results, the resolved lifetimes are consistent across different rates, but the intensity and counting efficiency is adversely affected when the rate is higher than 0.020 ml/min because of the weak acoustic focusing. Simultaneously, if the flow rate is lower than 0.010 ml/min, counts will be less than 80% of expected number because of loss of microbeads to the walls on the syringe pump and the flow channel. Flow rates of 0.010-0.020 ml/min are suggested as optimum for detection of 5 µm Eu beads.

In the next chapter, a lifetime multiplexed bioassay will be established by staining two cell lines with three varied Eu chelates and the mixture of two populations with distinct lifetime

codes will be detected on the TRMFC to demonstrate the lifetime-based multiplexing detection on this platform.

Chapter 5:   Multiplexing Detection

5.1 Introduction

The previous Chapter 4 System Evaluation reported evaluation of the Time-Resolved Microfluidics Flow Cytometer (TRMFC) in respect of determination of lifetime, signal intensity and counting efficiency for single-lifetime luminescent Eu^{3+}-doped polymer microbeads. Results showed that lifetimes could be determined with high accuracy, specifically with Coefficients of Variation (CV) 2% for the Eu beads. The counting efficiency is more than 90% of the expected number when the syringe pump is mounted vertically in order to prevent the denser beads settling to the bottom of the syringe. Lifetime and intensity measurements using TRMFC are in agreement with those obtained with OSAM for the same samples, and the counting efficiency results are consistent with the measurements on commercial flow cytometry. The comparatively small variation in lifetime measurements enables TRMFC to discriminate effectively a large number of lifetime channels within the range of lifetimes (30 µs to 2000 µs) provided by lanthanide (e.g., Eu^{3+}, Tb^{3+}) chelates. In this chapter, a lifetime multiplexed TRMFC bioassay involving two different cancer cell lines is designed, tested and evaluated.

As noted in Chapter 1 Introduction, the excited state lifetimes (and quantum yields) of lanthanide complexes are strongly dependent on the coordination environment of the lanthanide ion.[119] Binding events, changes in hydration/solvation and changes in ligand coordination mode to Ln^{III} can each affect the emission lifetime of the complex, inducing changes of hundreds of microseconds in some cases[155]. More specifically, the luminescent lifetime τ of lanthanide complex can be influenced by a number of biochemical components in the intracellular/intercellular environment[59,156,157] and for example, may even be different for different growth phases of the same cells[53,161]. This is clearly a phenomenon which must be taken into account in the design of experiments testing lifetime multiplexed detection of different biological targets.

The Eu^{3+}-complexes can be loaded into cells by permeation/uptake[152–154] or immunoassay methods[132]. The former method is chosen for the present multiplexing experiments because

of the high level and consistency of uptake which can be achieved resulting in comparatively high brightness of the target cells.

Two cultured cell lines (prostate cancer cells DU-145 and bladder cancer cells C3) stained variously with three Eu^{3+} chelates by way of the permeation method are used to demonstrate lifetime-based detection and discrimination of the different cells by TRMFC as described in this chapter. One of the key issues encountered in these experiments is the stability of the luminescence lifetime for the stained cells because changes in the cell environment, chelation solvents or ratio of Eu^{3+} to chelators can result in a range of lifetimes presenting for notionally the same cells. Following careful selection and quantification of reactants and by optimizing the cell staining process, experimental protocols can be established whereby repeatability and stability of lifetime can be achieved.

5.2 Lifetime-Based Multiplexed Bioassay

As noted above luminescence response (wavelength, intensity and lifetime) of stained cells depends on how the lanthanide complex probes permeate different cell types (e.g., uptake by positive diffusion or endocytosis), and the nature of sub-cellular localisation (e.g., lysosomes, mitochondria or nuclear). As lanthanide complex molecules are quite sensitive to the intracellular environment, any local perturbation of pH, metal ions and oxyanions in cells can change the luminescence characteristics.

In the present experiments a multiplexed bioassay is undertaken using the time resolved microfluidic flow cytometer to analyse populations of two different cell lines stained by three different lanthanide complexes thus establishing 6 distinct populations with different lifetimes T and/or intensities A, which are then analysed by way of samples with mixed cell populations, as illustrated in Fig. 5-1. The three lanthanide complexes are obtained by adding europium chloride ($EuCl_3$) to three tetradentate β-diketonate chelators (BHHCT, BHHBCB and CDHH) in predetermined concentration ratios. The chelators were provided by Dr. Nima Sayyadi of Department of Molecular Sciences, Faculty of Science and Engineering, Macquarie University. Two of the chelators are then selected according to the luminescent lifetime/intensity of two cell lines after uptake by permeation.
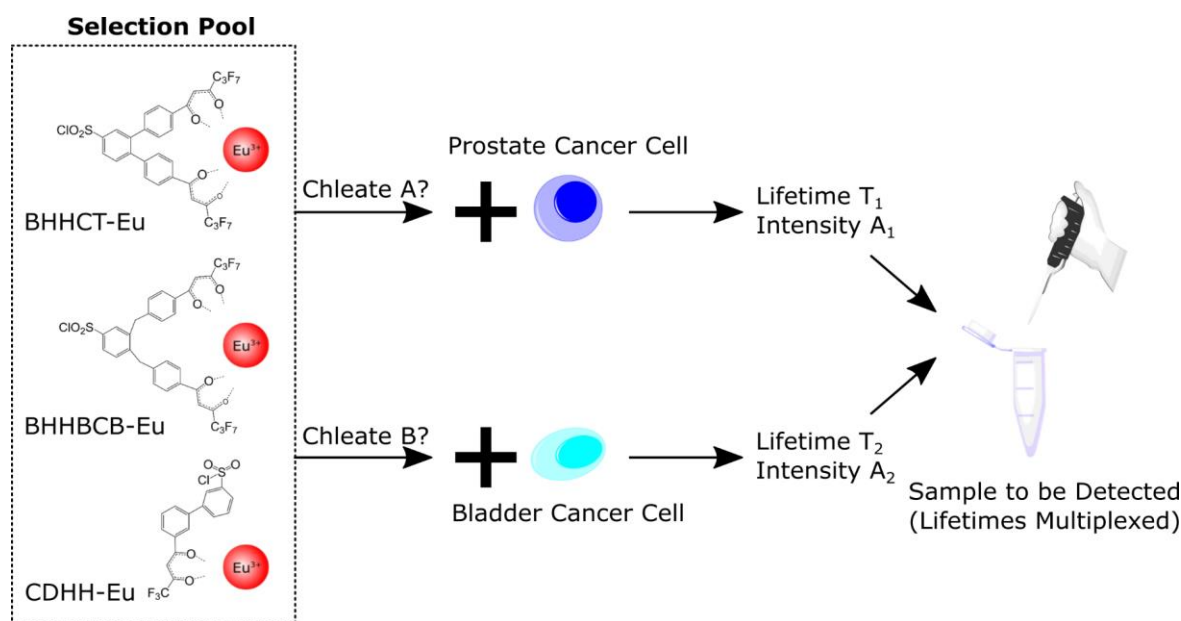
Figure 5-1 Model of lifetime-multiplexing detection panel containing prostate cancer cell/ bladder cancer cell, which are stained with Eu chelates.

The two cell lines used in the experiments are a human prostate cancer cell line DU-145 (American Type Culture Collection; ATCC; HTB-81) and a bladder cancer cell line C3 (the latter supplied by Prof. P Russell, Queensland University of Technology, Queensland, Australia). These two cell lines were cultured in 75 cm^2 culture flasks (T75) at 37 °C, in a humidified atmosphere with 5% (v/v) CO_2. They were incubated in RPMI 1640 (Life Technologies Australia Pty Ltd) supplemented with 10% (v/v) Fetal Calf Serum (FBS, Life Technologies Australia Pty Ltd), 50 IU/mL penicillin, and 50 μg/mL streptomycin. Cells were grown to near confluence in the culture flasks and then suspended with 0.05% (v/v) trypsin–EDTA solution (Life Technologies Australia Pty Ltd).

The structures of the selected chelators (BHHCT, BHHBCB and CDHH) are presented in Fig. 5-2. These are dissolvable in organic solvents, e.g., acetonitrile (ACN), dimethylformamide (DMF) and dimethyl sulfoxide (DMSO). The ligands can capture Eu^{3+} ions to form chelates (chelation process), which are quite stable with significant emission intensity and long lifetime values in range of microseconds to milliseconds, when excited with UV-vis light (excitation and emission maxima are 335 and 615 nm, respectively).
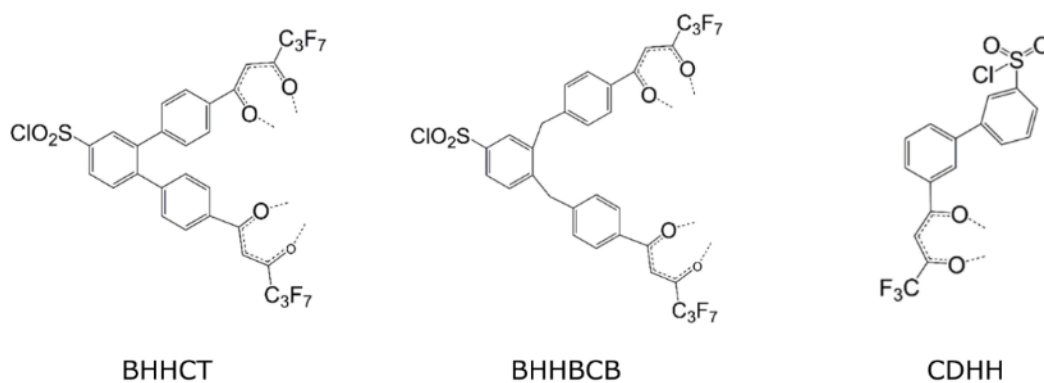
Figure 5-2 Three different structures of tetradentate β-diketonate-europium chelators used in the experiments.

The protocol for uptake of chelates into cells briefly contains two steps, first incubating the chelators to permeate cells and then completing the chelation process by adding Eu^{3+} in the form of $EuCl_3$ to the cell suspension. Note that we do not incubate cells with the Eu-chelates directly because they are easily aggregated as clusters in the solution, making it difficult to penetrate through uptake pathways of cell membranes.

To demonstrate reliable multiplexed detection in the time-resolved microfluidic flow cytometry, it is critical to explore and characterise the various factors that can affect the lifetimes or intensities of the chelates as probes for cells. In the following sections, the effect on the lifetimes and intensities of Eu-chelate stained cells is examined for different cell lines, cell growth phases, fixation of cells, chelate structures, ratio of chelators and Eu^{3+}, and reaction solvents for the chelates. Note that the intensity is quantified by peak signal voltage in the detected signal train.

5.3 Factors Affecting the Luminescence of Cells

When analysing a given experimental factor or variable influencing the luminescence lifetime or intensity of the Eu-chelate stained cells, all other variables are maintained constant. The detailed experiment conditions will be described separately in each sub-section below.

5.3.1 Cell Lines

The microenvironment of different cell lines can vary significantly. In order to see whether the key luminescence properties of uptaken chelates are different for different cell lines,

experiments were conducted with living DU-145 prostate cancer and C3 bladder cancer cell lines stained with Eu-BHHCT and Eu-BHHBCB. The ratio of chelators and Eu ions was set at 1:1, and the staining process was the same for all the experiments. However, when measuring the intensity of the stained cells in the time-resolved microfluidic flow cytometer, amplifier gain was set at 10^4 for the DU-145 cells, but was set at 10^5 for the C3 cells. This was because C3 cells, diameter typically 5-10 µm, are smaller than DU-145 cells (diameter typically 10-15 µm) thus individual DU-145 cells uptake greater amounts of chelate, i.e., twice of size resulting in around 8-fold volume difference, increasing the peak detected intensity accordingly. The lifetime and intensity distributions for the two cell lines as stained by the two chelates are shown in Fig. 5-3 (Eu-BHHCT) and Fig. 5-4 (Eu-BHHBCB), and CV of the distributions are listed in Tab. 5-1.
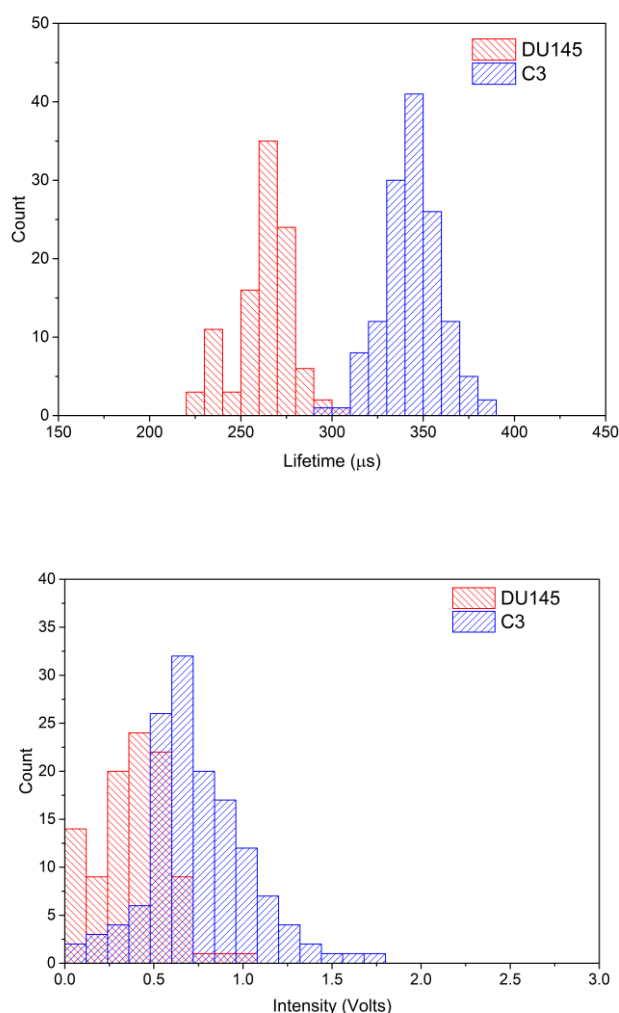
Figure 5-3 Lifetime and intensity distribution of DU-145 and C3 cells when stained with Eu-BHHCT chelate.
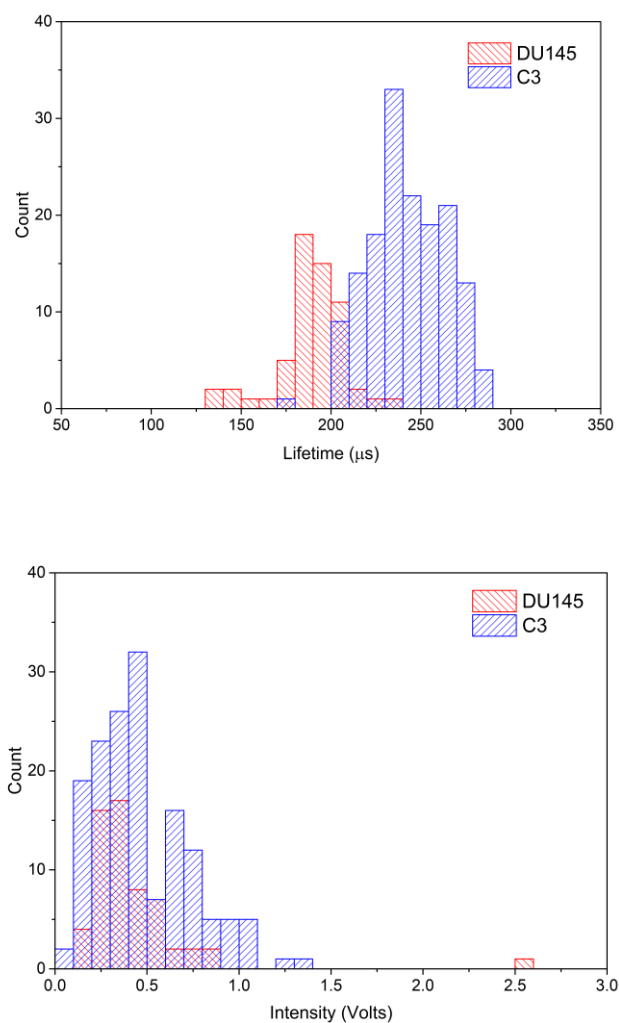
Figure 5-4 Lifetime and intensity distribution of DU-145 and C3 cells when stained with Eu-BHHBCB chelate.

Table 5-1 Data for lifetime and intensity distribution in Fig. 5-3 and Fig. 5-4.

	Eu-BHHCT (Fig. 5-3)		Eu-BHHBCB (Fig. 5-4)	
	DU-145	**C3**	**DU-145**	**C3**
Counts	101	138	59	154
Lifetime Ave. (μs)	263	344	189	242
Lif. CV	5.9%	4.5%	9.6%	8.7%
Intensity Ave. (Volts)	0.4	0.8	0.4	0.5
Int. CV	51.6%	38.3%	78.0%	54.2%

From the lifetime detection results in Fig. 5-3 and Fig. 5-4, we found both the chelate Eu-BHHCT and Eu-BHHBCB stained DU-145 and C3 cell lines demonstrated different luminescence lifetimes, with a small overlap in lifetime in the case of Eu-BHHBCB staining as shown by the data in Fig. 5-4. These results demonstrate that the same chelates up-taken

by different cell lines generally have different luminescent lifetimes, DU145 lifetimes typically shorter than those for C3.

The intensity data show that the two cell lines behave very similarly for staining with the two chelates, however, a different amplifier gain was used for the two cell lines: the stained DU-145 cells are clearly more intense, typically by a factor of 10, than the stained C3 cells. We believe that this results primarily from the larger size of the DU-145 prostate cancer cells and the correspondingly greater capacity to accept more chelate. Although the lifetimes are generally shorter for the brighter stained DU145 cells, we believe this is primarily the result of localised quenching of the Eu emission in the cells rather than a direct correlation between intensity and lifetime (for example we see that lifetime is also affected by cell growth phase as discussed below).

5.3.2 Cell Growth Phase

Stained cells of the same cell line but from different cell growth passages (including different cell growth phases) may also demonstrate different luminescence characteristics, particularly the value of the luminescence lifetime and the observed intensity. The duration between successive cell passaging varies inversely proportional to the rate of cell growth. DU-145 grows more rapidly than C3 cells, DU-145 cells passaging every 3-4 days, whereas C3 passage each 6-7 days. We stained Eu-BHHCT in two successive passages of DU-145 cells (passage P*m* and P*(m+1)*), and C3 cells (passage P*n* and P*(n+1)*). The solvent for BHHCT was DMF and chelation ratio of BHHCT to Eu ion concentration was maintained at 1:1. Note that the cell samples were extracted near the end of each growth passage, where the predominant growth phase is expected to be G2+M (pre-division growth plus mytosis) but there is likely to be a spectrum of growth phases present in the samples. The experimental data for lifetime and intensity are shown in Fig. 5-5 (DU-145) and Fig. 5-6 (C3), and summarised values in Tab. 5-2.
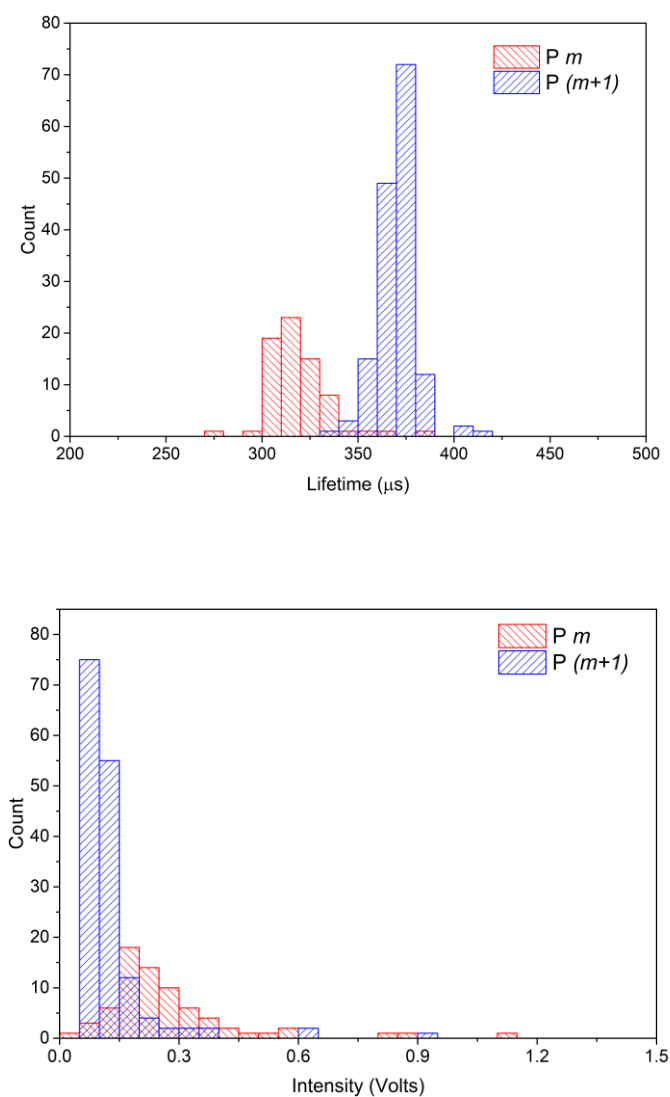
Figure 5-5 Lifetime and intensity distribution of Eu-BHHCT chelate stained DU-145 cells for two successive growth passages.
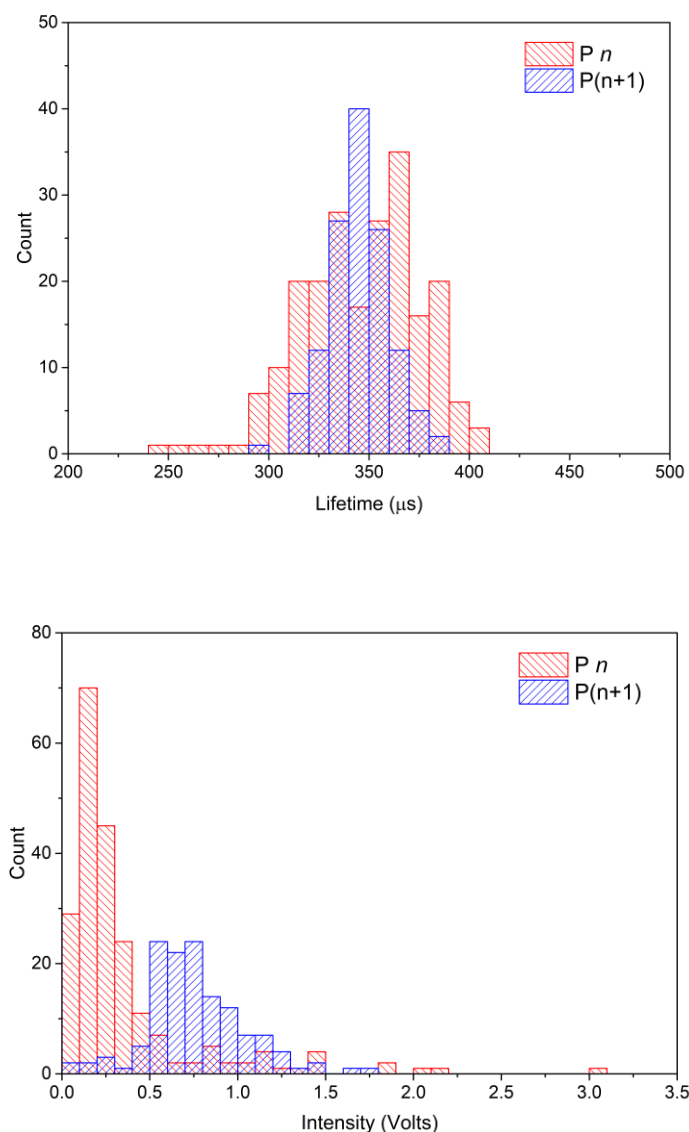
Figure 5-6 Lifetime and intensity distribution of Eu-BHHCT chelate stained C3 cells of two successive growth passages.

Table 5-2 Summary of lifetime and intensity distribution for data shown in Fig. 5-5 and Fig. 5-6.

Eu-BHHCT	DU-145 (Fig. 5-5)		C3 (Fig. 5-6)	
	P m	**P $(m+1)$**	**P n**	**P $(n+1)$**
Counts	71	155	214	132
Lifetime Ave. (μs)	319	370	346	345
Lif. CV	5.0%	2.8%	8.6%	4.4%
Intensity Ave. (Volts)	0.3	0.1	0.4	0.8
Int. CV	65.7%	81.2%	118.3%	37.5%

The change in luminescence lifetime is quite large for DU-145 but small for C3 between two cell growth passages. The intensity, mean values show a shift for both cells between successive passages. This indicates that the luminescent characteristics, known to reflect the microenvironment inside the cells, can be quite unstable from passage to passage, and potentially growth phase to growth phase. This probably results from variations in pH, oxygen level or other metabolism processes between growth passages since the chelates are quite sensitive to these factors. It is certainly noteworthy that cell growth phase, or different growth passage may also affect observed lifetime and intensity of Eu-chelate stained cells.

5.3.3 Cell Fixation

Normally, when labelling cells by immunoassay methods with antibodies, the cells are initially fixed to preserve the structures of antigens on the membranes so as to achieve higher labelling efficiency. In the present experiments, the chelators and $EuCl_3$ enter the cells by an uptake process, via pathways of passive diffusion or endocytosis.[162] The experiments in Chapter 5.3.1 and 5.3.2 were all conducted with living cells. It is important therefore, to determine whether fixation affects uptake of chelates into cells and if it changes the luminescence emission decay time (i.e., lifetime) of the intracellular chelates, and the observed intensities (i.e., intensity/brightness) of stained cells.

To compare the luminescent output of the chelates stained cells upon fixation factor only, DU-145 cells of the same passage and extracted from the same culture flask, were separated into three equal groups, I, II and III. The cells were all stained with Eu-BHHBCB, but cells in I were stained directly with no fixation, II was stained after fixation with 4% (v/v) paraformaldehyde (PFA) for 15 mins, and vice versa for group III. The cells were washed twice with PBS and stored at 4 °C until being processed for the next procedure after fixation. The solvent for the chelator BHHBCB was DMF for all three groups and chelation ratio of BHHBCB to Eu ions was set at 1:1. The luminescence intensity and lifetime distribution of stained cells in the three groups are shown in Fig. 5-7, and related data are listed in Tab. 5-3.
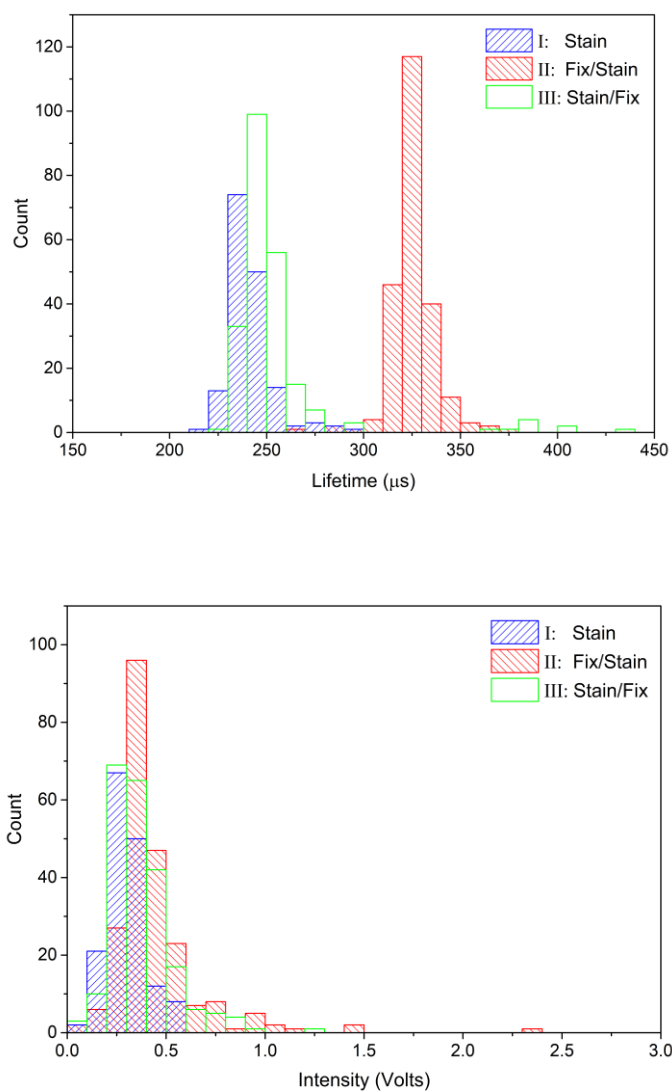
Figure 5-7 Lifetime and intensity distribution of Eu-BHHBCB stained DU-145 (upper chart) and C3 cells (lower chart) under different fixation conditions.

Table 5-3 Data for three groups of stained DU-145 cells under different fixation conditions.

DU-145 / Eu-BHHBCB	I Stain	II Fix/Stain	III Stain/Fix
Counts	160	228	223
Lifetime Ave. (µs)	241	325	255
Lif. CV	4.8%	3.5%	11.7%
Intensity Ave. (Volts)	0.3	0.4	0.4
Int. CV	32.7%	53.6%	41.9%

As can be seen from the data of Fig. 5-7, luminescence intensities for the three groups are quite similar from which it can be concluded that fixed or not, and fixed before or after

staining does not result in significant differences in chelate uptake. However, fixation affects luminescence lifetime of Eu-chelate stained cells when fixation precedes staining (group II), whereas for groups I (stain with no fixation) and III (stain before fixing lifetime distributions are essentially identical.

Given that the emission properties of up-taken chelates are sensitive to the inter/intra-cellular environment, it is preferable to stain cells with no fixation to maintain the original properties of target cells, however for the purpose of lifetime-multiplexed bioassays (consistent with the direction of the current research), cell fixation ahead of staining results in a distinctly narrower lifetime distribution (as shown in Tab. 5-3). Note that fixation and staining of both cell lines was performed in air to ensure the oxygen level is the same for all experiments. Oxygen level is one of several factors that can affect the luminescence lifetime of the stained cells, but study of this is beyond the scope of this thesis.

5.4 Properties of Chelates Affect in Luminescence Characteristics

The properties of the Eu-chelates used here that may affect the luminescence emission characteristics for the stained cells include the specific chelate structures, the chelation ratio of ligands and central ions, and the solvent used for the chelators. These factors are analysed in the following section.

The three chelators, BHHCT, BHHBCB and CDHH were dissolved in ACN, DMF and DMSO at the same molar concentration, resulting in nine combinations of chelator and solvent. The luminescence lifetime for each these nine chelate solutions were measured for chelate-Eu^{3+} ratio varied by stepwise titration of chelators with $EuCl_3$ solution. Luminescence characteristics for a range of chelation ratios were mapped for each of these nine combinations.

5.4.1 Measurement Platform

The lifetimes of the different Eu-chelate combinations were measured using a Cary Eclipse Fluorescence Spectrophotometer in the time-resolved detection mode (Fig. 5.8).

Prior to the measurement, the gate time and delay time can be set via a software interface according to the estimated lifetimes of samples. For the measurements of the Eu-chelate lifetimes in this section, we set the delay time as 100 µs and the gate open (detection) time was 1000 µs.
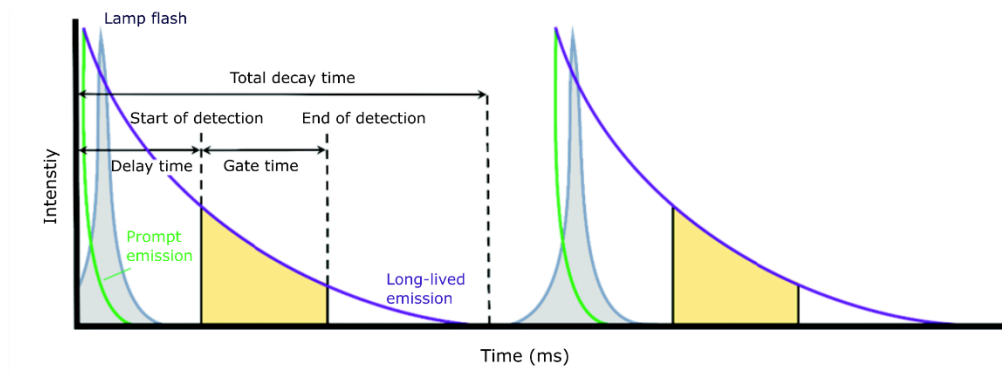
Figure 5-8 The time-resolved measurement scheme for Cary Eclipse Fluorescence Spectrophotometer by Agilent Technologies.

5.4.2 Measurement Procedure

There were nine sets of samples for permutations of three chelators dissolved in three organic solvents respectively. The samples were contained in a cuvette of standard dimensions. For each solution of chelator, $EuCl_3$ concentration was varied to give nine ratios of chelator: Eu, ranging from 10:1 to 1:10. The molar concentrations of the nine chelator solutions were set at 10^{-8} mol/µl (10 mM) to provide easy comparison between the nine combinations as listed below in Tab. 5-4.

Table 5-4 Preparation of chelator solutions.

Chelator	Molar Mass	Weight	Molar	Solvent		
	mg/mol	mg	mol	ACN	DMF	DMSO
BHHCT	0.79	0.8	10^{-6}	100 µl	100 µl	100 µl
BHHBCB	0.81	0.8	10^{-6}	100 µl	100 µl	100 µl
CDHH	0.46	0.9	2×10^{-6}	200 µl	200 µl	200 µl

The $EuCl_3$ solution was prepared in two different concentrations, 10 mM and 1M respectively as shown in Tab 5-5, to adjust the ratio of chelator and Eu^{3+} ion concentrations in the chelating reactions. The 1M solution was used in the case of high Eu^{3+} ratios to avoid

introducing excess water to the organic solvents in the reactions, and to avoid any effects of change of solvents on luminescence emission.

Table 5-5 EuCl$_3$ solution preparation in two molar concentrations.

Concentration	EuCl$_3$ (mg)	Molar	MiliQ water
10 mM	3	0.0116 mMol	1160 µl
1 M	30	0.1160 mMol	116 µl

5.4.3 Results and Analysis

The values of measured lifetimes are listed in Tab. 5-6, and are plotted in the following Fig. 5-9.

Table 5-6 Lifetimes (µs) of chelates dissolved in three solvents at different chelating ratios.

Molar concentration		EuCl$_3$ solution							
		10 mM					1 M		
EuCl$_3$ Volume (µl)		10	15	25	25	25	1	2	4	2
Chelator: Eu^{3+}		10:1	4:1	2:1	4:3	1:1	1:2	1:4	1:8	1:10
	ACN	4	242	256	265	267	261	254	246	245
BHHCT	DMF	587	548	507	475	452	444	433	414	403
	DMSO	655	677	673	657	634	641	647	651	651
	ACN	13	132	192	214	220	211	204	200	199
BHHBCB	DMF	397	436	410	382	363	357	342	315	308
	DMSO	489	556	555	537	524	558	560	593	578
	ACN	NA	52	145	146	149	142	142	139	138
CDHH	DMF	359	361	338	318	304	302	302	291	287
	DMSO	709	683	672	645	608	626	628	632	638
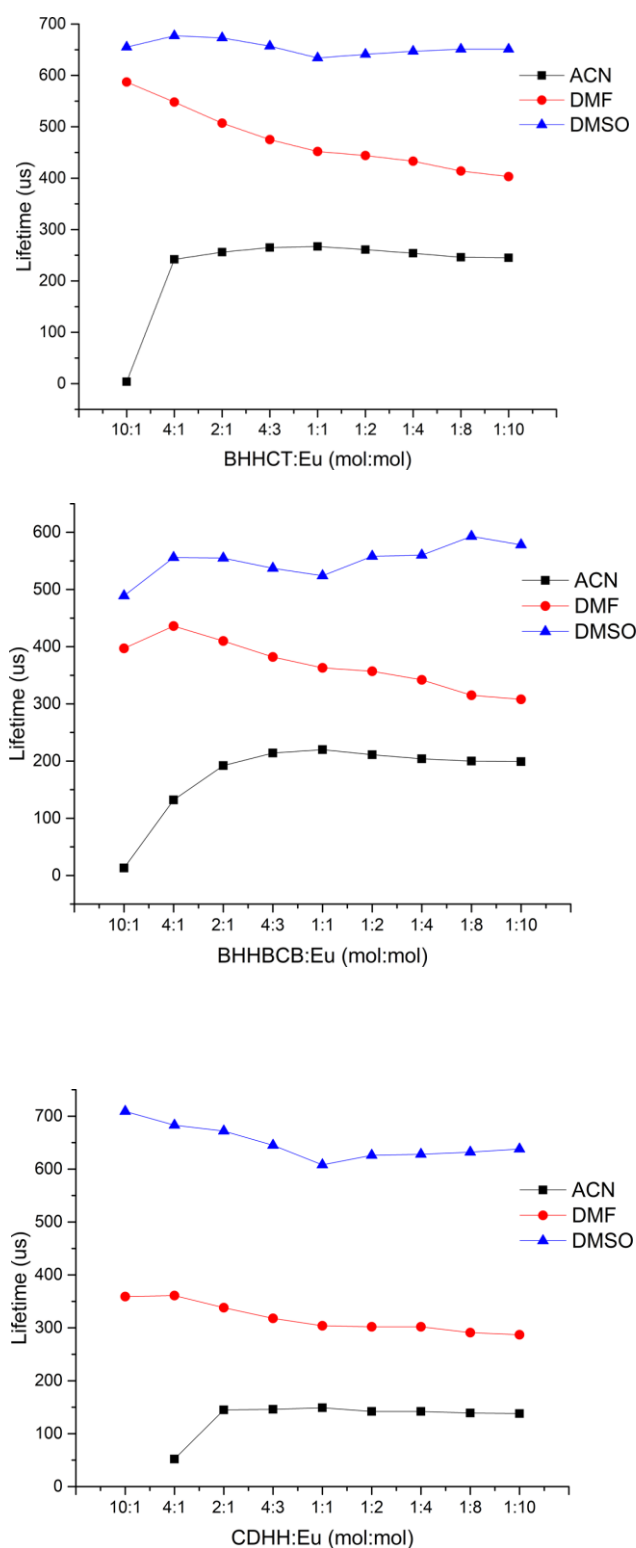
Figure 5-9 Lifetimes of three Eu chelates (BHHCT, BHHBCB and CDHH) in three solvents (ACN, DMF and DMSO) changed towards chelation ratios of chelator to Eu^{3+}.

It is clear from the above data that the same type of Eu-chelate dissolved in different solvents results in significant change to the luminescent lifetime, observed for all the three chelates. Eu-chelates dissolved in DMSO have the longest luminescence lifetime of more

than 500 µs, whereas for the ACN solvent lifetimes are the shortest, less than 300 µs. For increase in ratio of Eu^{3+} to chelator, lifetimes for solution in ACN increase initially and reach to a stable value in the range 150 µs to 250 µ above a ratio of about 2:1. For the Eu-chelates in DMF, lifetimes decrease monotonically as the ratio is increased. In contrast, for DMSO as the solvent, the lifetime values were comparatively stable across the full range of chelate-Eu^{3+} ratios, especially above 1:1 where lifetimes fall in a narrow region 550 µs-650 µs for all three solvents. It is noted finally that excess Eu^{3+} appeared to have little effect on observed lifetimes.

5.4.4 Choice of Chelator Solvent

In consideration of the preceding results, DMSO was chosen as the chelator solvent for all subsequent experiments. The key reasons for this selection are listed below:

i. The lifetimes of each single chelate dissolved in DMSO are quite stable in a 500-700 µs range (Fig. 5-9), relatively insensitive to the chelation ratio.

ii. Use of DMSO as the chelator solvent results in longer chelate-Eu^{3+} luminescence lifetimes, providing greater flexibility in lifetime range for multiplexing in cell experiments.

iii. DMSO is commonly used as a solvent for biosamples, i.e., cells or tissues.

iv. Chelates are easily soluble in DMSO and it has low toxicity (though attention must still be paid when handling DMSO since it penetrates easily through skin, so that gloves are required for handling).

The lifetimes of the three Eu-chelates dissolved in DMSO are collated in Fig. 5-10 below.
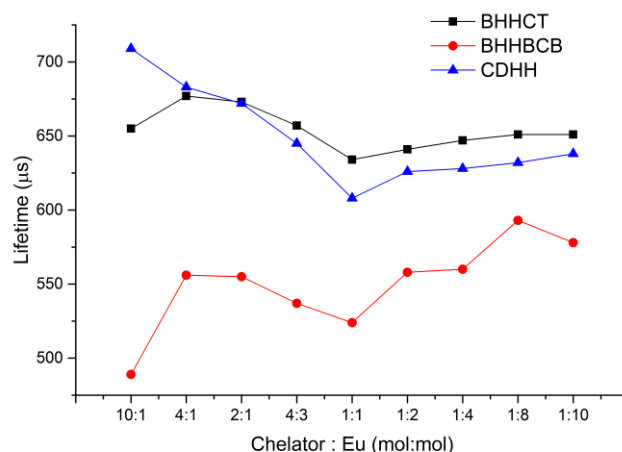
Figure 5-10 Lifetimes of three Eu-chelates in DMSO solution.

Luminescence lifetimes for DMSO solvent for Eu-BHHCT and Eu-CDHH lie in range from 600 µs to 700 µs, whereas for Eu-BHHBCB is between 500 µs and 600 µs. Above a chelation ratio of 1:1, the lifetimes of BHHCT and CDHH are quite stable in a 50 µs range, from 600 µs to 650 µs. Though the luminescence of Eu-BHHBCB was observed to have stronger dependence on chelate-Eu concentration ratio than Eu-BHHCT and Eu-CDHH, the variation remained in a comparatively small range ~75 µs. Choosing chelation ratio close to 1:1 minimises the variation of lifetime for DMSO solvent, this condition being adopted for all subsequent cell staining experiments.

As for selecting the two preferred chelates for staining the two cell lines for lifetime-multiplexed detection, this requires that the two chelates chosen have clearly distinguishable lifetimes, as discussed below.

5.5 Lifetime-Multiplexed Detection of Two Different Cell Lines in TRMFC

As described earlier, our aim is to demonstrate a lifetime-multiplexed bioassay by time-resolved microfluidic flow cytometry of a sample containing two different two cell lines (DU-145 and C3), each coded with distinct luminescence lifetimes by way of uptake-staining of the two cell lines by Eu-chelates with different characteristic lifetimes. It has been shown in the previous sections 5.3 and 5.4 that the luminescence output of lanthanide complexes is quite sensitive to their environment including any changes to the chelation reaction protocols

themselves. Subsequent analysis of a number of factors which can significantly change the emission characteristics of the stained cells has identified a set of conditions which decrease the variability in luminescence intensity and lifetime, notably fixing the cells before staining, using DMSO as the chelator solvent, and choosing Eu^{3+}: ligand molar ratios at 1:1 or above for the chelation reaction in the cells.

In this section, the two cell lines are stained with the three chosen lanthanide complexes using an optimised staining protocol based on the above conditions. The luminescence lifetimes and intensities of these Eu-chelate stained cells are then measured separately by the time-resolved microfluidic flow cytometer to select operating conditions for subsequent lifetime-multiplexed analysis of a mixed cell sample.

5.5.1 Optimised Cell Staining Protocol

After analysing the factors that can affect the lifetimes and intensities of stained cells, an optimised protocol for staining of cells with luminescent Eu-chelates has been developed as summarised below:

1. Freshly passaged well-suspended DU-145 cells (10^7/ml, PBS solution) are added into three 1.5 ml polystyrene tubes, A1, A2 and A3, evenly (1 ml each), C3 cells (about 10^7/ml, PBS solution) into tubes B1, B2 and B3 evenly (1 ml each).

2. Centrifuge (300 rcf, 5 min) six tubes and remove the supernatant. Then resuspend the cells in 300 µl 4% (v/v) PFA and leave the tubes for overnight for sufficient fixation of cells.

3. Repeat centrifugation (300 rcf, 5 min) two times to purify and isolate the cells from PFA solution by removing the supernatant and resuspending fixed cells into 200 µl PBS.

4. Add 100 µl DMSO solution of three chelators, BHHCT, BHHBCB and CDHH (10 mM, overdosed to fully stain all the cells) in A1, A2, A3 and B1, B2, B3 respectively as shown in Tab. 5-7. Mix the chelators and the cells well in the tubes with pipette.

Table 5-7 Chelators and cell lines in each tube.

	A1	**A2**	**A3**	**B1**	**B2**	**B3**
Cell line	DU-145	DU-145	DU-145	C3	C3	C3
Chelator	BHHCT	BHHBCB	CDHH	BHHCT	BHHBCB	CDHH

5. Centrifuge six tubes at 300 rcf for 5 min and remove the supernatant and resuspend the cells in 200 µl DMSO and 800 µl PBS. Centrifuge tubes (300 rcf, 5 min) to wash the excess chelators in the solution. Repeat washing for two more times by centrifuging after adding 100 µl DMSO and 900 µl PBS in the tubes to make sure there is no excess chelators. This step is critical because the overdosed chelators need to be washed off to make sure the luminescence background in the solution are as low as possible.

6. Add 200 µl $EuCl_3$ solution (10 mM) into each tube and mix well, now the cells are stained with Eu-chelates.

7. Add 1 ml MiliQ water into six tubes and centrifuge to remove the supernatant and repeat one more centrifuge to wash off the excess Eu^{3+}.

8. Resuspend the cells into 200 µl AutoMacs solution (Miltenyi Biotec, aiming to prevent cells aggregation).

9. Accurately quantify cell concentration by conventional flow cytometry (BD Influx cell sorter, BD Bioscience).

10. Restore the tubes in fridge (4°C) for time-resolved measurements.

5.5.2 Cell Lifetime Calibration

The chelates stained DU-145 (tube A1-A3) and C3 (tube B1-B3) cells were analysed separately by time-resolved microfluidic flow cytometry for measurement of luminescence lifetime and intensity distributions. Results are shown in Fig. 5-11 and Tab. 5-8. Note that amplifier gain was set at 10^5 for the tube B3 cell sample (C3/Eu-CDHH), otherwise 10^4 was the default setting for amplifier gain for other samples.
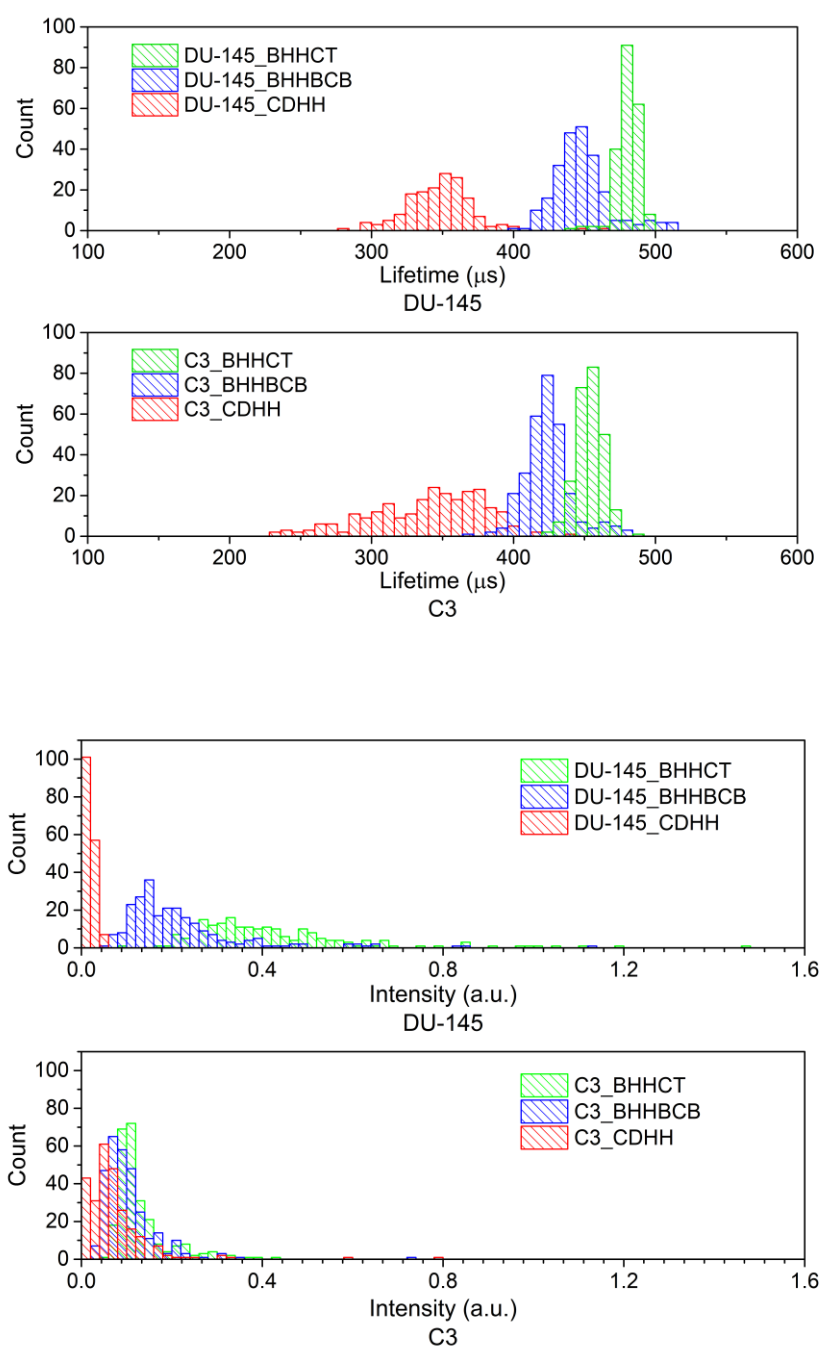
Figure 5-11 Lifetime and intensity distributions of two cell lines stained with three different chelates, measured using time-resolved microfluidic flow cytometer.

Table 5-8 Calculated results of average lifetime, average intensity, CV and cell count in Fig. 5-11.

	A1	A2	A3	B1	B2	B3[*]
Cell line	DU-145	DU-145	DU-145	C3	C3	C3
Chelator	BHHCT	BHHBCB	CDHH	BHHCT	BHHBCB	CDHH
Lifetime ave.	481 µs	448 µs	348 µs	454 µs	424 µs	340 µs
Lifetime CV	1.7%	4.4%	7.0%	2.1%	3.9%	11.9%
Intensity ave.	0.44 a.u.	0.22 a.u.	0.02 a.u.	0.13 a.u.	0.10 a.u.	0.07 a.u.
Intensity CV	57.1%	64.3%	34.5%	47.0%	61.6%	105.8%
Counts	208	241	165	256	299	254

* Amplifier gain $\times 10^5$ was applied, otherwise $\times 10^4$ was the default amplifier gain setting.

For the lifetime distributions in Fig. 5-11, the same cell line stained with three chelates showed very different lifetime ranges, consistent with previous experiments. However, when the same chelate is used to stain different cell lines, the luminescence lifetimes are quite similar, within 5.6%.

Considering the intensity histograms in Fig. 5-11, the luminescence intensity of Eu-BHHCT stained cells is observed to be similar to that of Eu-BHHBCB cell. The stained DU-145 cells are more intense than the stained C3 cells for both chelates, primarily because DU-145 cells are larger and therefore capable of uptaking more chelate. However, the Eu-CDHH stained cells are quite faint compared to the intensities seen for the other two chelates. This can be attributed to the structure of CDHH (Fig. 5-2) which can provide only half of the energy pathway from the chelate antenna to the bound Eu^{3+} ion as compared to BHHCT and BHHBCB.

To prepare for lifetime-multiplexed detection by TRMFC, one population of Eu-chelate stained DU-145 cells and another of Eu-chelate stained C3 cells with distinct lifetime ranges must be selected. According to the lifetime results shown in Fig. 5-11 and Tab. 5-8, DU-145 stained with Eu-BHHCT (A1) and C3 stained with Eu-CDHH (B3) were chosen for the subsequent multiplexing demonstration. Note that the difference of their intensities can also be used to separate the different cell populations in a two-dimensional representation of the data (see the intensity difference in Fig. 5-12).

Fig. 5-12 shows images of DU-145 stained with Eu-BHHCT and C3 cells with Eu-CDHH respectively in bright field and under UV excitation. Inspection of the images shows that the typical size of DU-145 cells is in the range 10-15 µm, larger than the C3 cells (5-10 µm). Here the UV-excited image of C3 was taken with 200 ms exposure time and the others were

with 20 ms. Even with 10-fold longer exposure time, C3 cells stained with Eu-CDHH are still much fainter than DU-145; this can be used to differentiate the cell populations together with lifetime.
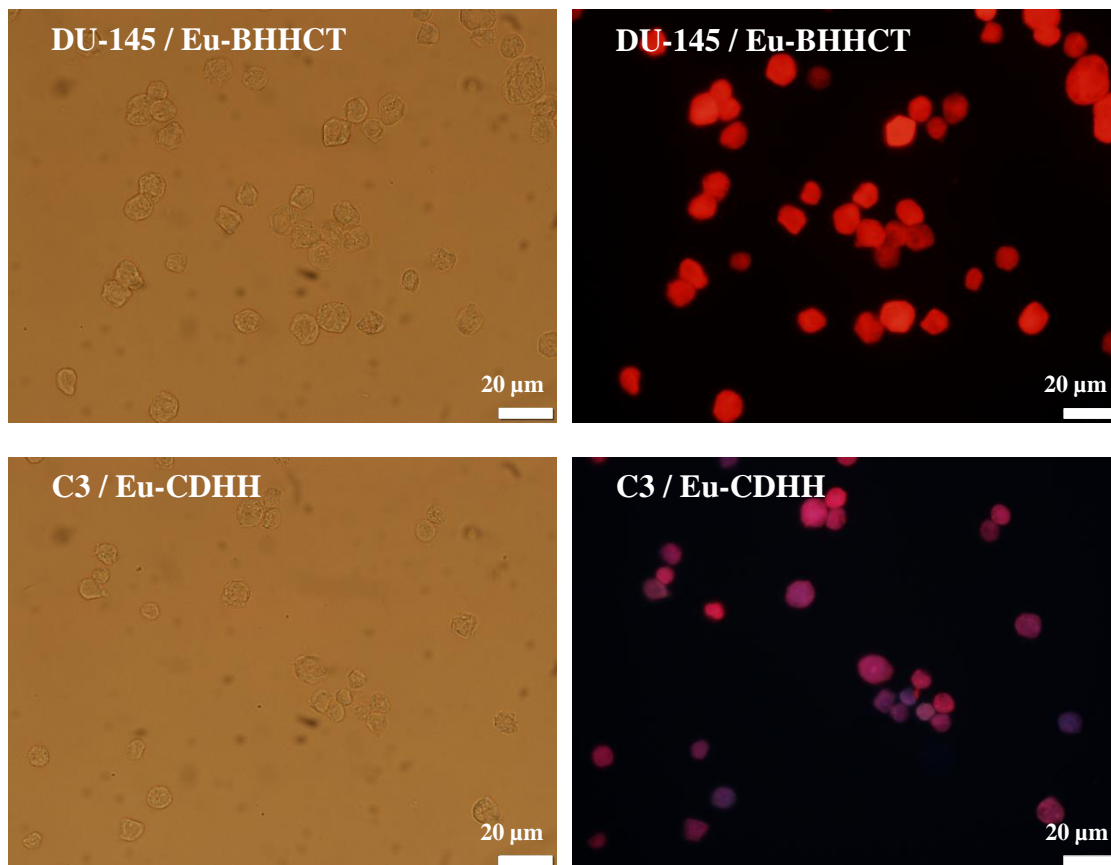
Figure 5-12 Bright field images and UV-excited images of DU-145 stained by Eu-BHHCT and C3 by Eu-CDHH. The exposure time for C3 cells under UV is 200 ms, and that for the other three images is only 20 ms.

To confirm that the luminescence output of the Eu-chelate stained cells can be adequately controlled, a second set of experiments exactly following the protocol described in Chapter 5.5.1 was undertaken with a successive passage of cells. DU-145 prostate cancer cells were stained with Eu-BHHCT and C3 bladder cancer cells with Eu-CDHH, and subjected to separate analysis by TRMFC: results are compared with those of the previous experiments (denoted as S1 here), as shown in Fig. 5-11 and Tab. 5-8 (A1 and B3). The results of two sets of experiments are consolidated in Fig. 5-13 and Tab. 5-9.
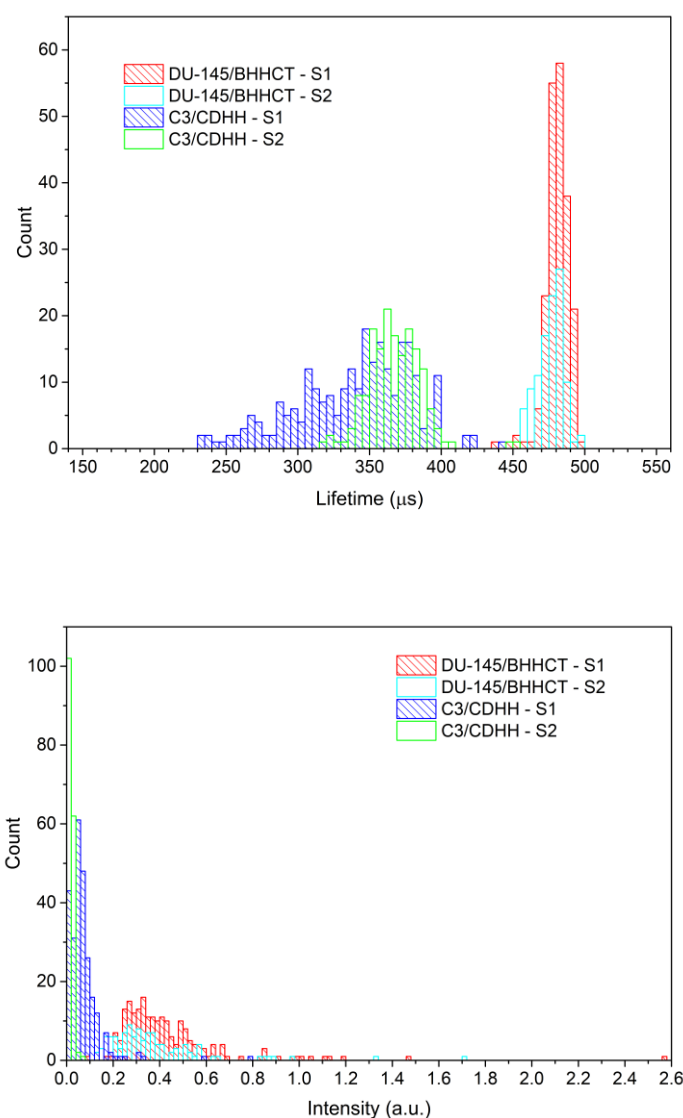
Figure 5-13 Lifetime and intensity distributions of two sets of experiments that DU-145 is stained with Eu-BHHCT and C3 with Eu-CDHH.

Table 5-9 Calculated results of average lifetime, average intensity, CV and cell count in Fig. 5-13.

Cell line	DU-145		C3	
Set of Experiment	S1	S2	S1[*]	S2
Chelator	BHHCT	BHHCT	CDHH	CDHH
Lifetime ave.	481 μs	475 μs	340 μs	368 μs
Lifetime CV	1.7%	2.0%	11.9%	5.2%
Intensity ave.	0.44 a.u.	0.37 a.u.	0.07 a.u.	0.02 a.u.
Intensity CV	57.1%	62.0%	105.8%	37.6%
Counts	208	109	254	167

* Amplifier gain ×10⁵ was applied, otherwise ×10⁴ was the default amplifier gain setting.

The lifetime distributions confirmed that cells for two sets of experiment (S1 and S2) stained with the same chelate have overlapping lifetime, so lifetime value is quite stable for the selected staining protocol. Since cells of two successive growth passages were used in S1 and S2 experiments, it is evident that measured lifetimes are not sensitive to different passages for the chosen conditions, which include cell fixation before staining. This comparison verified that fixation effectively permeabilizes the cells and universalizes the inter and intra-cellular environment.

Considering the intensity results, it is clear that the stained DU-145 cells were invariably brighter than the stained C3 cells for both sets of experiments S1 and S2. Notably for $x10^4$ amplifier gain set for the S2 detection runs for both C3 and DU-145 cells, the detected luminescence intensities are quite distinct as shown by the data of Fig. 5-14. So for the next section of multiplexing detection of the mixture samples of two cell lines, gain 10^4 of amplifier will be used and intensity and lifetime distributions will both be used for the separation of two different cell populations.
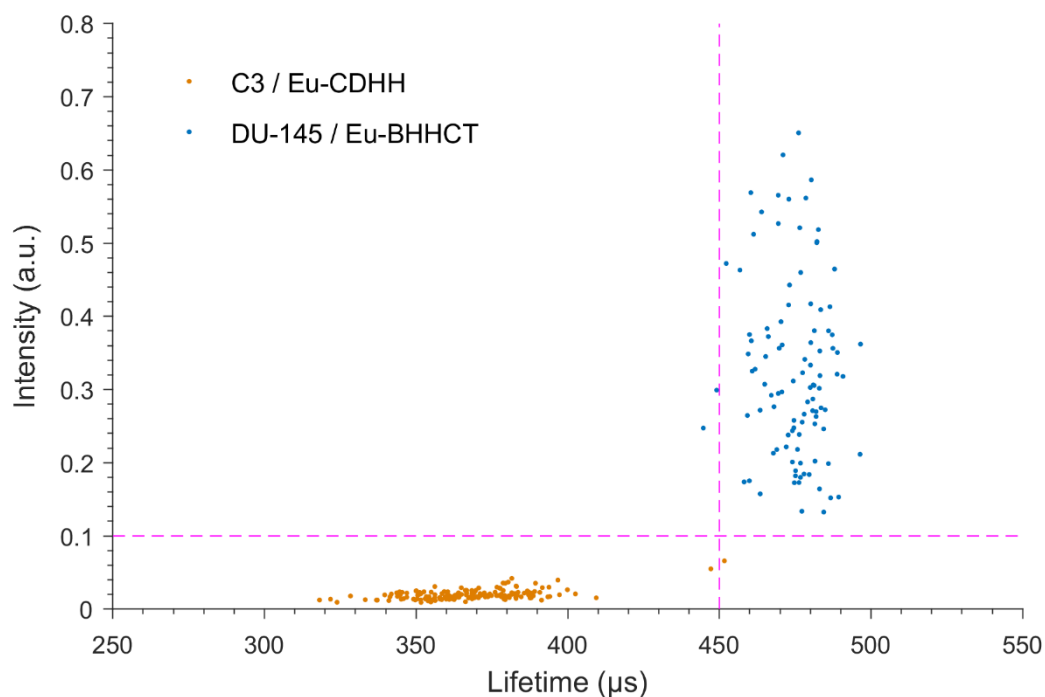
Figure 5-14 Scatter chart of luminescence intensity vs lifetime for DU-145 cells doped with Eu-BHHCT and C3 cells doped with Eu-CDH for S2 experiments. The data is the same as appears in the histograms of cell counts vs lifetime and intensity are shown in Fig. 5-13.

When recognising different cell populations in the mixed multiplexing samples, thresholds for lifetime and intensity should be applied for the separation of the cells. As shown in Fig. 5-14, measured lifetimes of C3 cells stained with Eu-CDHH lay in range of 230 µs to 460 µs, whereas DU-145 stained with Eu-BHHCT had measured lifetimes from 435 µs to 500 µs. There is a small range of overlap in lifetime distributions around 450 µs, but involving only a few cells. However, setting an empirical intensity boundary at 0.1 and lifetime boundary at 450 µs is easy to differentiate the two different cell populations with very few cell counts lost.

5.5.3 Multiplexing Detection on TRMFC

To demonstrate lifetime-based multiplexing detection by time-resolved microfluidic flow cytometry, a bioassay was designed comprising two cancer cell lines which were uptake-stained with different Eu chelates following the previously established optimised staining protocol. The two populations of stained cells will then be mixed in different ratios to provide calibrated samples for analysis by the TRMFC.

Original concentrations of the stained DU-145 and C3 cells were estimated as ~10^7 cells/ml according to Countess™ II FL Automated Cell Counter. More accurate measurements of concentrations were then made on a commercial flow cytometry (BD Influx cell sorter, BD Bioscience), showing the concentration of the prepared DU-145 suspension (×1 suspension) was $7.9{\times}10^6$ cells/ml with CV being 11.4% and that of the C3 (×1 suspension) is $1.1{\times}10^7$ cells/ml with CV of 5.1% (see in Tab. 5-10).

Table 5-10 Cell concentration counted on commercial flow cytometer.

Suspension	R1	R2	R3	Average	Uncertainty
DU-145(×1)	$8.9{\times}10^6$/ml	$7.5{\times}10^6$/ml	$7.3{\times}10^6$/ml	$7.9{\times}10^6$/ml	11.4%
DU-145(×500)	$2.1{\times}10^4$/ml	$2.1{\times}10^4$/ml	$1.2{\times}10^4$/ml	$1.8{\times}10^4$/ml	28.9%
C3 (×1)	$1.1{\times}10^7$/ml	$1.2{\times}10^7$/ml	$1.1{\times}10^7$/ml	$1.1{\times}10^7$/ml	5.1%
C3 (×500)	$2.9{\times}10^4$/ml	$2.4{\times}10^4$/ml	$2.7{\times}10^4$/ml	$2.6{\times}10^4$/ml	9.4%

Diluted cell suspensions were prepared to adjust the ratio of two cell populations. 2 µl of both original cell suspensions (original suspension, ×1 original) were diluted into 1 ml AutoMacs respectively to obtain a small number of cells (diluted suspension, ×500 diluted). The diluted suspensions of both cells were counted on the commercial flow cytometer,

giving concentrations of the ×500 diluted DU-145 as 1.8×10^4 cells/ml with CV of 28.9% and of the diluted C3 suspension as 2.6×10^4 cells/ml with CV of 9.4%.

Note that in the case of the diluted samples, the cell count numbers from which the concentrations are calculated are low, often only a few tens of cells for a given count run, so that there is a significant variation of calculated concentrations for nominally the same sample. It follows that the uncertainties in the cell concentration values as represented by the CV, are substantially higher (a factor 2 or more) for the ×500 diluted samples than for the ×1 samples, as illustrated by the values listed in Tab. 5-10.

For the purpose of demonstrating lifetime-multiplexed analysis by TRMFC, mixed samples containing both DU-145 and C3 cells (each population stained with the different Eu-chelates), were prepared in five relative concentrations (groups denoted as K1-K5), as listed in Tab. 5-11. In practice the volumes of the two cell populations (with ×1 suspension or ×500 suspension depending on the chosen cell concentrations) were spiked into 10 ml AutoMacs to make the K1-K5 sample groups. Note that cell numbers and relative concentrations for specific suspension are stated in a range owing to the uncertainty of cell counting data obtained by commercial flow cytometry (see Tab. 5-10).

Table 5-11 Preparation of mixtures of two cell populations, which were spiked in five different proportions.

Group	DU-145 / Eu-BHHCT			C3 / Eu-CDHH			Proportion
	×1	×500	Cell Num.	×1	×500	Cell Num.	
K1	1.5μl		11850±1350		15μl	400±38	36:1~24:1
K2	1.5μl		11850±1350		150μl	4000±380	3.6:1~2.4:1
K3	0.75μl		5925±675	0.75μl		8250±420	1:1.2~1:1.7
K4		150μl	2700±780	1.5μl		16500±840	1:4.5~1:9.0
K5		15 μl	270±78	1.5μl		16500±840	1:45~1:90

Each of the K1-K5 samples were then analysed on TRMFC in triplicate (denoted as M1, M2 and M3), each for a 20-minute run time at sample flow rate 0.01 ml/min (horizontal orientation of syringe pump). Note the cell samples were well mixed prior to analysis, however cell aggregation and settling to the bottom of the syringe vessel was significant during the experimental run time. The measured lifetimes and intensities of detected events were recorded and plotted intensity vs lifetime: data for the particular case of the K3 samples where the calibrated cell numbers are 5925 ±675 and 8250 ±420 for DU145 and C3 cells respectively (i.e. approximately equal cell numbers), are shown in Fig. 5-15.
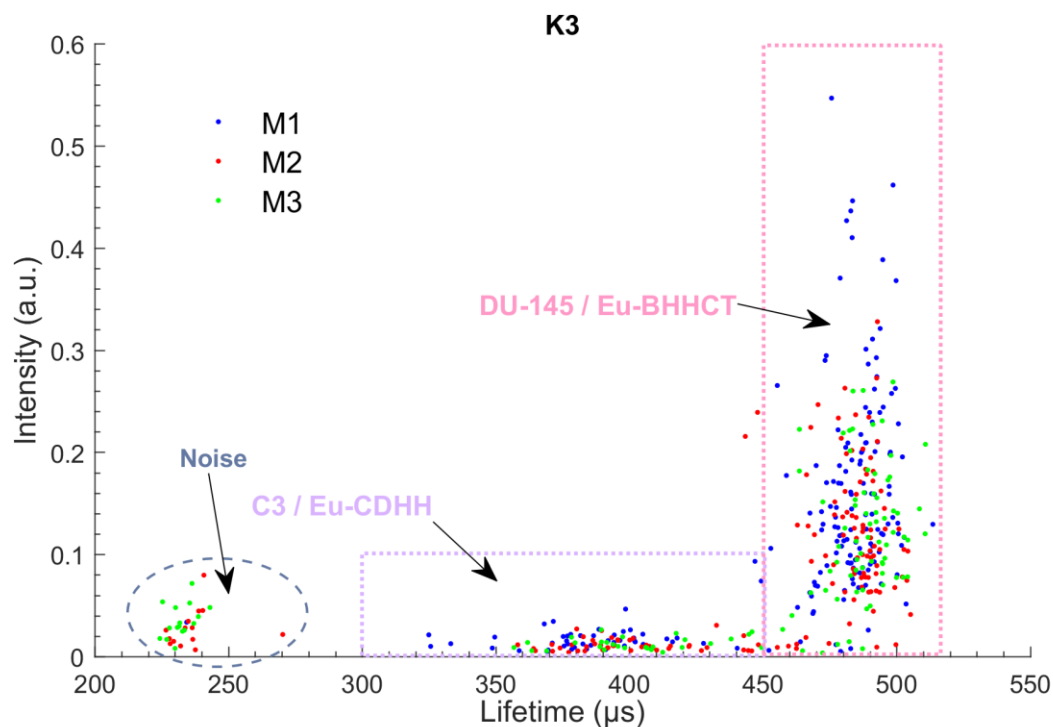
Figure 5-15 Scatter of detected events of M1-M3 in K3 mixed samples on the coordinate system where lifetime is on the X and intensity on the Y axes. Two populations of cells can be differentiated based on the selected boundaries according to the measured lifetime and intensity.

The lifetime ranges of most of the detected events shown in Fig. 5-15 are similar compared to those presented in Fig. 5-13 and 5-14, though some events also appear with low intensities at lifetimes closely grouped around 230 µs (labelled "Noise" in Fig. 5-15). This latter group of events is also seen in analysis of K1, K2, K4 and K5 samples, and is tentatively identified as arising from suspended Eu-chelate aggregates outside cells. According to the lifetime boundaries set from the data in Fig. 5-14, events with lifetimes 300-450 µs should be identified as Eu-CDHH stained C3 cells, and those with lifetimes above 450 µs are Eu-BHHCT stained DU-145 cells. However, the observed event intensities are not strictly consistent with the data in Fig. 5-14. For the mixed cell samples as in Fig. 5-15 a significant number of the events with lifetimes >450 µs have low intensity, less than 0.1 a.u. Nevertheless, for the purpose of counting the two different cell populations, luminescence lifetime is taken as the primary multiplexing code, so that events with lifetimes >450 µs are identified as arising from DU-145 cells.

Accordingly, two distinct intensity-lifetime zones shown in Fig. 5-15 were used for the purpose of counting the events numbers attributed to the two different cell types present in the mixed samples. Event (cell) counts and the ratio of cell populations (DU-145:C3) are listed in the following Tab. 5-12.

Table 5-12 Counts of detected events in two defined detection zones attributed to the two different cell types and calculated proportions (DU145:C3) of the two cell types.

Group	No.	Total Counts	DU-145	C3	DU-145:C3
K1	M1	173	165	8	21:1
	M2	197	186	11	17:1
	M3	136	121	15	8:1
	Average	168	157	11	14:1
	Calibration		237±27	8±1	36:1~24:1
K2	M1	104	88	16	5.5:1
	M2	108	86	22	3.9:1
	M3	40	30	10	3:1
	Average	84	68	16	4:1
	Calibration		237±27	80±10	3.6:1~2.4:1
K3	M1	183	135	47	2.9:1
	M2	136	88	48	1.8:1
	M3	99	71	28	2.5:1
	Average	139	98	41	2:1
	Calibration		118±13	165±8	1:1.2~1:1.7
K4	M1	291	21	270	1:13
	M2	292	32	260	1:8
	M3	221	23	198	1:9
	Average	268	25	243	1:10
	Calibration		54±16	330±17	1:4.5~1:9.0
K5	M1	231	3	228	1:76
	M2	266	7	259	1:37
	M3	243	12	231	1:19
	Average	246	7	239	1:35
	Calibration		5±2	330±17	1:45~1:90

As shown in Tab. 5-12, almost all the cell counts detected by TRMFC are lower in comparison with the calibration data shown in Tab. 5-10 and Tab. 5-11.

The reduced numbers of cells counted by TRMFC arise from several of factors. Firstly, as suggested by the data of Tab. 4-6, Chapter 4.3, this can be caused by the horizontally orientation of the syringe pump, so that significant numbers of the target cells settle to the bottom of the syringe during the 20 mins' analytical run time, with only 50%-80% of the calibrated cell-counts delivered into the microfluidic channel. However, the counting efficiency for cells is higher compared than that of Eu polymer beads (~ 20%) when

measured with horizontal orientation of pump (see detailed discussions in Chapter 4.3). This difference is probably because the cells, with density quite similar to water, do not settle as quickly as the higher-density polymer microbeads. It is expected that orienting the syringe pump in the vertical axis will substantially alleviate this problem, increasing cell count and improving repeatability for test samples.

Note also that loss of detectable cells due to the adhesion to the surface of syringe, tubing or channels, remains a challenge for cell counting in flow cytometry in general.

A more generic reason for the low cell counts in TRMFC is the formation of cell aggregations and exclusion of these from the cell count. As shown in Fig. 5-16, when a cell aggregate transits the detection aperture, the signal appears as trains with long durations which are not resolvable, and then taken as noise and discarded in the analysis on the Labview software (which counts only single-cell and dual-cell events). This is the main cause of low count numbers in the analysis of the K2-M3 sample, where about 60% of the whole signal train was composed of long cell clusters. In this context note that the efficiencies for counting of DU-145 cells for the K1 and K2 samples, where the DU-145 concentrations are comparatively high, are much lower than those of DU-145 cells for K4 and K5 samples, where the DU-145 concentrations are very low. This is equally true for counting efficiencies of C3 cells for the K4 and K5 samples (high C3 concentrations), which are much lower than of C3 cells for the K1 and K2 samples (low C3 concentrations). This is generally consistent with the observation that cell aggregation is more severe for higher cell concentrations.[163,164]
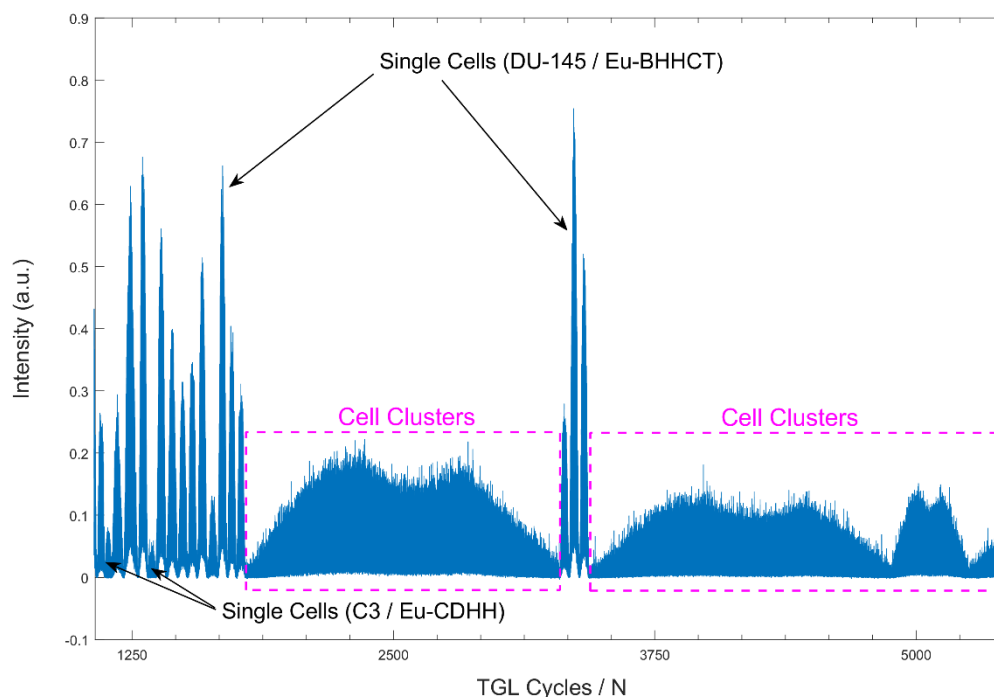
Figure 5-16 A fragment of signal train collected during analysis of the K2-M3 samples. The cell clusters caused long-lasting signal trains (marked in dash-line rectangles) that are unable to be resolved exactly, discarded by the analysis software. And the peaks with narrow width are identified as single cells signal (see the signal processing in Chapter 3), ones with higher intensities are identified to be Eu-BHHCT stained single DU-145, and ones with maximum intenstiy lower than 0.1 a.u. (consistent to Fig. 5-15) are to be Eu-CDHH stained single C3 cell.

Despite the limitations discussed above, the results of TRMFC for measured relative cell concentrations in the various cell mixes shown in the right-hand column of Tab. 5-12 are broadly consistent within the uncertainties of measurement with the calibrated relative concentrations based on cell counts made by the commercial flow cytometer (denoted as "Calibration" in Tab. 5-12). Results of this pilot demonstration have confirmed that lifetime-based multiplexed detection in microfluidic flow with Eu-chelate stained cell lines can achieve high sensitivity, for example, detection limits as low as 3 targets out from 231 counts (K5-M1), and high accuracy of lifetime measurements.

It is clear that further improvements can be made to operation of the TRMFC so as to enhance the quality of the measurements. At the flow rates 0.01 ml/min set in these pilot experiments, only 0.2 ml of sample is analysed, which at the lowest concentrations of target

cells (about 10^3 cells/ml) results in very low potential cell counts, with correspondingly poor counting statistics and greater potential for experimental error in dilution. Increased sample flow rate resulting in reduced analytical run times and/or larger sample throughput is one area where major improvements to performance of TRMFC can be made, along with design improvements such as optimised sample preparation and delivery to the microfluidic flow channel, including syringe-pump configuration.

5.6 Summary

Time-resolved microfluidic flow cytometry is capable of resolving luminescence lifetimes in microsecond to millisecond time scale and has the potential to achieve lifetime-based multiplexed detection of multiple analytes in liquid samples using a low-cost microfluidic flow platform. This chapter has reported results for a pilot multiplexing bioassay of samples containing two cell lines stained with different long-lifetime luminescent Eu-chelate. The factors that could influence the luminescence output (particularly luminescence intensity and lifetime) of the Eu-chelate stained cells have been examined in detail, and an optimised staining protocol developed. Output-stabilized DU-145 cells stained by Eu-BHHCT and C3 cells stained by Eu-CDHH were selected to provide a simple multiplexing panel. Distinct empirical zones based on lifetime and intensity ranges have been established which enable the detected events to be identified as arising from one or the other cell type, thus demonstrating lifetime-based multiplexed analysis of a biosample by TRMFC for the first time. The assay for lifetime multiplexing detection could also be developed with microspheres doped with different Eu chelates showing distinct lifetimes.

Chapter 6 summarises the key research outcomes from this research, and discusses the future prospects of developing time-resolved microfluidic flow cytometry to explore the mechanisms and applications of the long-lifetime luminescence material to biomedical diagnostics. Examples are sensing of changes of intracellular or intercellular microenvironment (pH, oxygen or ions *et al.*) by detecting luminescence output variations (i.e. lifetime) of the penetrated lanthanide chelates; and cancer cell detection in complex fluidic biosamples (i.e. urine samples and blood samples) based on lifetime-coded antibodies.

Chapter 6:   Conclusions and Perspectives

6.1 Summary

This thesis has reported design, construction and operation of a time-resolved microfluidic flow cytometer (TRMFC), aimed at achieving lifetime-based multiplexed biosensing in conjunction with long-lived luminescent probes, using a practical, low-cost technology. A microfluidic chip integrated with acoustic PZT is central to the instrumental design, which enables stable operation at the low sample flow velocities necessary for accurate long lifetime detection. Two-dimensional (2D) focusing of the sample into the centre of the microfluidic flow channel is afforded by acoustic standing wave forces at the detection zone, ensuring high event counting efficiencies approaching 100%. Time-gated luminescence (TGL) detection combined with lifetime-based multiplexing is highly effective in removing the autofluorescence interference arising from the non-target cellular background of biosamples, providing high detection sensitivity and contrast so that multiplexing of lifetime-coded in detection channels can be achieved with very low channel cross-talk. Combination of spectral (colour) coding and lifetime coding using, for example, multiple lanthanide-based fluorophores, has the potential for significant increase in multiplexing capability for analysis of complex biosamples. Additionally, the design concept of the TRMFC based on microfluidic flow sampling and lifetime decoding, the latter implemented through software computation, enables considerable simplification of the physical technology, which can substantially reduce the overall cost of the instrumentation package, compared to conventional flow cytometry based on spectral multiplexing, wherein a number of lasers and detectors are required for the different colour channels. TRMFC has a range of potential opportunities in the screening of fluidic biosamples containing multiple subpopulations of targets, i.e., blood or urine samples of human, and environmental seawaters with microorganisms.

The instrumental design, and related components selections for TRMFC and the corresponding setting of system operating parameters for the long lifetime detection have been described in detail. The signal train collected from multiple successive applications of

the TGL cycle to the sample as it transits the excitation/detection aperture has been analysed and the process of lifetime decoding demonstrated. For the optical wide-field detection system, the probability of overlap of two or more target events present in the detection region simultaneously, has been analysed, and settings of the key parameters i.e., detection aperture size, flow velocity and sample concentration have been determined to achieve optimum system performance providing highest sample throughput with lowest event-overlap probability. A method for determining the lifetimes for two overlapping events based on the length and the peak of the signal train has been implemented; the signal for more than two overlapping events is discarded and no counts recorded, though the probability for this is low, ~1% for the chosen operating parameters. Note however, in the case of significant aggregation of target cells, there may be a substantial increase in multiple, connected target events, which can lead to a large increase is signal rejection and corresponding drop in single (or dual) cell count efficiency.

Performance of the TRMFC system has been evaluated with lifetime-calibrated Eu^{3+}-doped polymer beads to establish detection capabilities in determination of lifetime, signal intensity and counting efficiency. These measurements were cross-validated against results of analysis of the same calibrated samples using time-gated orthogonal scanning automated microscopy (OSAM). The focusing efficacy of acoustic standing waves under different flow velocities in the microfluidic flow channel, and the effect of acoustic focusing on time-resolved detection results, have also been analysed. Finally, a pilot lifetime-based multiplexing bioassay has been demonstrated, developed with Eu-chelate stained cell lines, and the factors that influence luminescence output of the chelate labelled cells, i.e. lifetimes and intensities, have been analysed experimentally. Lifetime-based multiplexed analysis of a sample containing two distinct cancer cell lines has been demonstrated.

Key technical results of the research are summarised below;

i. Both cells and polymer microbeads passing through the 0.52 (*H*) × 0.58 (*W*) mm cross-section microfluidic channel can be 2D focused under a control signal of $20V_{pp}$ sinusoidal AC at 1.272 MHz for horizontal and 1.430MHz for vertical focusing, at a 5Hz cycle rate. The maximum flow rate is limited by the degree of acoustic focusing and is set to 0.010 ml/min experimentally for the events with size of 5-10 µm. However, the flow rate 0.010 ml/min for the syringe pump oriented on the horizontal axis results in a low event counting efficiency, <20%, because the denser polymer beads and cells tend to settle to the bottom of

the syringe over the extended (~20 minutes) analytical run times. Fortunately, this can be solved relatively easily by mounting the syringe pump on the vertical axis, thus improving the counting efficiency to above 90%.

ii. Increase of the detection aperture size and sample concentration increases the probability of overlapping detection events, the size of the detection aperture being the most important factor. Increasing the flow rate does not affect the overlap probability but does increase system throughput. The maximum sample flow rate was initially set to 0.010 ml/min as discussed above. To achieve a theoretical 99% counting efficiency, excluding only those cases of three or more overlapping events at a probability of 1%, the detection aperture was set at $L = 100$ µm, adjusted by a ring-actuated iris diaphragm. The transit time T_W for a target crossing the detection aperture is 181 ms at the maximum flow velocity (0.553 µm/ms at maximum flow rate Q=0.010 ml/min), and the corresponding number of TGL cycles during the transit time is N=90. The sample concentration for maximum throughput (83 events/min) is then calculated to be ~8350 events/ml.

iii. The strategy for determining individual lifetimes where target events overlap in the detection aperture is first to distinguish the double-event signals from all the signals observed and then to apply a lifetime decoding algorithm to calculate the two lifetimes. A double-event signal can be clearly identified from the length (TGL cycles number N) of the signal train and dual peaks in the profile, which has a longer pulse trains, typically $N{\geq}150$ cycles. There is a second peak located after the 100th TGL cycle, with the first peak located in the same range as those for single-event pulse trains. For the observed double-event signal, TGL cycles in advance of the first peak and those following the second peak are taken as separate events, and their lifetimes are calculated respectively and added to the accumulated event count.

iv. Performance of the TRMFC has been evaluated using 5 µm calibrated luminescent Eu-doped microbeads, and the average lifetime measured as 250 µs with coefficient of variation (CV) of 2.4%, consistent with the results for the same beads detected by OSAM. Using the time-integrated signal to describe the intensity of events, the intensity of single microbeads beads measured by TRMFC is 23 µV·s, with CV of around 40%, showing narrower distribution than comparable measurements of intensity of the same microbeads conducted using OSAM, since the acoustic focusing applied in TRMFC ensures the flowing targets lie more accurately in the focal plane of the objective, resulting in maximum uniform of

detected signal. Target event counting efficiency greater than 90% and up to 100% of the calibrated microbeads samples are achieved with the syringe pump oriented on the vertical axis which maximises loss of microbeads targets in delivery to the microfluidic flow channel.

v. The maximum flow velocity is limited by the power of the acoustic PZT to achieve tight line-focusing of 5 µm polymer microbeads in the acoustic microfluidic chip to ensure accurate determinations of lifetime and intensity. The highest focusing efficiency where the beads flow along a single axis at the very middle of the channel with CV of 5.0-6.0%, can be obtained when the flow rate is ≤0.010 ml/min. However, it has been demonstrated empirically that sufficiently accurate determination of lifetime, intensity and high counting efficiency on the TRMFC does not require perfect linear focusing, so that in practice the maximum flow rate can be doubled, to 0.02 ml/min, without significantly affecting detection performance, but increasing the detection throughput by a factor of two. Further increase of flow rate more than 0.02 ml/min will reduce the counting efficiency because the focusing of targets then deteriorates with some events travelling outside the detection aperture. On the other hand, flow rates lower than 0.010 ml/min increase analytical run-times with resultant loss of target microbeads to the walls on the syringe pump, connecting tubing and the flow channel itself. Flow rates of 0.010-0.020 ml/min are identified as optimum for detection of 5 µm Eu beads.

vi. A bioassay containing two cell lines (prostate cancer cell line DU-145 and bladder cancer cell line C3) with distinct lifetime ranges for lifetime-based multiplexing detection on TRMFC was designed by staining three Eu chelates (Eu-BHHCT, Eu-BHHBCB, Eu-CDHH) into two cell lines respectively. The factors that influence the lifetime and intensity of Eu-chelate stained cells have been explored and characterised, including different cell lines, cell growth phases, fixation of cells, chelate structures, ratio of chelators and Eu^{3+}, and reaction solvents for the chelates. Finally, stabilized prostate cancer cells (DU-145) stained with BHHCT-Eu and bladder cancer cells (C3) stained with CDHH-Eu were selected for a pilot demonstration of lifetime-multiplexed analysis of a suspension of both cell lines by TRFMC. According to the pre-calibration measurements of above two lifetime-coded cell populations, events with lifetimes 300-450 µs are recognised as Eu-CDHH stained C3 and the ones with 450-520 µs as Eu-BHHCT stained DU-145. And mixed samples containing two lifetime populations in five different spiking ratios have been analysed by TRMFC and the practical counting ratio of two populations are compared to calibration results. Broad

agreement for relative concentrations of the two different cell types between TRMFC analysis and calibration measurements by conventional flow cytometry has been demonstrated, however further improvement of TRMFC performance is required for precise analysis of complex biosamples.

6.2 Future Scope

This multidisciplinary research project implements the TGL technique on a microfluidic flow cytometry platform for long lifetime luminescence screening for the first time, enabling lifetime-multiplexed detection of luminescent targets in small samples with high sensitivity and accuracy for simple samples. Performance of this time-resolved microfluidic flow cytometer (TRMFC) suggests a number of opportunities for future improvement of the technology including engineering of the microfluidic device, optimisation of operating conditions, validation of analytical results, and ultimately application to real biomedical diagnostics.

The TRMFC performance can be further enhanced in terms of detection throughput by applying a more powerful PZT chip to decouple the limitation of flow velocity from the acoustic efficiency. Currently the maximum voltage imposed on the PZT is 20 V_{pp}, providing rather weak focusing power across the microfluidic channel, which limits the minimum size of events being focused and maximum flow velocity of beads, and consequently the detection throughput. With increase of focusing efficiency, the maximum flow rate may be improved substantially, perhaps up to 10 ml/min[40]. Although such a high flow rate is too high for long-lifetime detection in the micro- to millisecond range (requiring at least 1 ms detection time per TGL cycle and about 10 TGL cycles to achieve high sensitivity and accuracy in lifetime determination), for a detection aperture of 100 µm, the maximum flow velocity could be increased to 10 µm/ms (corresponding to flow rate 0.18 ml/min) increasing the detection throughput by factor of ~18, and increasing count rates to 1500 target events per minute.

The probability for overlapping events in TRMFC can be further analysed and verified against experimental data collected under different flow rates, samples concentrations and detection aperture sizes. Also the algorithm used to decode two overlapped events may be

extended to three of more overlapping events, to further reduce uncounted events to 0.1% or less.

There are immediate plans to apply the TRMFC methodology to screening of human urine samples for rare-event prostate cancer cell detection. This involves collaboration with colleagues in Molecular Sciences, notably Dr. Nima Sayyadi who is currently working on the prostate cancer cell immunodetection with long-lifetime Eu chelates[82]. The capability of TRMFC to avoid interference from the strong autofluorescence emission from such complex biosamples, i.e., containing protein, epithelium cells and bacterial *et al.*, is a particular advantage for this application. We are approaching this application by targeting prostate cancer cells with specific antibodies in the real clinical urine samples.

However, there are several challenges to implementing TRMFC for immuno-labelled cell detection. Firstly, the immuno-luminescence signal is significantly weaker than for the Eu-chelate stained cells used in experiments to date, because of the limited number of antigens on the cell surface and relatively low efficiencies for the primary and secondary antibody labelling processes. Weaker luminescence emission requires longer integration times, with corresponding reductions to sampling rate and potentially higher signal to noise. Secondly, rare-event cell detection in microfluidic systems requires careful handling to prevent the loss of events caused by cell aggregation or settling during the analytical run time. Optimization of the immuno-labelling protocol for prostate cancer cell detection in urine samples, together with investigation of TRMFC operational conditions and parameters for best analytical performance will therefore be required for this particular application.

The lifetime-multiplexed assay of samples containing Eu-chelate stained cancer cell lines as reported in Chapter 5, shows that the luminescence characteristics of Eu-chelates, i.e. lifetime and intensity, are strongly affected by a number of biochemical changes in the intracellular/intercellular environment.[59,119,156] This suggests another opportunity for using the sensitive lanthanide complex as biosensor in biomedical diagnostics based on the detected luminescence lifetime. A particular example might be an *in vitro* skin cancer detection model, including an epidermal cell line (HaCaT) and melanoma cancer cell line (SK-MEL-28).

References

[1].   Lu, Y. et al. On-the-fly decoding luminescence lifetimes in the microsecond region for lanthanide-encoded suspension arrays. *Nat. Commun.* **5,** 1–8 (2014).

[2].   Lu, Y. et al. Tunable lifetime multiplexing using luminescent nanocrystals. *Nat. Photonics* **8,** 32–36 (2014).

[3].   Dean, P. N. & Hoffman, R. A. Overview of Flow Cytometry Instrumentation. in *Current Protocols in Cytometry* **39,** 1.1.1-1.1.8 (John Wiley & Sons, Inc., 2007).

[4].   Darzynkiewicz, Z., Holden, E., Orfao, A., Telford, W. & Wlodkowic, D. *Recent Advances in Cytometry, Part A: Instrumentation, Methods*. *Methods In Cell Biology* **102,** (2011).

[5].   Darzynkiewicz, Z., Holden, E., Orfao, A., Telford, W. & Wlodkowic, D. *Recent Advances in Cytometry, Part B: Advances in Applications*. *Methods In Cell Biology* **103,** (2011).

[6].   Givan, A. L. *Flow Cytometry: First Principles*. (John Wiley & Sons, Inc., 2001). doi:10.1002/0471223948

[7].   Hawley, T. S. & Hawley, R. G. *Flow Cytometry Protocols*. (Humana Press, 2011). doi:10.1007/978-1-61737-950-5

[8].   Shapiro, H. M. *Practical Flow Cytometry*. (John Wiley & Sons, Inc., 2003). doi:10.1002/0471722731

[9].   Saeys, Y., Van Gassen, S. & Lambrecht, B. N. Computational flow cytometry: Helping to make sense of high-dimensional immunology data. *Nature Reviews Immunology* **16,** 449–462 (2016).

[10].   Perfetto, S. P., Chattopadhyay, P. K. & Roederer, M. Seventeen-colour flow cytometry: unravelling the immune system. *Nat. Rev. Immunol.* **4,** 648–655 (2004).

[11].   Chattopadhyay, P. et al. Toward 40+ Parameter Fluorescence Flow Cytometry. in *XXIX Congress of the International Society for Advancement of Cytometry* (2014).

[12]. Condrau, M. A., Schwendener, R. A., Niederer, P. & Anliker, M. Time-resolved flow cytometry for the measurement of lanthanide chelate fluorescence: I. Concept and theoretical evaluation. *Cytometry* **16,** 187–194 (1994).

[13]. Condrau, M. A. et al. Time-resolved flow cytometry for the measurement of lanthanide chelate fluorescence: II. Instrument design and experimental results. *Cytometry* **16,** 195–205 (1994).

[14]. Beverloo, H. B., van Schadewijk, A., van Gelderen-Boele, S. & Tanke, H. J. Inorganic phosphors as new luminescent labels for immunocytochemistry and time-resolved microscopy. *Cytometry* **11,** 784–792 (1990).

[15]. Chen, R. F., Vurek, G. G. & Alexander, N. Fluorescence decay times: Proteins, coenzymes, and other compounds in water. *Science (80-.).* **156,** 949–951 (1967).

[16]. Leif, R. C. et al. Markers for Instrumental Evaluation of Cells of the Female Reproductive Tract; Existing and New Markers. in *The Automation of Uterine Cancer Cytology* (eds. Wied, G., Babr, G. & Bartels, P.) 313–344 (Tutorials of Cytology, 1976).

[17]. Zhao, J. et al. Upconversion luminescence with tunable lifetime in NaYF 4 :Yb,Er nanocrystals: role of nanocrystal size. *Nanoscale* **5,** 944–952 (2013).

[18]. Jin, D., Connally, R. & Piper, J. Practical time-gated luminescence flow cytometry. I: Concepts. *Cytom. Part A* **71,** 783–796 (2007).

[19]. Jin, D., Connally, R. & Piper, J. Practical time-gated luminescence flow cytometry. II: Experimental evaluation using UV LED excitation. *Cytom. Part A* **71,** 797–808 (2007).

[20]. Büscher, M. Flow Cytometry Instrumentation - An Overview. *Curr. Protoc. Cytom.* **87,** e52 (2019).

[21]. Adan, A., Alizada, G., Kiraz, Y., Baran, Y. & Nalbant, A. Flow cytometry: basic principles and applications. *Crit. Rev. Biotechnol.* **37,** 163–176 (2017).

[22]. Marion G. Macey. *Flow Cytometry*. (Humana Press, 2007). doi:10.1007/978-1-59745-451-3

[23]. Derek Davies. Cell Sorting by Flow Cytometry. in *Flow Cytometry: Principles and Applications* (2007). doi:10.1007/978-1-59745-451-3

[24]. Hawley, T. S. & Hawley, R. G. *Flow Cytometry Protocols*. **1678,** (Springer New York, 2018).

[25]. Winson, M. K. & Davey, H. M. Flow Cytometric Analysis of Microorganisms. *Methods* **21,** 231–240 (2000).

[26]. Shapiro, H. M. Microbial analysis at the single-cell level: tasks and techniques. *J. Microbiol. Methods* **42,** 3–16 (2000).

[27]. Aebisher, D., Bartusik, D. & Tabarkiewicz, J. Laser flow cytometry as a tool for the advancement of clinical medicine. *Biomed. Pharmacother.* **85,** 434–443 (2017).

[28]. Jung, T., Schauer, U., Heusser, C., Neumann, C. & Rieger, C. Detection of intracellular cytokines by flow cytometry. *J. Immunol. Methods* **159,** 197–207 (1993).

[29]. Prussin, C. & Metcalfe, D. D. Detection of intracytoplasmic cytokine using flow cytometry and directly conjugated anti-cytokine antibodies. *J. Immunol. Methods* **188,** 117–28 (1995).

[30]. Gratama, J. W. et al. Flow cytometric enumeration of CD34+ hematopoietic stem and progenitor cells. European Working Group on Clinical Cell Analysis. *Cytometry* **34,** 128–42 (1998).

[31]. Huh, D., Gu, W., Kamotani, Y., Grotberg, J. B. & Takayama, S. Microfluidics for flow cytometric analysis of cells and particles. *Physiol. Meas.* **26,** R73–R98 (2005).

[32]. Shrirao, A. B. et al. Microfluidic flow cytometry: The role of microfabrication methodologies, performance and functional specification. *TECHNOLOGY* **06,** 1–23 (2018).

[33]. Chen, J. et al. Microfluidic Impedance Flow Cytometry Enabling High-Throughput Single-Cell Electrical Property Characterization. *Int. J. Mol. Sci.* **16,** 9804–9830 (2015).

[34]. Cheung, K. C. et al. Microfluidic impedance-based flow cytometry. *Cytom. Part A*

77A, 648–666 (2010).

[35]. Ateya, D. A. et al. The good, the bad, and the tiny: a review of microflow cytometry. *Anal. Bioanal. Chem.* **391,** 1485–1498 (2008).

[36]. Piyasena, M. E. & Graves, S. W. The intersection of flow cytometry with microfluidics and microfabrication. *Lab Chip* **14,** 1044–1059 (2014).

[37]. Goddard, G., Martin, J. C., Graves, S. W. & Kaduchak, G. Ultrasonic particle-concentration for sheathless focusing of particles for analysis in a flow cytometer. *Cytom. Part A* **69A,** 66–74 (2006).

[38]. Austin Suthanthiraraj, P. P. et al. One-dimensional acoustic standing waves in rectangular channels for flow cytometry. *Methods* **57,** 259–271 (2012).

[39]. Piyasena, M. E. et al. Multinode acoustic focusing for parallel flow cytometry. *Anal. Chem.* **84,** 1831–1839 (2012).

[40]. Kalb, D. M. et al. Line-Focused Optical Excitation of Parallel Acoustic Focused Sample Streams for High Volumetric and Analytical Rate Flow Cytometry. *Anal. Chem.* **89,** 9967–9975 (2017).

[41]. Gao, L. et al. Two-dimensional spatial manipulation of microparticles in continuous flows in acoustofluidic systems. *Biomicrofluidics* **9,** 1–17 (2015).

[42]. McKenna, B. K., Evans, J. G., Cheung, M. C. & Ehrlich, D. J. A parallel microfluidic flow cytometer for high-content screening. *Nat. Methods* **8,** 401–403 (2011).

[43]. Chen, Y. et al. Standing surface acoustic wave (SSAW)-based microfluidic cytometer. *Lab Chip* **14,** 916–923 (2014).

[44]. Georgakoudi, I. et al. In Vivo Flow Cytometry. *Cancer Res.* **64,** 5044–5047 (2004).

[45]. Boutrus, S. et al. Portable two-color in vivo flow cytometer for real-time detection of fluorescently-labeled circulating cells. *J. Biomed. Opt.* **12,** 020507 (2007).

[46]. Sipkins, D. A. et al. In vivo imaging of specialized bone marrow endothelial microdomains for tumour engraftment. *Nature* **435,** 969–973 (2005).

[47]. Tuchin, V. V., Tárnok, A. & Zharov, V. P. In vivo flow cytometry: A horizon of opportunities. *Cytom. Part A* **79A,** 737–745 (2011).

[48]. Tuchin, V. V. *Advanced Optical Flow Cytometry*. (Wiley-VCH Verlag GmbH & Co. KGaA, 2011). doi:10.1002/9783527634286

[49]. Zharov, V. P. et al. Photoacoustic flow cytometry: principle and application for real-time detection of circulating single nanoparticles, pathogens, and contrast dyes in vivo. *J. Biomed. Opt.* **12,** 051503 (2007).

[50]. Galanzha, E. I. & Zharov, V. P. Photoacoustic flow cytometry. *Methods* **57,** 280–296 (2012).

[51]. Juratli, M. A. et al. Real-time monitoring of circulating tumor cell release during tumor manipulation using in vivo photoacoustic and fluorescent flow cytometry. *Head Neck* **36,** 1207–1215 (2014).

[52]. Lu, Y. Advancing time-gated luminescence techniques for ultrasensitive and high-throughput biodetection. (2013).

[53]. Berezin, M. M. Y. & Achilefu, S. Fluorescence Lifetime Measurements and Biological Imaging. *Chem. Rev.* **110,** 2641–2684 (2010).

[54]. Deka, C. & Steinkamp, J. A. Time-resolved fluorescence-decay measurement and analysis on single cells by flow cytometry. *Appl. Opt.* **35,** 4481–4489 (1996).

[55]. Vereb, G., Jares-Erijman, E., Selvin, P. R. & Jovin, T. M. Temporally and Spectrally Resolved Imaging Microscopy of Lanthanide Chelates. *Biophys. J.* **74,** 2210–2222 (1998).

[56]. Jin, D. Y., Piper, J., Yuan, J. L. & Leif, R. Time-gated real-time bioimaging system using multicolor microsecond-lifetime silica nanoparticles. *SPIE Proc.* **7568,** Art. Nr. 1756819 (2010).

[57]. Jin, D. et al. Time-gated flow cytometry: an ultra-high selectivity method to recover ultra-rare-event μ-targets in high-background biosamples. *J. Biomed. Opt.* **14,** 024023 (2009).

[58]. Leif, R. C., Vallarino, L. M., Becker, M. C. & Yang, S. Increasing the luminescence of lanthanide complexes. *Cytom. Part A* **69A,** 767–778 (2006).

[59]. Song, B., Wang, G., Tan, M. & Yuan, J. A Europium(III) Complex as an Efficient Singlet Oxygen Luminescence Probe. *J. Am. Chem. Soc.* **128,** 13442–13450 (2006).

[60]. Sambrano, J. et al. Evaluating integrin activation with time-resolved flow cytometry. *J. Biomed. Opt.* **23,** 1 (2018).

[61]. Skilitsi, A. I. et al. Towards sensitive, high-throughput, biomolecular assays based on fluorescence lifetime. *Methods Appl. Fluoresc.* **5,** 034002 (2017).

[62]. Gohar, A. V. et al. Subcellular localization-dependent changes in EGFP fluorescence lifetime measured by time-resolved flow cytometry. *Biomed. Opt. Express* **4,** 1390–400 (2013).

[63]. Baggaley, E. et al. Long-lived metal complexes open up microsecond lifetime imaging microscopy under multiphoton excitation: From FLIM to PLIM and beyond. *Chem. Sci.* **5,** 879–886 (2014).

[64]. Mizukami, S., Tonai, K., Kaneko, M. & Kikuchi, K. Lanthanide-Based Protease Activity Sensors for Time-Resolved Fluorescence Measurements Structures and Schematic Representation of the Probes for Detecting Protease Activity. *J. Am. Chem. Soc* **130,** 36 (2008).

[65]. Galletly, N. P. et al. Fluorescence lifetime imaging distinguishes basal cell carcinoma from surrounding uninvolved skin. *Br. J. Dermatol.* **159,** 152–161 (2008).

[66]. Nedbal, J. et al. Time-domain microfluidic fluorescence lifetime flow cytometry for high-throughput Förster resonance energy transfer screening. *Cytom. Part A* **87,** 104–118 (2015).

[67]. Pepperkok, R., Squire, A., Geley, S. & Bastiaens, P. I. H. Simultaneous detection of multiple green fluorescent proteins in live cells by fluorescence lifetime imaging microscopy. *Curr. Biol.* **9,** 269–272 (1999).

[68]. van Geest, L. K. et al. System for fluorescence lifetime imaging microscopy. in *SPIE Proceedings* (eds. Cabib, D., Cogswell, C. J., Conchello, J.-A., Lerner, J. M. &

Wilson, T.) **3605,** 55–64 (International Society for Optics and Photonics, 1999).

[69]. Cao, R., Naivar, M. A., Wilder, M. & Houston, J. P. Expanding the potential of standard flow cytometry by extracting fluorescence lifetimes from cytometric pulse shifts. *Cytom. Part A* **85,** 999–1010 (2014).

[70]. Bastiaens, P. Fluorescence lifetime imaging microscopy: spatial resolution of biochemical processes in the cell. *Trends Cell Biol.* **9,** 48–52 (1999).

[71]. Li, W., Vacca, G., Castillo, M., Houston, K. D. & Houston, J. P. Fluorescence lifetime excitation cytometry by kinetic dithering. *Electrophoresis* **35,** 1846–1854 (2014).

[72]. Houston, J. P. et al. Overview of Fluorescence Lifetime Measurements in Flow Cytometry. in *Methods in molecular biology (Clifton, N.J.)* **1678,** 421–446 (2018).

[73]. Redford, G. I. & Clegg, R. M. Polar Plot Representation for Frequency-Domain Analysis of Fluorescence Lifetimes. *J. Fluoresc.* **15,** 805–815 (2005).

[74]. Gahlaut, N. Improving contrast in biological imaging: time-resolved microscopy and protein-targeted dendrimers. (2012).

[75]. Hanaoka, K., Kikuchi, K., Kobayashi, S. & Nagano, T. Time-resolved long-lived luminescence imaging method employing luminescent lanthanide probes with a new microscopy system. *J. Am. Chem. Soc.* **129,** 13502–13509 (2007).

[76]. Song, B., Vandevyver, C. D. B., Chauvin, A. S. & Bünzli, J. C. G. Time-resolved luminescence microscopy of bimetallic lanthanide helicates in living cells. *Org. Biomol. Chem.* **6,** 4125–4233 (2008).

[77]. Gahlaut, N. & Miller, L. W. Time-resolved microscopy for imaging lanthanide luminescence in living cells. *Cytom. Part A* **77 A,** 1113–1125 (2010).

[78]. Zhang, K. Y. et al. Long-Lived Emissive Probes for Time-Resolved Photoluminescence Bioimaging and Biosensing. *Chem. Rev.* **118,** 1770–1839 (2018).

[79]. Tu, C. C. et al. Time-Gated Imaging on Live Cancer Cells Using Silicon Quantum Dot Nanoparticles with Long-Lived Fluorescence. *ACS Photonics* **4,** 1306–1315 (2017).

[80].   Neaime, C. et al. Time-gated luminescence bioimaging with new luminescent nanocolloids based on [Mo 6 I 8 (C 2 F 5 COO) 6] 2− metal atom clusters. *Phys. Chem. Chem. Phys.* **18,** 30166–30173 (2016).

[81].   Xiao, Y. et al. Lanthanide complex-based luminescent probes for highly sensitive time-gated luminescence detection of hypochlorous acid. *Anal. Chem.* **84,** 10785–10792 (2012).

[82].   Sayyadi, N. et al. Sensitive Time-Gated Immunoluminescence Detection of Prostate Cancer Cells Using a TEGylated Europium Ligand. *Anal. Chem.* **88,** 9564–9571 (2016).

[83].   Sayyadi, N. et al. A Novel Universal Detection Agent for Time-Gated Luminescence Bioimaging. *Sci. Rep.* **6,** 27564 (2016).

[84].   Seveus, L. et al. Time-resolved fluorescence imaging of europium chelate label in immunohistochemistry and in situ hybridization. *Cytometry* **13,** 329–338 (1992).

[85].   Yuan, J., Wang, G., Kimura, H. & Matsumoto, K. Highly sensitive time-resolved fluoroimmunoassay of human immunoglobulin E by using a new europium fluorescent chelate as a label. *Anal. Biochem.* **254,** 283–7 (1997).

[86].   Zheng, X. et al. High-Contrast Visualization of Upconversion Luminescence in Mice Using Time-Gating Approach. *Anal. Chem.* **88,** 3449–3454 (2016).

[87].   Placide, V. et al. Two-photon multiplexing bio-imaging using a combination of Eu- and Tb-bioprobes. *Dalt. Trans.* **44,** 4918–4924 (2015).

[88].   Bünzli, J. C. G. Lanthanide luminescence for biomedical analyses and imaging. *Chem. Rev.* **110,** 2729–2755 (2010).

[89].   Richardson, F. S. Terbium(III) and Europium(III) Ions as Luminescent Probes and Stains for Biomolecular Systems. *Chem. Rev.* **82,** 541–552 (1982).

[90].   Nishioka, T. et al. New luminescent europium(III) chelates for DNA labeling. *Inorg. Chem.* **45,** 4088–4096 (2006).

[91].   Song, B. et al. A versatile method for quantification of DNA and PCR products based

on time-resolved EuIIIluminescence. *Analyst* **133,** 1749–1756 (2008).

[92]. Gu, L. et al. In Vivo Time-gated Fluorescence Imaging with Biodegradable Luminescent Porous Silicon Nanoparticles. *Nat. Commun.* **4,** 2326 (2013).

[93]. Lu, Y., Xi, P., Piper, J. A., Huo, Y. & Jin, D. Time-Gated Orthogonal Scanning Automated Microscopy (OSAM) for High-speed Cell Detection and Analysis. *Sci. Rep.* **2,** 837 (2012).

[94]. Jin, D. et al. Time-gated flow cytometry: an ultra-high selectivity method to recover ultra-rare-event μ-targets in high-background biosamples. *J. Biomed. Opt.* **14,** 024023 (2009).

[95]. Howell Jr, P. B. et al. Two simple and rugged designs for creating microfluidic sheath flow. *Lab Chip* **8,** 1097 (2008).

[96]. Thangawng, A. L. et al. A hard microflow cytometer using groove-generated sheath flow for multiplexed bead and cell assays. *Anal. Bioanal. Chem.* **398,** 1871–1881 (2010).

[97]. Oakey, J. et al. Particle focusing in staged inertial microfluidic devices for flow cytometry. *Anal. Chem.* **82,** 3862–3867 (2010).

[98]. Applegate, R. W. et al. Microfluidic sorting system based on optical waveguide integration and diode laser bar trapping. *Lab Chip* **6,** 422–426 (2006).

[99]. Holmes, D., Morgan, H. & Green, N. G. High throughput particle analysis: Combining dielectrophoretic particle focussing with confocal optical detection. *Biosens. Bioelectron.* **21,** 1621–1630 (2006).

[100]. Gascoyne, P. et al. Microsample preparation by dielectrophoresis: Isolation of malaria. *Lab Chip* **2,** 70–75 (2002).

[101]. Grenvall, C., Antfolk, C., Bisgaard, C. Z. & Laurell, T. Two-dimensional acoustic particle focusing enables sheathless chip Coulter counter with planar electrode configuration. *Lab Chip* **14,** 4629–37 (2014).

[102]. Piyasena, M. E. et al. Multinode Acoustic Focusing for Parallel Flow Cytometry. *Anal.*

Chem. **84,** 1831–1839 (2012).

[103]. Beyer, R. T. *Sounds of our times : two hundred years of acoustics*. (Springer-Verlag New York, 1999).

[104]. King, L. V. On the acoustic radiation pressure on spheres. *Proc. R. Soc. London. Ser. A - Math. Phys. Sci.* **147,** 212–240 (1934).

[105]. Gor'kov, L. P. On the Forces Acting on a Small Particle in an Acoustical Field in an Ideal Fluid. *Sov. Phys. Dokl.* **6,** 773 (1962).

[106]. Nyborg, W. L. Radiation Pressure on a Small Rigid Sphere. *J. Acoust. Soc. Am.* **42,** 947–952 (1967).

[107]. Laurell, T., Petersson, F. & Nilsson, A. Chip integrated strategies for acoustic separation and manipulation of cells and particles. *Chem. Soc. Rev.* **36,** 492–506 (2007).

[108]. Ter Haar, G. & Wyard, S. J. Blood cell banding in ultrasonic standing wave fields: A physical analysis. *Ultrasound Med. Biol.* **4,** 111–123 (1978).

[109]. Asudo, T. M. & Kada, T. O. Ultrasonic Radiation – Novel Principle for Microparticle Separation. *Anal. Chem.* **17,** 1341–1344 (2001).

[110]. Gautam, G. P. et al. Simple and inexpensive micromachined aluminum microfluidic devices for acoustic focusing of particles and cells. *Anal. Bioanal. Chem.* **410,** 3385–3394 (2018).

[111]. Shields, C. W., Cruz, D. F., Ohiri, K. A., Yellen, B. B. & Lopez, G. P. Fabrication and Operation of Acoustofluidic Devices Supporting Bulk Acoustic Standing Waves for Sheathless Focusing of Particles. *J. Vis. Exp.* 1–7 (2016). doi:10.3791/53861

[112]. Dual, J. & Möller, D. Acoustofluidics 4: Piezoelectricity and application in the excitation of acoustic fields for ultrasonic particle manipulation. *Lab Chip* **12,** 506 (2012).

[113]. Lenshof, A., Evander, M., Laurell, T. & Nilsson, J. Acoustofluidics 5: Building microfluidic acoustic resonators. *Lab Chip* **12,** 684 (2012).

[114]. Li, Z. et al. 2D acoustic focusing in a rectangular micro-channel of commercial flow cytometers. in *2017 IEEE International Ultrasonics Symposium (IUS)* 1–4 (IEEE, 2017). doi:10.1109/ULTSYM.2017.8092952

[115]. Shi, J. et al. Three-dimensional continuous particle focusing in a microfluidic channel via standing surface acoustic waves (SSAW). *Lab Chip* **11,** 2319 (2011).

[116]. Manneberg, O., Svennebring, J., Hertz, H. M. & Wiklund, M. Wedge transducer design for two-dimensional ultrasonic manipulation in a microfluidic chip. *J. Micromechanics Microengineering* **18,** 095025 (2008).

[117]. Wiklund, M., Spégel, P., Nilsson, S. & Hertz, H. M. Ultrasonic-trap-enhanced selectivity in capillary electrophoresis. *Ultrasonics* **41,** 329–333 (2003).

[118]. Nordin, M. & Laurell, T. Two-hundredfold volume concentration of dilute cell and particle suspensions using chip integrated multistage acoustophoresis. *Lab Chip* **12,** 4610 (2012).

[119]. Lakowicz, J. R. *Principles of Fluorescence Spectroscopy*. (Springer US, 2006). doi:10.1007/978-0-387-46312-4

[120]. Enkvist, E. et al. Protein-Induced Long Lifetime Luminescence of Nonmetal Probes. *ACS Chem. Biol.* **6,** 1052–1062 (2011).

[121]. Joo, J. et al. Gated Luminescence Imaging of Silicon Nanoparticles. *ACS Nano* **9,** 6233–6241 (2015).

[122]. Pu, C. et al. Doped Semiconductor-Nanocrystal Emitters with Optimal Photoluminescence Decay Dynamics in Microsecond to Millisecond Range: Synthesis and Applications. *ACS Cent. Sci.* **2,** 32–39 (2016).

[123]. Salinas-Castillo, A., Calahorro, A. J., Choquesillo-Lazarte, D., Seco, J. M. & Rodríguez-Diéguez, A. A new 2D cadmium chloride network with 2-aminopyrimidine displaying long lifetime photoluminescence emission. *Polyhedron* **30,** 1295–1298 (2011).

[124]. Ahern, J. C., Shilabin, A., Henline, K. M., Pike, R. D. & Patterson, H. H. Photophysical properties of {[Ag(CN) 2] − } 2 complexes trapped in a

supramolecular electron-acceptor organic framework. *Dalt. Trans.* **43,** 12044 (2014).

[125]. Guo, X.-Q., Castellano, F. N., Li & Lakowicz, J. R. Use of a Long-Lifetime Re(I) Complex in Fluorescence Polarization Immunoassays of High-Molecular-Weight Analytes. *Anal. Chem.* **70,** 632–637 (1998).

[126]. Hung, F.-F. et al. Water-Soluble Luminescent Cyclometalated Gold(III) Complexes with cis -Chelating Bis(N-Heterocyclic Carbene) Ligands: Synthesis and Photophysical Properties. *Chem. - A Eur. J.* **20,** 8604–8614 (2014).

[127]. Liu, H. et al. Balancing power density based quantum yield characterization of upconverting nanoparticles for arbitrary excitation intensities. *Nanoscale* **5,** 4770 (2013).

[128]. Boyer, J.-C. & van Veggel, F. C. J. M. Absolute quantum yield measurements of colloidal NaYF4: Er3+, Yb3+ upconverting nanoparticles. *Nanoscale* **2,** 1417 (2010).

[129]. Boyer, J.-C. & van Veggel, F. C. J. M. Absolute quantum yield measurements of colloidal NaYF4: Er3+, Yb3+ upconverting nanoparticles. *Nanoscale* **2,** 1417 (2010).

[130]. Xu, Y.-Y., Hemmilä, I., Mukkala, V.-M., Holttinen, S. & Lövgren, T. Co-fluorescence of europium and samarium in time-resolved fluorimetric immunoassays. *Analyst* **116,** 1155–1158 (1991).

[131]. Yuan, J., Wang, G., Majima, K. & Matsumoto, K. Synthesis of a Terbium Fluorescent Chelate and Its Application to Time-Resolved Fluoroimmunoassay. *Anal. Chem.* **73,** 1869–1876 (2001).

[132]. Zhang, L., Wang, Y., Ye, Z., Jin, D. & Yuan, J. New class of tetradentate β-diketonate-europium complexes that can be covalently bound to proteins for time-gated fluorometric application. *Bioconjug. Chem.* **23,** 1244–1251 (2012).

[133]. Yuan, J., Matsumoto, K. & Kimura, H. A New Tetradentate β-Diketonate-Europium Chelate That Can Be Covalently Bound to Proteins for Time-Resolved Fluoroimmunoassay. *Anal. Chem.* **70,** 596–601 (1998).

[134]. Tan, M., Wang, G., Hai, X., Ye, Z. & Yuan, J. Development of functionalized fluorescent europium nanoparticles for biolabeling and time-resolved fluorometric

applications. *J. Mater. Chem.* **14,** 2896–2901 (2004).

[135]. Hennink, E. J., de Haas, R., Verwoerd, N. P. & Tanke, H. J. Evaluation of a time-resolved fluorescence microscope using a phosphorescent Pt-porphine model system. *Cytometry* **24,** 312–320 (1996).

[136]. Lo, K. K.-W., Ng, D. C.-M. & Chung, C.-K. First Examples of Luminescent Cyclometalated Iridium(III) Complexes as Labeling Reagents for Biological Substrates. *Organometallics* **20,** 4999–5001 (2001).

[137]. Lo, K. K.-W., Lau, J. S.-Y., Lo, D. K.-K. & Lo, L. T.-L. Luminescent Cyclometalated Iridium(III) Polypyridine Complexes Containing a Thiourea Moiety: Synthesis, Characterization, Photophysics, Electrochemistry and Anion-Binding Properties. *Eur. J. Inorg. Chem.* **2006,** 4054–4062 (2006).

[138]. de Haas, R. R. et al. Phosphorescent Platinum/Palladium Coproporphyrins for Time-resolved Luminescence Microscopy. *J. Histochem. Cytochem.* **47,** 183–196 (1999).

[139]. Lo, K. K.-W., Li, C.-K., Lau, K.-W. & Zhu, N. Luminescent cyclometallated rhodium(iii) bis(pyridylbenzaldehyde) complexes with long-lived excited states. *Dalt. Trans.* **0,** 4682 (2003).

[140]. Leung, S.-K., Kwok, K. Y., Zhang, K. Y. & Lo, K. K.-W. Design of Luminescent Biotinylation Reagents Derived from Cyclometalated Iridium(III) and Rhodium(III) Bis(pyridylbenzaldehyde) Complexes. *Inorg. Chem.* **49,** 4984–4995 (2010).

[141]. Tyson, D. S., Bialecki, J. & Castellano, F. N. Ruthenium(II) complex with a notably long excited state lifetime. *Chem. Commun.* **0,** 2355–2356 (2000).

[142]. Dieke, G. H. & Crosswhite, H. M. The Spectra of the Doubly and Triply Ionized Rare Earths. *Appl. Opt.* **2,** 675 (1963).

[143]. Jin, D. et al. How to Build a Time-Gated Luminescence Microscope. in *Current Protocols in Cytometry* 2.22.1-2.22.36 (John Wiley & Sons, Inc., 2014). doi:10.1002/0471142956.cy0222s67

[144]. Meurman, O. H., Hemmilä, I. A., Lövgren, T. N. & Halonen, P. E. Time-resolved fluoroimmunoassay: a new test for rubella antibodies. *J. Clin. Microbiol.* **16,** 920–5

(1982).

[145]. Siitari, H., Hemmilä, I., Soini, E., Lövgren, T. & Koistinen, V. Detection of hepatitis B surface antigen using time-resolved fluoroimmunoassay. *Nature* **301,** 258–260 (1983).

[146]. Leif, R. C. & Vallarino, L. M. Rare-earth chelates as fluorescent markers in cell separation and analysis. *ACS Symp. Ser.* **464,** 41–58 (1991).

[147]. Selvin, P. R. & Hearst, J. E. Luminescence energy transfer using a terbium chelate: improvements on fluorescence energy transfer. *Proc. Natl. Acad. Sci.* **91,** 10024–10028 (1994).

[148]. Sayyadi, N., Connally, R. E. & Try, A. A novel biocompatible europium ligand for sensitive time-gated immunodetection. *Chem. Commun.* **52,** 1154–1157 (2016).

[149]. Campbell, R. E. et al. A monomeric red fluorescent protein. *Proc. Natl. Acad. Sci.* **99,** 7877–7882 (2002).

[150]. Chan, W. C. & Nie, S. Quantum dot bioconjugates for ultrasensitive nonisotopic detection. *Science* **281,** 2016–8 (1998).

[151]. Jin, D. Demonstration of true-color high-contrast microorganism imaging for terbium bioprobes. *Cytom. Part A* **79A,** 392–397 (2011).

[152]. Yu, J., Parker, D., Pal, R., Poole, R. A. & Cann, M. J. A europium complex that selectively stains nucleoli of cells. *J. Am. Chem. Soc.* **128,** 2294–2299 (2006).

[153]. Picot, A. et al. Long-lived two-photon excited luminescence of water-soluble europium complex: Applications in biological imaging using two-photon scanning microscopy. *J. Am. Chem. Soc.* **130,** 1532–1533 (2008).

[154]. New, E. J., Congreve, A. & Parker, D. Definition of the uptake mechanism and sub-cellular localisation profile of emissive lanthanide complexes as cellular optical probes. *Chem. Sci.* **1,** 111–118 (2010).

[155]. De Bettencourt-Dias, A. *Luminescence of Lanthanide Ions in Coordination Compounds and Nanomaterials*. (John Wiley & Sons Ltd, 2014).

doi:10.1002/9781118682760

[156]. You, Y., Lee, S., Kim, T. & Kei, O. Phosphorescent Sensor for Biological Mobile Zinc. *J Am Chem Soc.* **133,** 18328–18342 (2011).

[157]. Yuan, J. & Wang, G. Lanthanide complex-based fluorescence label for time-resolved fluorescence bioassay. *J. Fluoresc.* **15,** 559–568 (2005).

[158]. Veal, D. ., Deere, D., Ferrari, B., Piper, J. & Attfield, P. . Fluorescence staining and flow cytometry for monitoring microbial cells. *J. Immunol. Methods* **243,** 191–210 (2000).

[159]. Mackintosh, J. A. et al. A fluorescent natural product for ultra sensitive detection of proteins in one-dimensional and two-dimensional gel electrophoresis. *Proteomics* **3,** 2273–2288 (2003).

[160]. Deng, W., Jin, D., Drozdowicz-Tomsia, K., Yuan, J. & Goldys, E. M. Europium chelate (BHHCT-Eu3+) and its metal nanostructure enhanced luminescence applied to bioassays and time-gated bioimaging. *Langmuir* **26,** 10036–10043 (2010).

[161]. Hynes, J. et al. In vitro analysis of cell metabolism using a long-decay pH-sensitive lanthanide probe and extracellular acidification assay. *Anal. Biochem.* **390,** 21–28 (2009).

[162]. Mathieu, E. et al. Lanthanide-based tools for the investigation of cellular environments. *Chem. Commun.* **54,** 10021–10035 (2018).

[163]. Hubbe, M. A. Adhesion and detachment of biological cellsin vitro. *Prog. Surf. Sci.* **11,** 65–137 (1981).

[164]. Owen, E., Clifford, J. & Marson, A. The effects of surfactants on cell aggregation. *J. Cell Sci.* **32,** 363–376 (1978).

Appendix A. Brief History of Flow Cytometry

Flow cytometry has developed over the last almost 70 years from single-parameter instruments to highly sophisticated machines capable of detecting 50 parameters simultaneously. Wallace Coulter pioneered the concept in 1950s, where cell or particle volumes are deduced from an observed change in impedance (electrical conductivity) as they are flowing through a small orifice[1,2]. This is believed to be the first version of flow cytometry, with the purpose of counting cell numbers in suspension, which became the basis of the latter viable flow instruments. These Coulter counters soon became essential equipment in hospital haematology laboratories, allowing the rapid and automated counting of white and red blood cells.

In 1953, PJ Crosland-Taylor injected a suspension of red blood cells into the centre of a faster flowing stream, thus the cells were aligned in a narrow central file within the core of the wider stream preparatory to electronic counting[3]. This principle of hydrodynamic focusing was pivotal for the further development of flow cytometry.

Kamentsky *et al.* in 1965 described a two-parameter flow cytometer that measured absorption and back-scattered illumination of unstained cells, and this was used to determine cell nucleic acid content and size[4]. This instrument represented the first multiparameter flow cytometer, and the first cell sorter was described that same year by Fulwyler[5]. Use of an electrostatic deflection ink-jet[6] recording technique enabled the instrument to sort cells in volume at a rate of 1000 cells/s.

In 1969, Marvin Van Dilla and other members of the Los Alamos Laboratory group reported development of the first fluorescence-based detection cytometer that utilized the principle of hydrodynamic focusing[7]. The configuration of this instrument provided a framework that could support both the illumination and detection electronics of Kamentsky's device as well as the rapid flow and vibrating fluid jet of Fulwyler's sorter. The instrument was used for the detection of fluorescence from the Feulgen-DNA staining of Chinese hamster ovary cells and leukocytes as well as of their Coulter volume. The instrument thus led to systems for combining multiparameter of fluorescence, light scatter, and Coulter volume detection with cell sorting.

The technology that has subsequently emerged is mainly fluorescence-based detection and analysis. Cell sorting based on fluorescence[8] rapidly gained importance on the observation that fluorescently-labelled antibodies could be employed to identify specific cell types[9,10]. The popularity of flow cytometry and cell sorting was further enhanced by the development of monoclonal antibodies[11].

Over the last decades, flow cytometry and cell sorting platforms have significantly benefitted from developments in the area of optics, particularly in laser light sources, and electronics. This has reduced costs, increased flexibility, decreased space requirements, and simplified operations in flow cytometry. And flow cytometric technologies have been rapidly commercialized and widely employed in all forms of biological and biomedical research as well as within the clinical and diagnostic setting.

As multiparameter analysis of single cells has been a key tool in our understanding of complex cell systems such as the hematopoietic and immune systems, and in the understanding of cancer and immune responses[12]. It has seen continued development of polychromatic flow cytometry in multicolour / multiparameter technology and immunology. Chattopadhyay and Roederer reviewed the advances that have been achieved in polychromatic flow cytometry and cell sorting, outlined the need for multiparametric analysis and the limitations of current instrumentation and considerations of future developments [13].

Flow cytometry capable of simultaneously detecting 17 probes on individual cells at rates of ten thousands of cells per second is now routinely used[14], 30-parameter flow cytometers have recently become commercially available and 50-parameter flow cytometry is projected to be available soon[15,16]. Significant increases in the numbers of probes that can be measured by conventional fluorescence-based flow cytometers are limited by the relatively broad emission spectra of fluorescent probes, strong cellular autofluorescence[17], available light sources and detectors, and the complexity and the cost of instrument design[18].

In recent years, the need for more multiparametric technologies has given rise to new platforms of flow cytometry for the characterization of single cells. These technologies include the Fluidigm BioMark system[19], which measures 96 gene transcripts simultaneously from a single cell, and Cytometric Time of Flight (CyTOF), known as mass cytometry, for analysis of cellular protein expression with up to 100 parameters

simultaneously[20–22], and SERS (short for Surface Enhanced Raman Scattering) flow cytometry using SERS tags with narrow spectral features[23]. The emission decay rate, or equivalently lifetime, has been noticed as another parameter that can be encoded on the flow cytometry besides the fluorescence spectral characterizations[24], time-resolved flow cytometry or time-gated flow cytometry looking into probes with lifetime in nanoseconds region[24–29] or micro-milliseconds[17,30–34] are developed in order to discriminate spectrally overlap between fluorophores and improve the sensitivity of biosample analysis.

Very recently, as the data analysis method developed with arising of artificial intelligence (AI) in many areas of research and industry, researchers started to apply AI and machine learning in flow cytometry analysis to decode the high-dimensional fluorescent library efficiently and intelligently[15,35–38]. Nitta *et al.* demonstrated an artificial-intelligence-assisted, image-based flow cytometry capable of real-time rapid cell sorting based on unique chemical and morphological features[39], named Intelligent Image-Activated Cell Sorting (intelligent IACS). Suspended cells in a sample injected into the intelligent IACS are focused by the hydrodynamic focuser into a single stream, imaged by a frequency-multiplexed microscope, analysed by the real-time intelligent image processor, maintained in a single stream by the acoustic focuser during the computation, and sorted by the dual-membrane push-pull cell sorter triggered by decisions made by the image processor. The entire process is operated in a fully automated and real-time manner.

Reference:

[1].   Coulter, W. H. Means for counting particles suspended in a fluid. (1953).

[2].   Coulter, W. H. High speed automatic blood cell counter and cell size analyzer. in *Proceedings of the National Electronics Conference* **12,** 1034 (1956).

[3].   Crosland-Taylor, P. J. A Device for Counting Small Particles suspended in a Fluid through a Tube. *Nature* **171,** 37–38 (1953).

[4].   Kamentsky, L. A., Melamed, M. R. & Derman, H. Spectrophotometer: New Instrument for Ultrarapid Cell Analysis. *Science (80-.).* **150,** 630–631 (1965).

[5].   Fulwyler, M. J. Electronic Separation of Biological Cells by Volume. *Science (80-.).* **150,** 910–911 (1965).

[6].   Sweet, R. G. High Frequency Recording with Electrostatically Deflected Ink Jets. *Rev. Sci. Instrum.* **36,** 131–136 (1965).

[7].   Van Dilla, M. A., Trujillo, T. T., Mullaney, P. F. & Coulter, J. R. Cell microfluorometry: A method for rapid fluorescence measurement. *Science (80-.).* **163,** 1213–1214 (1969).

[8].   Hulett, H. R., Bonner, W. A., Barrett, J. & Herzenberg, L. A. Cell sorting: automated separation of mammalian cells as a function of intracellular fluorescence. *Science (80-.).* **166,** 747–9 (1969).

[9].   Bonner, W. A., Hulett, H. R., Sweet, R. G. & Herzenberg, L. A. Fluorescence Activated Cell Sorting. *Rev. Sci. Instrum.* **43,** 404–409 (1972).

[10].   Julius, M. H., Masuda, T. & Herzenberg, L. A. Demonstration that antigen-binding cells are precursors of antibody-producing cells after purification with a fluorescence-activated cell sorter. *Proc. Natl. Acad. Sci. U. S. A.* **69,** 1934–8 (1972).

[11].   KÖHLER, G. & MILSTEIN, C. Continuous cultures of fused cells secreting antibody of predefined specificity. *Nature* **256,** 495–497 (1975).

[12].   Barlogie, B. et al. Flow Cytometry in Clinical Cancer Research. *Cancer Res* **43,** 3982–

3997 (1983).

[13]. Chattopadhyay, P. K. & Roederer, M. Cytometry: Today's technology and tomorrow's horizons. *Methods* **57,** 251–258 (2012).

[14]. Perfetto, S. P., Chattopadhyay, P. K. & Roederer, M. Seventeen-colour flow cytometry: unravelling the immune system. *Nat. Rev. Immunol.* **4,** 648–655 (2004).

[15]. Saeys, Y., Van Gassen, S. & Lambrecht, B. N. Computational flow cytometry: Helping to make sense of high-dimensional immunology data. *Nature Reviews Immunology* **16,** 449–462 (2016).

[16]. Chattopadhyay, P. et al. Toward 40+ Parameter Fluorescence Flow Cytometry. in *XXIX Congress of the International Society for Advancement of Cytometry* (2014).

[17]. Condrau, M. A., Schwendener, R. A., Niederer, P. & Anliker, M. Time-resolved flow cytometry for the measurement of lanthanide chelate fluorescence: I. Concept and theoretical evaluation. *Cytometry* **16,** 187–194 (1994).

[18]. Chattopadhyay, P. K., Hogerkorp, C.-M. & Roederer, M. A chromatic explosion: the development and future of multiparameter flow cytometry. *Immunology* **125,** 441–449 (2008).

[19]. Citri, A., Pang, Z. P., Südhof, T. C., Wernig, M. & Malenka, R. C. Comprehensive qPCR profiling of gene expression in single neuronal cells. *Nat. Protoc.* **7,** 118–127 (2012).

[20]. Bendall, S. C. et al. Single-Cell Mass Cytometry of Differential Immune and Drug Responses Across a Human Hematopoietic Continuum. *Science (80-.).* **332,** 687–696 (2011).

[21]. Spitzer, M. H. & Nolan, G. P. Mass Cytometry: Single Cells, Many Features. *Cell* **165,** 780–791 (2016).

[22]. Newell, E. W., Sigal, N., Bendall, S. C., Nolan, G. P. & Davis, M. M. Cytometry by Time-of-Flight Shows Combinatorial Cytokine Expression and Virus-Specific Cell Niches within a Continuum of CD8 + T Cell Phenotypes. *Immunity* **36,** 142–152 (2012).

[23]. Nolan, J. P. et al. Single cell analysis using surface enhanced Raman scattering (SERS) tags. *Methods* **57,** 272–279 (2012).

[24]. Deka, C. & Steinkamp, J. A. Time-resolved fluorescence-decay measurement and analysis on single cells by flow cytometry. *Appl. Opt.* **35,** 4481–4489 (1996).

[25]. Nedbal, J. et al. Time-domain microfluidic fluorescence lifetime flow cytometry for high-throughput Förster resonance energy transfer screening. *Cytom. Part A* **87,** 104–118 (2015).

[26]. Houston, J. P., Naivar, M. A. & Freyer, J. P. Digital analysis and sorting of fluorescence lifetime by flow cytometry. *Cytom. Part A* **77,** 861–872 (2010).

[27]. Houston, J. P., Naivar, M. A., Jenkins, P. & Freyer, J. P. Capture of fluorescence decay times by flow cytometry. in *Current Protocols in Cytometry* 1–21 (John Wiley & Sons, Inc., 2012). doi:10.1002/0471142956.cy0125s59

[28]. Kage, D. et al. Luminescence lifetime encoding in time-domain flow cytometry. *Sci. Rep.* **8,** 16715 (2018).

[29]. Becker, W. et al. Time-resolved detection and identification of single analyte molecules in microcapillaries by time-correlated single-photon counting (TCSPC). *Rev. Sci. Instrum.* **70,** 1835–1841 (1999).

[30]. Manna, P. & Jimenez, R. Time and frequency-domain measurement of ground-state recovery times in red fluorescent proteins. *J. Phys. Chem. B* **119,** 4944–4954 (2015).

[31]. Condrau, M. A. et al. Time-resolved flow cytometry for the measurement of lanthanide chelate fluorescence: II. Instrument design and experimental results. *Cytometry* **16,** 195–205 (1994).

[32]. Jin, D., Connally, R. & Piper, J. Practical time-gated luminescence flow cytometry. I: Concepts. *Cytom. Part A* **71,** 783–796 (2007).

[33]. Jin, D., Connally, R. & Piper, J. Practical time-gated luminescence flow cytometry. II: Experimental evaluation using UV LED excitation. *Cytom. Part A* **71,** 797–808 (2007).

[34]. Jin, D. et al. Time-gated flow cytometry: an ultra-high selectivity method to recover ultra-rare-event μ-targets in high-background biosamples. *J. Biomed. Opt.* **14,** 024023 (2009).

[35]. Todorov, H. & Saeys, Y. Computational approaches for high-throughput single-cell data analysis. *FEBS J.* 1–17 (2018). doi:10.1111/febs.14613

[36]. Lei, C. et al. High-throughput imaging flow cytometry by optofluidic time-stretch microscopy. *Nat. Protoc.* **13,** 1603–1631 (2018).

[37]. Sassano, E. Machine Learning Methods for Flow Cytometry Analysis and Visualization. (2018).

[38]. Larrañaga, P. et al. *Machine Learning in Bioinformatics*. *Briefings in Bioinformatics* **7,** (John Wiley & Sons, Inc., 2008).

[39]. Nitta, N. et al. Intelligent Image-Activated Cell Sorting. *Cell* **175,** 1–11 (2018).

Appendix B. Instrument Operation Procedure of TRMFC

1. Securely mount the microfluidic device onto the BX51 microscope stage with the microchannel directly underneath the objective. NOTE: Ensure the PZT transducer does not make contact with the stage.

2. Load the well-mixed sample (e.g., a constant concentration of suspension of polystyrene beads or cells) into the disposable syringe and mount it securely on the pump. Connect the syringe to the microfluidic inlet with silicon tube tightly, and also a tube from outlet leading to a disposable vial for sample recollection. NOTE: Make sure no bubbles in the syringe before mounting it on the pump.

3. Connect the wires from the PZT transducer to the output from the waveform function generator. Program the settings on the function generator (e.g., peak-to-peak voltage, resonance frequencies for 2D focusing and jumping frequency between them) and monitor the output signal of the wave generator using an oscilloscope.

4. Turn on the syringe pump and program the settings on the panel (e.g., syringe inner diameter, volume, infuse or withdraw selection and working rate) and start infusing to introduce the sample into the microchannel. Turn on the function generator to begin actuating the PZT transducer. NOTE: This configuration is intended for "infuse mode" on the pump.

5. Turn on the microscope and ensure the microfluidic channel is clearly in focus. Monitor the particles or cells flowing through the device with the microscope on bright field mode to make sure they can be effectively focused into stream centre under the resonance frequencies set on the function generator.

6. Ensure all the electrical configurations are connected well in right order and turn them on. Adjust the PMT gain by tuning the potentiometer on the gain control box and monitor the control voltage on the multimeter, making sure it works at 0.9 V and set the amplifier gain on 10^5 V/A.

7. Make sure all the filters and lens mounting correctly and the luminescence signal will be split to PMT. Note: The emission should always go to PMT when the online program is running for lifetime resolving and data collection purpose, and the CCD camera only work for the video or image recording.

8. Program the LED settings on the controller panel (e.g., working mode, LED current, current limit). Turn off the bright field illustration on microscopy and turn the LED on.

9. Open the online Labview program in PC and set parameter on the software front panel (e.g., TGL period, LED pulses, PMT gating, background removal threshold and files saving path). Turn off the room light and run the real-time resolving software.

Appendix C. Research Ethics Clearance

Macquarie University
Certificate of Completion

This is to certify that:

Yan Wang

Has completed the Macquarie University online Biosafety Workshop in 2018

Assoc. Professor Subra Vemulpad – Chair
Institutional Biosafety Committee

*Certificates are valid for 3 years

MACQUARIE
University

e-learning
Certificate of completion
Awarded to:

Yan Wang

Hazardous Chemicals

Date: 03/11/2017

SECTION A	Biohazard Risk Assessment Form – NON GMO

Notification Number: NIP041214BHA

Department	Chemistry and Biomolecular Sciences	Date:	04 Dec 2014
Chief investigator:	Professor Nicolle Packer		
Contact number/email:	9850 8176 / nicki.packer@mq.edu.au		
Title of research/practical	A study of glycosylation and its changes in healthy and diseased cells and in bacteria and fungi		
Is additional approval required?	Animal Ethics ☒ Human Ethics ☒ Fieldwork Manager ☐ Other ☐ (state)_____		

Exact location(s) of research:

E8A 109 PC2/QC2 laboratory, E8C 320 laboratory, E8C 323 APAF PC2 cell culture laboratory, E8C 326 BMD laboratory, ASAM Level 1 PC2 laboratory, E8C 252 PC2 laboratory (due to complete in February 2015)

Control measures: Eliminate risk ☐ Substitute the hazard ☐ Isolate the hazard ☒ Implement engineering controls ☒ Administration ☒ (e.g. Training) **PPE ☒**
E.g. Eliminate by irradiation prior to use, isolation by class II biological safety cabinets, administration by following SWP as below, PPE as listed below.

Isolation by class II biological safety cabinets
Training by experienced personnel, laboratory induction and safe laboratory practice training conducted by experienced and authorised personnel
Following good safe operating procedures, good microbiology practices and current biological waste disposal practices
Wearing appropriate PPE in accordance to safe operating procedures

Supporting documents which must be read in conjunction with this assessment. (e.g. Safe Working Procedures, Safety Data Sheets, Guidelines/Protocols)

Safe working procedures:
1) Working with potential human pathogens and known human pathogens in PC2 laboratory
2) Working with peripheral blood in PC2 laboratory
Safe work procedure risk assessment:
1) Working with peripheral blood in PC2 laboratory

What is the type of the biological material?

Bacteria ☒ Fungi ☒ Virus ☐ Cell Line ☐ Tissue ☒ Parasite ☐ Animal ☐ Plant ☐ Soil ☐ Toxin ☐ Prions ☐ Nucleic Acid ☐ other ☒ Peripheral blood cells

What is the name of the biological agent?

ATCC cell lines
Tissue samples from melanoma patients, liver disease patients and tumour samples from patients
Peripheral blood cells and serum/plasma
Urine and faecal samples

Bacteria and Fungi

List the Personal Protective Equipment required:

Gloves ☒ Latex or Nitrile **Eye protection** ☒ Safety glasses **Clothing** ☒ Button up lab coat. PC2 surgical gowns

Footwear ☒ Enclosed covered shoes **Respiratory Protection** ☒ Face shield. N95 surgical mask (e.g.PF2 face mask) **Other** ☐ _____

What are the risks associated with this Biological Agent. (Can be more than one risk group depending on method)

Risk Group	Details of Biohazards including risks associate with biological agent http://www.absa.org/riskgroups/index.html	Biosafety level	Risk Reduction Measures (must be followed by the researcher)
Group 1- Low Individual and community risk (Microorganism that is unlikely to cause human, plant or animal disease)	Well characterised human cell lines from ATCC collection, eg. [HCT116(colon cancer), ATCC CCL-247] [A549 (Lung cancer cells), ATCC CCL-185] [HL60 (Leukemia cells), ATCC CCL-240] [OCI-AML/OCI-AML2 (Leukemia cells), from Ontario Cancer Institute, Toronto, Canada] [Jurkat(Leukemia cell), ATCC TIB-152] [K562(Leukemia cells), ATCC-243] [OPM-2(Myeloma cells)] [KARPAS(Lymphoma cells)] [MAVER(Lymphoma cells)]	**Biosafety Level 1**	1 Standard laboratory procedures will be followed in accordance with Laboratory Microbiological Standards AS/NZ 2243:3:2010 and university guidelines (see supporting documents - Section A above) and include spillage and emergency response. 2 Investigator has attended university Biosafety training course (see 3) 3 Chief Investigator identified in Section A confirms that the researchers have received appropriate training and instruction or has adequate supervision and understands safe laboratory practice according to AS/NZ2243:3:2010 and university guidelines (see supporting documents - Section A above)
Group 2- Moderate individual risk, limited community risk (Microorganism that is unlikely to be a significant risk to laboratory workers, the community/livestock/environment. Laboratory exposures may cause infection but effective treatment and preventative measures are available and the risk of spread is limited).	Human tissue samples (tested negative for HIV, Hepatitis A and B) derived from healthy patients or tumour samples from cancer patients Peripheral blood cells and serum/plasma Urine and faecal samples Bacteria, yeast, filamentous fungi	**Biosafety Level 2**	1 Standard laboratory procedures will be followed in accordance with Laboratory Microbiological Standards AS/NZ 2243:3:2010 and university guidelines which are appropriate for **Risk Group 2** (see supporting documents - Section A above) and include spillage and emergency response. 2 Researcher has attended university Biosafety training course (see 3) 3 Chief Investigator identified in Section A confirms that the researcher has received appropriate training and instruction or has adequate supervision and understands safe laboratory practice according to AS/NZ 2243:3:2010 and university guidelines (see supporting documents - Section A above)
Group 3 -High individual risk,	NA		1 Standard laboratory procedures will be followed in accordance with

Hardcopies of this document are considered uncontrolled.
Please refer to the Health & Safety internet site for latest version.

Page 2 of 6

limited community risk (Microorganisms that usually causes serious human or animal disease and may present a significant risk to laboratory workers. It could present a limited to moderate risk if spread in the community or the environment, but there are usually effective preventative measures or treatment available).	Laboratory Microbiological Standards AS/NZ 2243:3:2010 and university guidelines which are appropriate for **Risk Group 3** (see supporting documents - Section A above) and include spillage and emergency response. 2 Researcher has attended university Biosafety training course (see 3) 3 Chief Investigator identified in Section A confirms that the investigator has received appropriate training and instruction or has adequate supervision and understands safe laboratory practice according to AS/NZ 243:3:2010 and university guidelines (see supporting documents - Section A above)

Process and equipment to be used	You must include: - Brief description of work, control measures (including aerosols), sample storage, transport of samples, clean up procedures, disinfectant and waste disposal.

Cell lines
Commercial cell lines obtained from ATCC are well characterised and safe to use. Primary cell cultures derived from tissue need more caution. The cell lines are maintained and propagated in the designated PC2 laboratory listed above in CO2 incubators. Work on these cell lines requires aseptic techniques and may generate aerosols. Exposure to this may pose a risk. Hence, proper personal protection equipment (PPE) listed above are required when handling these cell lines. All work conducted on these cell lines will be done in a Class II biological safety cabinet (BSC) located in the designated PC2 laboratory listed above.

Seeded cells are collected in sealed falcon tubes for whole cell lysate extraction, membrane protein extractions, secreted protein and intracellular protein extractions. After washes using centrifugation, the cells or proteins obtained are resuspended in detergent lysis buffers and placed on ice and transferred to laboratories (E8C 324, 326,320, ASAM Level 1 PC2 laboratories) for further downstream processing. To avoid possible aerosols generated during the centrifugation steps, centrifuge will be left for 10 minutes before opening. Transport will be done in a sealed container sprayed externally with 70%(w/w) ethanol for decontamination. Any spills will be cleaned up using 1% Virkon, followed by water and 70%(w/w) ethanol. Lysis of cells will be performed mechanically using a handheld homogenizer or a needle and syringe in designated PC2 laboratories in Class II BSC.

After the procedures, all work areas will be wiped routinely using 70%(w/w) ethanol. All waste media and unwanted cell cultures will be treated with 1% Virkon and left to stand at least 15 min for decontamination before discarding as biohazard waste in doubled bagged autoclaved bags. Contaminated cell culture pipettes, pipette tips and any contaminated plastic wares will be discarded as biohazard waste in doubled bagged autoclaved bags. These bags will be transported by designated APAF personnel to E8C 202 autoclave room in a sealed unbreakable waste bin for autoclaving according to safe operating procedures outlined by the department. After autoclave, the waste is then transported in a sealed unbreakable waste bin to the locked yellow biohazard bin located at the E5A compound.

Tissue samples
Human tissue samples (tested negative for HIV, Hepatitis A and B) derived patients will be collected by collaborators and sent to us frozen on dry ice for analysis. Cell membrane extraction will be processed in the designated PC2 laboratories listed above. Tissue samples will be homogenised by handheld homogeniser or grinded in liquid nitrogen using a disposable pestle in Eppendorf tubes and this will be done in designated PC2 laboratories listed above inside a Class II BSC. After homogenisation, lysis buffer containing detergent will be added and samples will be deemed safe for transport in sealed, labelled containers to E8C 324, 320, ASAM

Level 1 PC2 laboratories for further processing and analysis. Work areas will be routinely wiped with 70%(w/w) ethanol and sterilised with UV light for at least 30 minutes.

Membrane extraction will continue on the laboratory bench in E8C 324, 320 and in ASAM Level 1 PC2 laboratories following general aseptic techniques. The protocol will involve multiple centrifugation and detergent addition steps. Any spills that occurred during sample preparation will involve the use of 1% Virkon followed by water and 70%(w/w) ethanol for disinfection and decontamination. Any waste material, includes pipette tips, waste solutions, plastic ware tubes will be disposed waste in yellow biohazard bags and will be offered to licensed disposal companies for incineration. After the procedure, laboratory benches will be sterilised and cleaned with 70%(w/w) ethanol.

Peripheral blood cells and serum/plasma

Peripheral blood will be collected in EDTA tubes and transported in sealed, labelled containers to designated PC2 laboratories listed above for processing. As aerosols may be generated during the procedure especially during centrifugation, all work will be done in a Class II BSC located in the designated PC2 laboratories listed above. To avoid possible aerosols during the centrifugation steps, centrifuge will be left for 10 minutes before opening. Any spills that occurred during sample preparation will involve the use of 1% Virkon followed by water and 70%(w/w) ethanol for disinfection and decontamination. All personnel handling blood will be trained by experienced individuals to follow standard operating procedures. PPE listed above will be used throughout the whole procedure and work areas will be decontaminated with 1% Virkon followed by water and 70%(w/w) ethanol after the procedure. Any waste generated from the procedure will be discarded as biohazard waste in yellow biohazard bags and will be offered to licensed disposal companies for incineration.

Any work on blood cells, serum or plasma isolated from peripheral blood from the above isolation procedure will be confined to designated PC2 laboratories listed above unless rendered non-hazardous via fixation or inactivation using detergents. Isolated blood cells will be co-cultured with bacteria in designated PC2 laboratories. Secreted proteins resulting from this co-culture will be obtained after washes via centrifugation performed in designated PC2 laboratories in sealed falcon tubes and placed on ice. These proteins will be transported in a sealed, labelled container, sprayed externally with 70% (w/w) ethanol to E8C 324, 320 laboratories and ASAM Level 1 PC2 laboratories for further downstream processing. Cells obtained at the end of the experiment will be tested for their viability and cell count, after which, they will be fixed with paraformaldehyde for imaging purposes. Isolated blood cells will also be subjected to immuno staining with antibodies after fixation with paraformaldehyde. All these will be performed in a Class II BSC. Upon fixation, cells are rendered non-hazardous and will be transported to E8C 324, 320 laboratories and ASAM Level 1 PC2 laboratories for immuno staining in a sealed, labelled container, sprayed externally with 70% (w/w) ethanol. Any waste generated from the procedure will be discarded as biohazard waste in yellow biohazard bags and will be offered to licensed disposal companies for incineration. Any spills will be cleaned up with 1% Virkon followed by water and 70%(w/w) ethanol for disinfection and decontamination.

Urine and faecal samples

Urine and faecal samples will be collected by collaborators and transported in sealed, labelled containers to designated PC2 laboratories for processing. Any work on urine and faecal samples will be confined to designated PC2 laboratories unless rendered non-hazardous via fixation or inactivation using detergents. They will be processed according to established standard work procedures to isolate blood cells. As aerosols may be generated during the procedure, all work will be done in a Class II BSC located in the designated PC2 laboratories. To avoid possible aerosols produced during the centrifugation steps, centrifuge will be left for 10 minutes before opening. Any spills that occurred during sample preparation will involve the use of 1% Virkon followed by water and 70%(w/w) ethanol for disinfection and decontamination. All personnel handling urine and faecal will be trained by experienced individuals to follow standard work procedures. PPE listed above will be used throughout the whole procedure and work areas will be decontaminated with 70% (w/w) ethanol after the procedure. Any waste generated from the procedure will be discarded as biohazard waste in yellow biohazard bags and will be offered to licensed disposal companies for incineration.

Bacteria and Fungi

Bacteria and fungi human pathogens will be cultured on suitable growth media to isolate the pathogens. These pathogens will be handled according to standard

Hardcopies of this document are considered uncontrolled.
Please refer to the Health & Safety internet site for latest version.

Page 4 of 6

operating procedures, using good microbiological practices at designated PC2 laboratories listed above. All work performed will be confined to a Class II BSC.

Before the start of the experiments, Class II cabinet would be wiped using 70%(w/w) ethanol for sterilisation. To prevent cross contamination, the cabinet will be sterilise with UV light for at least 30 minutes. PPE listed above will be worn in the designated PC2 laboratories at all times. If a spill occurs on the work area, 1% Virkon will be used to remove any spills from cabinet surface followed by water and then sterilized with 70%(w/w) ethanol.

Proteins secreted from bacteria and fungi will be collected after washes using centrifugation. Cells will also be collected after experiments to examine their morphology. If a spillage occurs during centrifugation of bacteria or fungi cells, the lids of the centrifuge will be left unopened for at least 10 minutes to prevent aerosol exposure. After which, the spillage will be cleaned up with 1% Virkon, followed by water and 70% (w/w) ethanol. Cells will also be collected after experiments to examine their morphology. These cells will be fixed with paraformaldehyde or methanol prior to their transport to normal laboratories (E8C 324,326, 320) to render them non-hazardous.

Once all work is completed, the cabinet will be cleaned and wipe down using 70%(w/w) ethanol for decontamination. All waste media and cultures will be decontaminate by autoclaving either in their original glassware (flasks etc) or placed in a double bagged autoclave bag (for plastic ware tubes, contaminated pipettes and tips etc) and will be transported in a sealed unbreakable bin to be autoclaved at E8C 202 autoclave room. After autoclaving, the waste is then transported in a sealed waste bin to the locked yellow bin in the E5A compound for disposal. Glassware will be decontaminated with 1% Virkon at least 15 min, washed and autoclaved before they are stored in cabinets for the next user to prevent cross contamination.

SECTION B

MACQUARIE UNIVERSITY

Biohazard Safety Committee – Risk Assessment Decision

Important Information

For **non GMO** investigations email this assessment to **biohazard@mq.edu.au** for approval by the **Biohazard** Safety Committee.

Individual Responsibilities

By submitting this assessment the Chief Investigator identified in Section A, confirms that any supporting documents, training, guidance, instruction or protocols issued by the University will been followed so far as reasonably practicable to ensure the work is carried out without risk to health, safety or the environment. The Chief investigator is responsible for ensuring, so far as reasonably practicable the safety of researchers and others who may be affected by the work described within this document.

Decision to be completed by the Biohazard Safety Committee:

The Committee has agreed that this risk assessment is sufficient for investigations to commence? **Yes × ☐ No ☐ Further action required ☐**

Further Action/Comments:
The committee has revised your risk assessment and provided the following feedback to consider.
Spills: It may be worth mentioning to use paper towels soaked in Virkon 1% and wait for ten minutes before proceed with the cleaning up.
This may be in the supporting documents.

Your risk assessment is approved to proceed.

| Name of Approver (Committee Rep): | Joanne Cuomo |
| Date Approved: | 10th of December 2014 |

This Risk Assessment must be approved for work to commence